Theoretical and Experimental Evaluation of the $^{16}\mathrm{O}(\mathrm{p},\alpha)^{13}\mathrm{N}$ Reaction Rate and Its Impact on Astrophysical Models

May Haddaj M Alruwaili

Doctor of Philosophy (PhD)

University of York

School of Physics, Engineering and Technology

July 2025

Abstract

The nuclear reactions $^{16}\mathrm{O}(\mathrm{p},\alpha)^{13}\mathrm{N}$ and $^{13}\mathrm{N}(\alpha,\mathrm{p})^{16}\mathrm{O}$ play critical roles in stellar nucleosynthesis within Type Ia (SNIa) and core-collapse supernovae (CCSN). The $^{16}\mathrm{O}(\mathrm{p},\alpha)^{13}\mathrm{N}$ reaction influences Ca/S abundance ratios in SNIa, while the inverse $^{13}\mathrm{N}(\alpha,\mathrm{p})^{16}\mathrm{O}$ reaction affects $^{13}\mathrm{C}$ production in CCSN. However, the reaction rates for both remain poorly constrained due to limited direct measurements and uncertainties in nuclear structure inputs.

This work presents a new direct measurement of the $^{16}\mathrm{O}(\mathrm{p},\alpha)^{13}\mathrm{N}$ cross-section using the MUSIC active-target detector over the centre-of-mass energy range $E_{\mathrm{cm}} = 5.7{-}7.1\,\mathrm{MeV}$, where previous datasets exhibit significant discrepancies. The resulting cross-sections were used to recalculate the stellar reaction rate under SNIa conditions, revealing a maximum enhancement of only 1.5 times the CF88 rate. The new rate was substantially lower than previous estimates of up to a factor of seven. These findings indicate that $^{16}\mathrm{O}(\mathrm{p},\alpha)^{13}\mathrm{N}$ alone cannot account for the observed Ca/S variations, suggesting a need to re-evaluate alternative reactions, such as $^{16}\mathrm{O} + {}^{12}\mathrm{C}$ fusion.

To constrain the inverse $^{13}\mathrm{N}(\alpha,\mathrm{p})^{16}\mathrm{O}$ rate relevant to CCSN, the low-energy cross section was derived from $\mathcal{R}$-matrix analysis of available $^{17}\mathrm{F}$ state information above α-threshold. By combining the $\mathcal{R}$-matrix derived cross-section at low energies with the new experimental $^{16}\mathrm{O}(\mathrm{p},\alpha)^{13}\mathrm{N}$ data at higher energies, an updated $^{13}\mathrm{N}(\alpha,\mathrm{p})^{16}\mathrm{O}$ rate was obtained. The new $^{13}\mathrm{N}(\alpha,\mathrm{p})^{16}\mathrm{O}$ rate exceeded previous estimates by up to a factor of three in the temperature range $T = 0.4{-}0.7\,\mathrm{GK}$.

Moreover, the contribution of thermally excited states was assessed. The results show that, for the temperatures of $T < 5\,\mathrm{GK}$, the cross-section measured for the ground-state transition adequately represents the stellar reaction rate.

Declaration

I, May Alruwaili, declare that this thesis is a presentation of original work and I am the sole author. This work has not previously been presented for a degree or other qualification at this University or elsewhere. All sources are acknowledged as references.

Acknowledgements

I begin by expressing my sincere gratitude to Allah (God) for everything.

I am deeply grateful to my supervisor, Prof. Alison Laird, for her continuous guidance, support, and encouragement throughout this research. Her patience, dedication, and belief in me have been invaluable, and I could not have completed this work without her. I would also like to thank Dr. Christian Diget for many helpful discussions and valuable input.

My thanks also go to Dr.Chloé Fougères, Dr.Heshani Jayatissa, and Dr.Melina Avila for their assistance during the experimental work on the MUSIC detector at Argonne National Laboratory.

I would like to acknowledge the support of the Saudi Government, the Ministry of Education, Northern Border University, and the Saudi Cultural Bureau in London for funding and supporting my studies.

I am especially grateful to my mother, whose prayers and love have been a constant source of strength and comfort throughout this journey. I also thank my brothers and sisters for their endless support in every way possible.

I am truly thankful to my friends Fajer, Amal, Alaa, and Renad for sharing this path with me from my undergraduate studies until the completion of this PhD, your friendship has been one of my greatest blessings.

A very special thank you goes to the joy of my life, my daughter Atheer, for her patience, her strength, and for always reminding me how proud she is of me. She has been my greatest source of motivation.

Finally, I would like to express a quiet and heartfelt thank you to a dear friend who guided me to this path when I had lost my way. It was never my plan to pursue a doctorate; it was this person who first suggested that we might one day become professors. Although she is no longer here, I continue this journey for both of us.

Contents

List of Figures

List of Tables

Chapter 1

Introduction

1.1 Nuclear astrophysics

Nuclear astrophysics combines nuclear physics and astrophysics to answer fundamental questions about the universe, from supernova explosions to the origin of elements [1, 2]. A central goal of this field is determining accurate reaction rates in stellar environments, as these govern elemental abundances in stars and galaxy evolution. However, nuclear reactions in stars occur at low energies near the Coulomb barrier, resulting in extremely small cross-sections. To overcome this, researchers employ high-precision experiments, often conducted in underground laboratories to reduce background noise from cosmic rays. When experimental data are not available, phenomenological and statistical models are used to estimate the cross-section [3].

1.2 The Role of $^{16}\mathrm{O}(\mathrm{p},\alpha)^{13}\mathrm{N}$ and $^{13}\mathrm{N}(\alpha,p)^{16}\mathrm{O}$ in Explosive Nucleosynthesis

The importance of the $^{16}\mathrm{O}(\mathrm{p},\alpha)^{13}\mathrm{N}$ reaction in explosive nucleosynthesis was first pointed out by Woosley et al. (1972) [4], who showed that the rate of this reaction is crucial for determining the nature of explosions that have produced the abundant elements between ^{28}Si and ^{42}Ca. Additionally, studies have shown that the $^{16}\mathrm{O}(\mathrm{p},\alpha)^{13}\mathrm{N}$ reaction plays a key role in determining the metallicity dependence of the (Ca/S) and (Ar/S) mass ratios in Type Ia supernova models. Yet, with current reaction rates, models fail to reproduce the observed (Ca/S) and (Ar/S) ratios in SNIa remnants. An observational study [5] proposed that increasing the $^{16}\mathrm{O}(\mathrm{p},\alpha)^{13}\mathrm{N}$ reaction rate by a factor of seven relative to the REACLIB [6] value significantly improves agreement with the observed (Ca/S) ratios across different progenitor metallicities. However, without direct experimental confirmation, this proposed rate increase remains unverified.

On the other hand, the reversed reaction of $^{13}\mathrm{N}(\alpha,\mathrm{p})^{16}\mathrm{O}$ has an important role in processes occurring in core-collapse supernovae (CCSN), particularly within the helium shell. Its importance stems from its competition with the $\beta+$ decay of ^{13}N to ^{13}C. This reaction contributes to the destruction of ^{13}N, thus regulating the ^{13}C affects the isotopic signature observed in presolar grains.

A revised reaction rate for $^{13}\mathrm{N}(\alpha,\mathrm{p})^{16}\mathrm{O}$ was proposed [7] based on the unbound states in the ^{17}F compound nucleus. However, missing information and unconstrained α-widths in the relevant ^{17}F states resulted in an uncertainty of a factor of 50 in the final ^{13}C production in CCSN models. In summary, the rates of $^{16}\mathrm{O}(\mathrm{p},\alpha)^{13}\mathrm{N}$ and $^{13}\mathrm{N}(\alpha,\mathrm{p})^{16}\mathrm{O}$ reactions play key roles in explosive nucleosynthesis. A new experimentally constrained rate is essential for their impact on astrophysical

models.

1.3 The Structure of ^{17}F Nuclei

The structure of ^{17}F above the α-threshold plays a crucial role in determining the reaction rate of $^{13}\mathrm{N}(\alpha,\mathrm{p})^{16}\mathrm{O}$. Since these states predominantly decay via proton emission ($\Gamma_p \gg \Gamma_\alpha$), the reaction rate is primarily governed by the small but significant α-particle widths (Γ_α).

Early studies reported tentative spin-parity assignments and unconstrained total widths. These uncertainties have complicated the reliability of ^{17}F state information for estimating the $^{13}\mathrm{N}(\alpha,\mathrm{p})^{16}\mathrm{O}$ reaction rate. Therefore, an extensive evaluation of these states was carried out in this thesis to identify the sources of uncertainty and examine the currently available information.

1.4 Aim of the Work and Thesis Structure

This study aims to provide a new, experimentally constrained reaction rate for the $^{16}\mathrm{O}(\mathrm{p},\alpha)^{13}\mathrm{N}$ reaction, which is essential for accurately modelling Type Ia supernovae (SNIa). The new rate is intended to clarify whether the $^{16}\mathrm{O}(\mathrm{p},\alpha)^{13}\mathrm{N}$ reaction alone can account for the observed variations in Ca/S and Ar/Si abundance ratios across different SNIa progenitor metallicities. Additionally, the study investigates uncertainties in the structure of the ^{17}F compound nucleus, which directly influences the nucleosynthesis of ^{13}C via the inverse $^{13}\mathrm{N}(\alpha,\mathrm{p})^{16}\mathrm{O}$ reaction during the shock-wave phase of CCSNe. This study therefore tests whether the available spectroscopic information on ^{17}F is sufficient to constrain the $^{13}\mathrm{N}(\alpha,\mathrm{p})^{16}\mathrm{O}$ rate and determine its

role in ^{13}C production.

To achieve these goals, this study combines a detailed analysis of the nuclear structure of ^{17}F with a comprehensive evaluation of available experimental data using the $\mathcal{R}$-matrix code `AZURE2` [8]. Existing spectroscopic information was compared with measurements of the $^{16}\mathrm{O}(\mathrm{p},\alpha)^{13}\mathrm{N}$ reaction to derive an improved theoretical cross-section in the low-energy region, where direct measurements are particularly challenging. At higher energies, a new experimental measurement of the $^{16}\mathrm{O}(\mathrm{p},\alpha)^{13}\mathrm{N}$ cross-section was performed. The experiment employed the MUSIC active-target multi-sampling detector to measure the reaction in inverse kinematics, where events were identified through variations in the energy loss (ΔE) of the detected particles.

Finally, the combined spectroscopic and experimental results are used to calculate updated reaction rates for both $^{16}\mathrm{O}(\mathrm{p},\alpha)^{13}\mathrm{N}$ and $^{13}\mathrm{N}(\alpha,\mathrm{p})^{16}\mathrm{O}$. These revised rates are expected to enhance the accuracy of astrophysical models for both Type Ia and core-collapse supernovae, improving our understanding of nucleosynthesis processes in explosive stellar environments. The thesis is organised as follows:

- **Chapter 2:** Theoretical background.
- **Chapter 3:** Literature review on the $^{16}\mathrm{O}(\mathrm{p},\alpha)^{13}\mathrm{N}$ reaction.
- **Chapter 4:** Nuclear structure of the ^{17}F compound nucleus.
- **Chapter 5:** New cross-section measurements of $^{16}\mathrm{O}(\mathrm{p},\alpha)^{13}\mathrm{N}$ using the MUSIC detector.
- **Chapter 6:** Results and discussion.
- **Chapter 7:** Conclusion.

Chapter 2

Background

2.1 Explosive Oxygen Burning and Intermediate-Mass Element Production in SNe Ia

Type Ia supernovae (SNe Ia) are among the most energetic events in the universe, resulting from the thermonuclear explosion of a white dwarf star. These explosions occur in binary systems where the white dwarf accretes matter from a companion star until reaching the Chandrasekhar limit ($\sim 1.4\,M_{\odot}$), triggering a thermonuclear runaway [10] (Figure 2.1). In addition to their essential role as standardised candles for measuring cosmic distances, SNe Ia are significant sites of nucleosynthesis, particularly for iron-group and intermediate-mass elements that contribute to the evolution of galactic chemistry [11], [12]. The presence of silicon in SNe Ia light curves distinguishes them from Type Ib and Ic supernovae, and observations confirm the abundance of other intermediate-mass elements, including sulphur, argon, and calcium [13, 14].

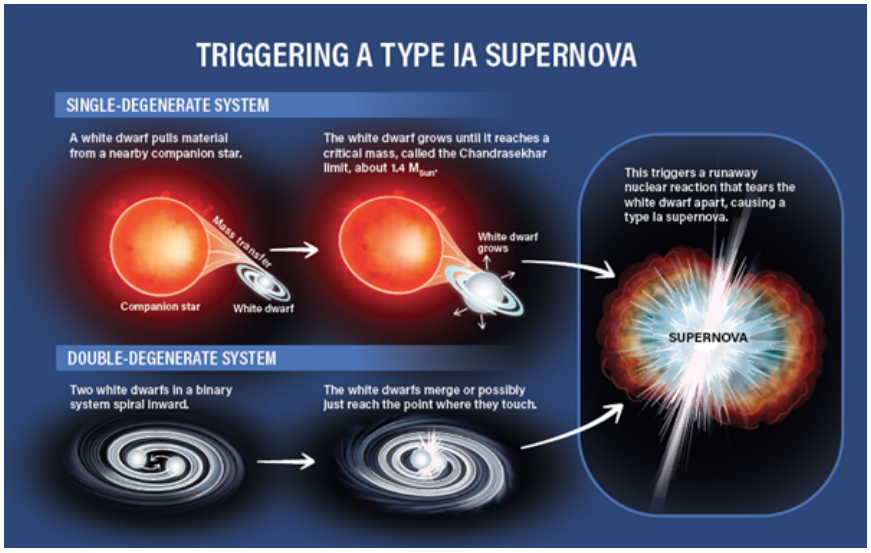

Figure 2.1: The two leading scenarios for triggering a Type Ia supernova: the single-degenerate (SD) and double-degenerate (DD) models. In the SD scenario, a white dwarf accretes material from a companion star, typically a fusion-burning star, eventually reaching the Chandrasekhar mass and exploding. In contrast, the DD scenario involves the merger of two white dwarfs, where their combined mass or the force of the collision triggers a runaway nuclear reaction, leading to the supernova explosion. Taken from Ref. [9].

Nucleosynthesis in SNe Ia proceeds in distinct layers under varying temperature and density conditions. While the central, high-temperature regions produce iron-group elements through silicon fusion, the outer, cooler layers experience oxygen and carbon burning, yielding intermediate-mass elements such as silicon, sulphur, and calcium [15] [16].

During the explosive oxygen-burning stage, at temperatures of around (3−4) GK, the destruction of ^{16}O proceeds through multiple pathways. One major channel involves the fusion of two ^{16}O nuclei to form an excited ^{32}S* nucleus [17]:

$$^{16}\mathrm{O} + ^{16}\mathrm{O} \rightarrow {}^{32}\mathrm{S}^* \rightarrow \begin{cases} ^{28}\mathrm{Si} + \alpha + 9.59\,\mathrm{MeV}, & (34\%) \\ ^{31}\mathrm{P} + p + 7.68\,\mathrm{MeV}, & (56\%) \\ ^{31}\mathrm{S} + n + 1.45\,\mathrm{MeV}, & (5\%) \\ ^{30}\mathrm{P} + d - 2.41\,\mathrm{MeV}, & (5\%) \end{cases} \tag{2.1}$$

Additionally, ^{16}O can be converted to $^{12}\mathrm{C} + \alpha$ either via photodisintegration:

$$^{16}\mathrm{O}(\gamma, \alpha)^{12}\mathrm{C}, \tag{2.2}$$

Or through a proton-capture pathway:

$$^{16}\mathrm{O}(\mathrm{p}, \alpha)^{13}\mathrm{N}(\gamma, \mathrm{p})^{12}\mathrm{C}. \tag{2.3}$$

By providing an alternative route to form ^{12}C, $^{16}\mathrm{O}(\mathrm{p}, \alpha)^{13}\mathrm{N}$ bypasses the photodisintegration channel and increases the α-particle population. The $^{16}\mathrm{O}(\mathrm{p}, \alpha)^{13}\mathrm{N}$ reaction is particularly significant under α-rich conditions during explosive oxygen burning [18], where it strongly influences the abundances of intermediate-mass elements, specifically affecting Ca/S and Si/Ar ratios. In fact, the reaction chain $^{16}\mathrm{O}(\mathrm{p}, \alpha)^{13}\mathrm{N}$ $(\gamma, \mathrm{p})^{12}\mathrm{C}$ within the α-rich branch is considered one of the most influential factors in determining the abundance of ^{40}Ca [19, 17].

The effectiveness of this reaction in α-rich environments arises from their low metallicity. At low metallicity, the abundance of free neutrons is reduced, which limits the ability to neutralise protons and leads to a higher proton fraction. Under these conditions, the $^{16}\mathrm{O}(\mathrm{p}, \alpha)^{13}\mathrm{N}$ reaction becomes even more important for converting ^{16}O to ^{12}C [5]. Consequently, the impact of the $^{16}\mathrm{O}(\mathrm{p}, \alpha)^{13}\mathrm{N}$ rate on nucleosynthesis varies with the metallicity of the progenitor.

2.2 Hydrogen Ingestion and Nucleosynthesis of ^{13}C in Core-Collapse Supernovae

CCSNe occur when massive stars ($\approx 8M_{\odot}$)reach the end of their life cycle and undergo gravitational collapse [20]. Throughout their lifetime, these massive stars experience stages of nuclear fusion, starting from hydrogen and then progressing to helium, carbon, neon, oxygen, and silicon. This process creates a layered structure similar to an onion, with an iron core at the centre. However, because elements heavier than iron cannot produce energy through nuclear fusion, the core can no longer generate the energy needed to resist gravitational forces. As the iron core grows and eventually exceeds the Chandrasekhar limit (≈1.4 $M_{\odot}$), the electron degeneracy pressure is insufficient to support it, causing the core to collapse [21].

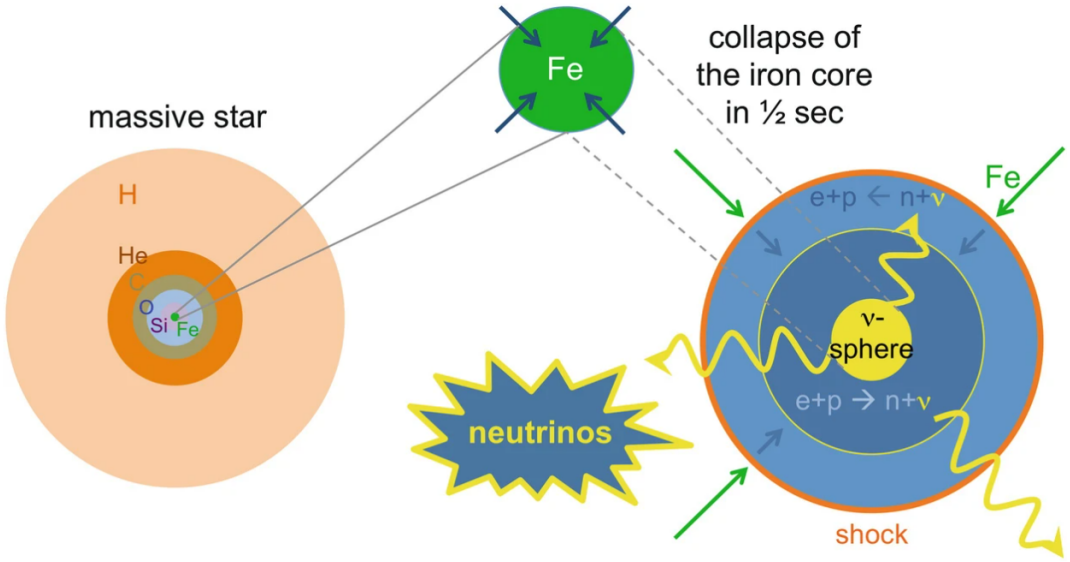

Figure 2.2: Schematic representation of the core-collapse supernova mechanism, illustrating the key stages of collapse, bounce, and explosion. The figure depicts the evolution from a massive star with an onion-shell structure to the collapse of the iron core within half a second. The process results in the formation of a shock wave, the emission of neutrinos, and the subsequent explosion. Taken from [22].

The collapsing mechanism can be seen in (Figure 2.2); as the iron core undergoes gravitational collapse, extreme pressure forces electrons and protons to merge,

forming neutrons and releasing a significant flux of neutrinos. The collapse continues until the nuclear density is reached, generating an outward shock wave [23]. During the explosion, shock-induced mixing can drive hydrogen into the helium shell [24], enabling a network of proton capture reactions that significantly influence the nucleosynthetic yields. Among these reactions, the $^{13}\mathrm{N}(\alpha,\mathrm{p})^{16}\mathrm{O}$ process is particularly important because it competes with $\beta+$ decay of $^{13}\mathrm{N}$ to $^{13}\mathrm{C}$. The process begins with proton capture on carbon:

$$^{12}\mathrm{C} + p \rightarrow {}^{13}\mathrm{N} + \gamma \tag{2.4}$$

The resulting $^{13}\mathrm{N}$ can then follow one of two competing pathways:

$$^{13}\mathrm{N} \xrightarrow{\beta^+} {}^{13}\mathrm{C} + e^+ + \nu_e \tag{2.5}$$

$$^{13}\mathrm{N}(\alpha,p)^{16}\mathrm{O} \tag{2.6}$$

The competition between these pathways significantly influences the final isotopic composition of supernova ejecta. When the $^{13}\mathrm{N}(\alpha,\mathrm{p})^{16}\mathrm{O}$ reaction is dominant, it increases the production of $^{16}\mathrm{O}$ while suppressing the formation of $^{13}\mathrm{C}$ and $^{15}\mathrm{N}$. On the other hand, a lower $^{13}\mathrm{N}(\alpha,\mathrm{p})^{16}\mathrm{O}$ reaction rate allows more $^{13}\mathrm{N}$ to decay, which results in higher abundances of $^{13}\mathrm{C}$ and $^{15}\mathrm{N}$. This balance is crucial for understanding the isotopic signatures of elevated levels of both $^{13}\mathrm{C}$ and $^{15}\mathrm{N}$ observed in presolar grains [25].

2.3 The Physics of Nuclear Reactions

Nuclear reactions involve interactions between atomic nuclei and subatomic particles, transforming elements and releasing or absorbing energy. These reactions are central to stellar nucleosynthesis, where elements are formed through fusion and other nuclear processes. Nuclear reactions can be broadly classified based on the interacting particles and the resulting products. When two nuclei or a nucleus and a subatomic particle collide, the reaction can be represented as:

$$0 + 1 \rightarrow 2 + 3 \tag{2.7}$$

Alternatively, this reaction can be expressed in shorthand notation:

$$0(1,2)3 \tag{2.8}$$

In this notation, 1 represents the target nucleus, 0 the incident particle, 2 the outgoing particle, and 3 the residual nucleus. Typically, 2 is the lighter ejected particle, and 3 is the heavier product nucleus.

2.3.1 Q-Value and Energy Considerations

Nuclear reactions involve changes in the nuclear binding energy, characterised by the Q-value. The Q-value is the net energy change in a reaction and is given by:

$$Q = (m_{01} - m_{23})\, c^2 \tag{2.9}$$

Where m_{01} and m_{01} are the total masses of the reactants and products, respectively, and c is the speed of light. Q-value determines whether a reaction releases or absorbs energy: With a positive Q-value, the reaction is exothermic, releases energy and increases the kinetic energy of the products. With a negative Q-value, the reaction is endothermic, requires energy to proceed, and sets a minimum energy threshold for the incident particle. An additional energy barrier arises from the Coulomb repulsion between positively charged nuclei in charged-particle reactions. This Coulomb barrier further increases the energy threshold, even for exothermic reactions. As a result, charged-particle reactions require higher kinetic energies to overcome this repulsion and initiate the reaction [26].

2.3.2 Nuclear Cross Sections

The probability of two colliding particles undergoing a nuclear reaction is represented by the cross-section σ and is defined as:

$$\sigma = \frac{\text{Interactions per time}}{\text{Beam particles per time per area} \times \text{Target particles}} \tag{2.10}$$

The cross-section has units of area, and its standard unit in nuclear physics is the barn (1 barn $= 1 \times 10^{-28} m^2$), with commonly used subdivisions such as millibarns, microbarns, and nanobarns. For an ideal detector that captures all reaction products, the cross-section can be calculated from the reaction yield Y using:

$$\sigma = \frac{Y}{I\, N_A\, t\, A} \tag{2.11}$$

where I is the beam intensity, N_A is Avogadro's number, t is the target thickness, and A is the molar mass of the target material. If the detector only covers a limited

solid angle $\Delta\Omega$, the differential cross-section $\frac{d\sigma}{d\Omega}$ is used:

$$\frac{d\sigma}{d\Omega} = \frac{Y}{IN_A t\Delta\Omega} \tag{2.12}$$

The differential cross section (unit of area per solid angle is square meter per steradian (m^2/sr)). This angular distribution is crucial for studying reaction mechanisms, as it reveals information about the angular momentum, spin alignments, and the quantum states involved in the reaction.

2.4 Reactions in Stellar Environments

In stellar environments, nuclear reactions occur under different conditions than laboratory experiments. Instead of having fixed energies, the reactants are in thermal equilibrium, meaning their energies follow a statistical distribution described by the Maxwell-Boltzmann distribution. Consequently, reaction rates are more meaningfully expressed as functions of temperature rather than direct cross-sections [27].

2.4.1 Thermonuclear Reaction Rates

The reaction rate (R) represents the number of nuclear reactions per unit volume per unit time and is defined as:

$$R = n_a n_b \langle \sigma v \rangle \tag{2.13}$$

Here, n_a and n_b are the number densities of the reactant species a and b, and $\langle \sigma v \rangle$ is the reaction rate coefficient, which depends on the velocity distribution of the reactants. The reaction rate coefficient averages the product of the cross-section $\sigma(v)$

and the relative velocity (v) over the Maxwell-Boltzmann velocity distribution:

$$\langle \sigma v \rangle = \int_0^\infty P(v)\sigma(v)v\, dv \tag{2.14}$$

The Maxwell-Boltzmann velocity distribution for particles of reduced mass μ at temperature T is:

$$P(v)dv = 4\pi v^2 \left(\frac{\mu}{2\pi kT}\right)^{3/2} \exp\left(-\frac{\mu v^2}{2kT}\right) dv \tag{2.15}$$

In terms of energy $E = \frac{1}{2}\mu v^2$, the distribution becomes:

$$P(E)dE = \frac{2}{\sqrt{\pi}\,(kT)^{3/2}} \sqrt{E} \exp\left(-\frac{E}{kT}\right) dE \tag{2.16}$$

2.4.2 Gamow Window and the Astrophysical S-Factor

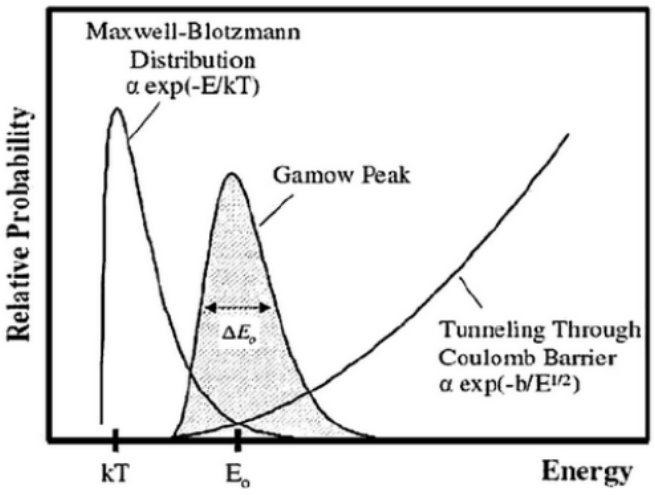

Figure 2.3: Schematic presentation of the Gamow peak region for reactions between charged particles at stellar temperatures [28]. The overlap between the Maxwell-Boltzmann distribution and the tunnelling probability defines the Gamow window

In reactions that involve charged particles, the Coulomb repulsion between positively charged nuclei becomes significant. Even at high temperatures, only a small fraction of particles possess sufficient energy to overcome this Coulomb barrier.

However, due to quantum mechanical tunnelling, reactions can still occur at lower energies. This interplay between the high-energy tail of the Maxwell-Boltzmann distribution and the tunnelling probability gives rise to the Gamow window [29].

The energy at the peak of the Gamow window(Figure 2.3),E_0 represents the most probable energy for reactions at a given temperature:

$$E_0 = 0.122(Z_1^2 Z_2^2 \mu)^{1/3} T_9^{2/3} \text{ MeV} \tag{2.17}$$

The width of the Gamow window (ΔE) is given by:

$$\Delta E = 0.2368(Z_1^2 Z_2^2 \mu)^{1/6} T_9^{5/6} \text{ MeV} \tag{2.18}$$

Where: Z_1 and Z_2 are the charges of the interacting nuclei, μ is the reduced mass and T_9 is the temperature in Gigakelvins (GK).

This Gaussian-shaped window defines the energy range where most reactions occur, making it critical to understanding reaction rates in stellar environments. To address the strong energy dependence of the cross-section resulting from the Coulomb barrier, the astrophysical S-factor ($S(E)$) has been introduced [30] [31].

$$S(E) = \sigma(E) E \exp(2\pi\eta) \tag{2.19}$$

where η is the Sommerfeld parameter, which characterises the strength of the Coulomb barrier:

$$\eta = \frac{Z_1 Z_2 e^2}{4\pi\varepsilon_0 \hbar v} \tag{2.20}$$

By removing the rapidly varying Coulomb term, the $S(E)$ provides a smoother function that captures the nuclear properties of the reaction. The reaction rate

coefficient in terms of the S-factor is:

$$\langle \sigma v \rangle = \left(\frac{8}{\pi\mu}\right)^{1/2} \left(\frac{1}{kT}\right)^{3/2} \int_0^\infty S(E) \exp\left(-\frac{E}{kT} - \sqrt{\frac{E_G}{E}}\right) dE \tag{2.21}$$

where E_G represents the Gamow energy.

2.4.3 Formalism of Nuclear Resonances

A key phenomenon in nuclear reactions is the occurrence of resonances [32]. Resonances occur when the energy of the colliding particles matches an excited energy level of the compound nucleus, resulting in a sharp increase in the reaction cross-section. These resonant states are characterised by their resonance energy (E_r), spin-parity (J^π), lifetime (τ), and the widths of the resonance (Γ). Theresonance's width (Γ) is related to its lifetime through :

$$\Gamma = \frac{\hbar}{\tau} \tag{2.22}$$

For narrow resonances typically identified when their widths are much smaller than the width of the Gamow window ($\Gamma \ll \Delta$) [29], the Breit-Wigner formula describes the cross-section [29] as follows:

$$\sigma_{\mathrm{BW}}(E) = \frac{\lambda^2}{4\pi} \frac{(2J+1)(1+\delta_{ab})}{(2j_a+1)(2j_b+1)} \frac{\Gamma_i \Gamma_f}{(E_r - E)^2 + \Gamma^2/4} \tag{2.23}$$

In this equation, λ is the de Broglie wavelength associated with the relative motion of the projectile + target system in the entrance channel. In special cases such as (p, γ) or (p, α) reactions on heavy targets, $\mu \approx m_p$, and the expression

reduces numerically to the proton de Broglie wavelength [33]. The quantities j_a and j_b denote the intrinsic spins of the interacting nuclei a and b, so that the factor $(2J+1)(1+\delta_{ab})/\Big[(2j_a+1)(2j_b+1)\Big]$ accounts for the statistical weighting of the resonance with spin J. Here, δ_{ab} is the Kronecker delta, which equals one only when the two particles are identical ($a = b$), thereby avoiding double counting of indistinguishable configurations. The quantities Γ_i and Γ_f are the partial widths of the resonant state of the compound system formed by the $a + b$ interaction, corresponding to decay through the entrance and exit channels, respectively. The total width $\Gamma = \sum_c \Gamma_c$ characterises the lifetime of this compound resonance, while the ratios Γ_i/Γ and Γ_f/Γ determine the probabilities for the resonance to decay through the corresponding channels. Here, E is the centre-of-mass energy of the interacting $a + b$ system, and E_r is the resonance energy at which the compound nucleus forms a state with spin J.

The strength of the narrow resonance ($\omega\gamma$) [31] is defined as:

$$\omega\gamma = \frac{(2J+1)(1+\delta_{ab})}{(2j_a+1)(2j_b+1)}\frac{\Gamma_i\Gamma_f}{\Gamma} \tag{2.24}$$

This value quantifies the contribution of the resonance to the overall reaction cross-section and rate, measured in keV. The reaction rate simplifies for narrow resonances is given by:

$$N_A\langle\sigma v\rangle = N_A\left(\frac{(2\pi)^{3/2}}{\mu(kT)^{3/2}}\right)\omega\gamma e^{-E_r/kT} \tag{2.25}$$

In contrast, when the resonance width Γ is comparable to the Gamow width, or $\Gamma/E_r \geq 10\%$ [31], the resonance is classified to as a broad resonance. In this case, the contribution of the resonance extends over a wide range of energies rather than

being confined sharply around E_r. As a result, the narrow resonance approximation is no longer valid, and the reaction rate must be obtained by evaluating the full Maxwellian convolution::

$$N_A\langle\sigma v\rangle = N_A\left(\frac{8}{\pi\mu}\right)^{1/2}\frac{1}{(kT)^{3/2}}\int_0^\infty \sigma(E)Ee^{-E/kT}\,\mathrm{d}E \tag{2.26}$$

The energy dependence of the cross section is then described by the Breit–Wigner expression:

$$\sigma_{\mathrm{BW}}(E) = \frac{\pi}{k^2}\frac{\omega\Gamma_a(E)\Gamma_b(E)}{(E-E_r)^2+(\Gamma(E)/2)^2} \tag{2.27}$$

where the partial widths $\Gamma_a(E)$ and $\Gamma_b(E)$, as well as the total width $\Gamma(E)$, may vary significantly with energy for broad resonances. This formalism ensures that these energy dependencies are fully taken into account when computing the reaction rate.

2.4.4 Treatment of the Gamow Window in Endothermic Reactions

The reaction $^{16}\mathrm{O}(\mathrm{p},\alpha)^{13}\mathrm{N}$ is endothermic, with a Q-value of $Q = -5.218$ MeV. For such reactions, determining the Gamow window using the standard expression (e.g., Eq. 2.17) is not meaningful, as it typically yields energies below the reaction threshold, where the cross-section is essentially zero.

An alternative approach is used instead: the Gamow window is estimated based on the forward (exothermic) reaction and then shifted by the Q-value of the reaction. For the $^{16}\mathrm{O}(\mathrm{p},\alpha)^{13}\mathrm{N}$ reaction at a temperature of $T = 3.5$ GK, the Gamow window (E_G) is determined as:

$$E_G{}^{^{16}\mathrm{O}(\mathrm{p},\alpha)^{13}\mathrm{N}} = E_G{}^{^{13}\mathrm{N}(\alpha,\mathrm{p})^{16}\mathrm{O}} + Q, \tag{2.28}$$

where the $^{13}\mathrm{N}(\alpha,\mathrm{p})^{16}\mathrm{O}$ is the forward reaction, and the Q-value is 5.218 MeV.

Using this method, the effective Gamow window for the $^{16}\mathrm{O}(\mathrm{p},\alpha)^{13}\mathrm{N}$ reaction is found to lie within the range:

$$E_{\mathrm{cm}} = 6.499 \text{ MeV} - 8.902 \text{ MeV}, \quad \Rightarrow \quad E_{\mathrm{x}} = 5.899 \text{ MeV} - 8.302 \text{ MeV}, \tag{2.29}$$

where E_{x} refers to the excitation energy of the compound nucleus $^{17}\mathrm{F}$. Therefore, the states within this excitation energy range in $^{17}\mathrm{F}$ are expected to be the most influential in determining the reaction rate.

2.4.5 Thermal Population of Excited States and Stellar Enhancement Factor

In experimental measurements of nuclear cross-sections, target nuclei are usually in their ground state. As a result, the resulting reaction rates only reflect contributions from the ground state.

In stellar environments, however, the situation differs [34, 35] . The excited states of the target nucleus become thermally populated according to the Maxwell-Boltzmann distribution. The probability of a state i being populated at temperature T is given by:

$$P^i = \frac{g^i}{G} \exp\left(-\frac{E^i}{kT}\right), \tag{2.30}$$

where $g^i = 2J^i + 1$ is the statistical weight of the state with spin J^i, E^i is the excitation energy above the ground state, and G is the partition function:

$$G = \sum_i g^i \exp\left(-\frac{E^i}{kT}\right). \tag{2.31}$$

At low temperatures, the exponential suppression on the excited states is too high, and the excited states are effectively scarcely populated, leading to $G \approx 1$, with the ground state overwhelmingly dominating, making the excited states' contribution to the rate negligible.

However, as the temperature rises beyond ~ 1 GK, this suppression is reduced significantly, and excited states begin to contribute meaningfully to the reaction rate. This results in a stellar rate that is higher than the experimental rate due to the contribution of thermally excited states. The enhancement of the experimental rate is quantified by the Stellar Enhancement Factor (SEF), defined as:

$$\text{SEF} = \frac{NA\langle\sigma v\rangle^*}{NA\langle\sigma v\rangle}, \tag{2.32}$$

Where $NA\langle\sigma v\rangle^*$ is the stellar reaction rate that includes excited-state contributions, and $NA\langle\sigma v\rangle$ is the ground-state reaction rate obtained from experiments.

The Stellar Enhancement Factor (SEF) is typically estimated using statistical models, most notably the Hauser-Feshbach (H-F) [36] formalism. These models simulate the population and decay of nuclear states under thermal conditions, allowing for the inclusion of excited-state contributions in the reaction rate.

Tabulated SEF values for a wide range of reactions can be found in works such as Rauscher and Thielemann [37] and Goriely, Hilaire, and Koning [38]. Modern nuclear reaction codes, such as TALYS [39], incorporate the Hauser-Feshbach approach to automatically account for thermally populated excited states when computing stellar reaction rates.

It was suggested that for reactions with a high negative Q-value, the Coulomb barrier can suppress contributions from thermally excited states, often leading to a

larger ground state fraction and making laboratory measurements more representative of the stellar rate with a Stellar Enhancement Factor (SEF)≈ 1 [40, 41, 42].

However, a Stellar Enhancement Factor (SEF) close to unity does not necessarily imply negligible contributions from excited states to the stellar reaction rate. This is because the excited state may influence the decay branching ratios of the compound nucleus, even if its thermal population is low as previously seen in the reaction of $^{20}\mathrm{Ne}(\gamma,\alpha)^{16}\mathrm{O}$ [43].

2.5 Forward and Reverse Reactions

Nuclear reactions are time-reversible, which means that the cross-sections of a forward reaction and its reverse are related by detailed balance [44] [45]. So for a forward reaction of $(01 \rightarrow 23)$ and the reverse reaction $(23 \rightarrow 01)$ the cross-sections can be described by :

$$\frac{\sigma_{23\rightarrow 01}}{\sigma_{01\rightarrow 23}} = \frac{(2j_0+1)(2j_1+1)}{(2j_2+1)(2j_3+1)} \cdot \frac{\mu_{01}E_{01}(1+\delta_{23})}{\mu_{23}E_{23}(1+\delta_{01})} \tag{2.33}$$

Here: E_{01} and E_{23} are the center-of-mass energies for the forward and reverse reactions, respectively. μ_{01} and μ_{23} are the reduced masses of the initial and final states, where:

$$\mu_{ij} = \frac{m_i m_j}{m_i + m_j} \tag{2.34}$$

And E_{23}= E_{01}+Q then, we can write the ratio of the reaction rate as:

$$\frac{N_A\langle\sigma v\rangle_{23\rightarrow 01}}{N_A\langle\sigma v\rangle_{01\rightarrow 23}} = \frac{(2j_0+1)(2j_1+1)(1+\delta_{23})}{(2j_2+1)(2j_3+1)(1+\delta_{01})} \left(\frac{\mu_{01}}{\mu_{23}}\right)^{3/2} e^{-Q_{01\rightarrow 23}/kT} \tag{2.35}$$

2.6 $\mathcal{R}$-Matrix Formalism and AZURE2

The Breit-Wigner approach, as shown in Eq. 2.23 and Eq. 2.27, is well-suited for describing isolated resonances. However, its applicability decreases as the number of resonances and associated reaction channels increases. In contrast, $\mathcal{R}$-matrix theory provides a more comprehensive framework for modelling multi-channel resonances and their interference effects, making it essential to study complex nuclear systems [46, 47].

A fundamental assumption in $\mathcal{R}$-matrix theory is the division of configuration space into two distinct regions: an *internal region*, where the nuclear interaction occurs, and the total wavefunction is expanded in terms of eigenstates, and an *external region*, where the interaction is primarily governed by the Coulomb potential [48]. The wavefunctions in these two regions are matched at a boundary(known as channel radius), allowing the $\mathcal{R}$-matrix to connect the parameters of the compound nucleus to the experimental observables. Mathematically, the $\mathcal{R}$-matrix is defined as:

$$R_{cc'} = \sum_{\lambda} \frac{\gamma_{\lambda c}\gamma_{\lambda c'}}{E_\lambda - E} \tag{2.36}$$

where E_λ is the resonance energy, and E is the centre-of-mass energy of the reaction. and $\gamma_{\lambda c}$ is the reduced width amplitude given by:

$$\gamma_\lambda = \left(\frac{\hbar^2}{2\mu R^2}\right)^{1/2} \theta_\lambda \tag{2.37}$$

where θ_λ is the dimensionless reduced width, μ is the reduced mass, and R is the channel radius. The observed partial width Γ_λ of a specific channel λ is connected

to the reduced width amplitude $\gamma_\lambda$by:

$$\Gamma_\lambda = 2P_l(E)\gamma_\lambda^2 \tag{2.38}$$

where $P_l(E)$ is the penetrability factor, which accounts for the probability of a particle tunnelling through the Coulomb barrier.

The penetrability factor itself is defined as:

$$P_l(E) = \frac{kR}{F_l^2(kR) + G_l^2(kR)} \tag{2.39}$$

where $k = \sqrt{2\mu E/\hbar^2}$ is the wave number, and F_l and G_l are the regular and irregular Coulomb wavefunctions, respectively [49].

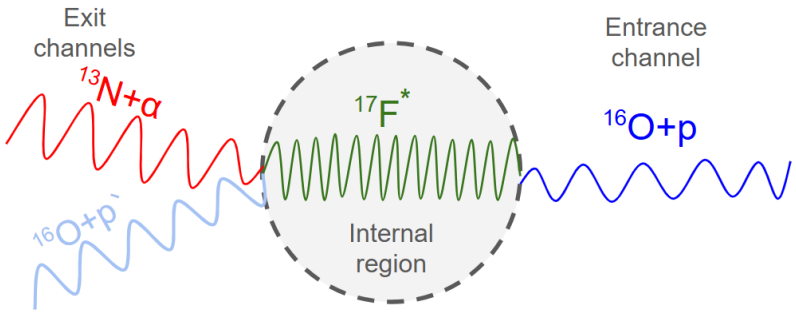

Figure 2.4: Schematic representation of the $\mathcal{R}$-matrix approach for the ^{16}O(p, α)^{13}N reaction. The entrance channel ^{16}O (shown in blue) leads to the formation of the compound nucleus ^{17}F* (internal region, green wave function). The compound nucleus can decay via different exit channels: either back to ^{16}O (elastic scattering, light blue) or to the reaction product ^{13}N + α (red). The black dashed boundary represents the channel radius, where the matching condition between the internal and external wavefunctions is applied in $\mathcal{R}$-matrix theory.

2.6.1 AZURE2 for Resonance Parameter Fitting

AZURE2 [8] is a multilevel, multi-channel $\mathcal{R}$-matrix code developed for analysing and extrapolating low-energy nuclear reactions relevant to astrophysics. It applies the $\mathcal{R}$-matrix formalism to experimental data, enabling the extraction of resonance parameters and the calculation of reaction rates [50]. Since its development, AZURE2 has been widely used to determine reaction cross-sections and rates at stellar temperatures [51, 52, 53].

In addition, AZURE2 can optimise key resonance parameters, including resonance energies (E_λ) and reduced width amplitudes ($\gamma_{\lambda c}$) through a fitting process. The fitting is achieved through an iterative process that minimises the χ^2 function, defined as:

$$\chi^2 = \sum_i \frac{(y_i^{\text{exp}} - y_i^{\text{calc}})^2}{\sigma_i^2} \tag{2.40}$$

where y_i^{exp} denotes the experimental data, y_i^{calc} is the theoretical prediction, and σ_i represents the associated uncertainty.

The integration of $\mathcal{R}$-matrix theory within AZURE2 has significantly enhanced the precision of reaction rate calculations, particularly in cases where direct experimental measurements at low energies are challenging.

2.7 Energy Loss of Charged Particles and Ionisation Chambers

2.7.1 Energy Loss of Charged Particles in Matter

When charged particles such as alpha particles, protons, or heavy ions pass through a material, they lose energy primarily through interactions with the atomic electrons of the medium. These interactions transfer energy to the electrons, either ejecting them from their orbitals (ionisation) or raising them to higher energy states (excitation). Although interactions with atomic electrons dominate energy loss, interactions with atomic nuclei can also contribute to energy loss. The most likely mechanism of nuclear interaction is Rutherford scattering [54], where the charged particle is deflected by the repulsive electrostatic field of the nucleus, resulting in nuclear recoil. Less frequently, if the projectile has sufficient energy to overcome the Coulomb barrier, it may induce a nuclear reaction, such as fusion or inelastic scattering, where energy is transferred to nuclear excitation or particle emission. However, due to the small size of the nucleus and strong Coulomb repulsion, nuclear interactions remain a minor contribution to the total energy loss, compared to ionisation by electrons.

The rate of energy loss of the charged particles per unit path length is known as the stopping power *(S)* and is expressed as:

$$-\frac{dE}{dx} = S \tag{2.41}$$

A detailed description is provided by the Bethe-Bloch formula [55], which models

the energy loss of charged particles:

$$-\frac{dE}{dx} \approx \frac{4\pi e^4}{m_e}\frac{Z_p^2}{v^2}\left(N_A\rho\frac{Z_t}{M_t}\right)\ln\left(\frac{2m_e v^2}{I}\right) \tag{2.42}$$

Z_p is the charge of the incident particle, v is its velocity, e is the elementary electron charge, m_e is the electron mass, N_A is Avogadro's number, ρ is the mass density of the target material, and Z_t and M_t are the atomic number and mass of the target material, respectively; I is the mean excitation potential of the material.

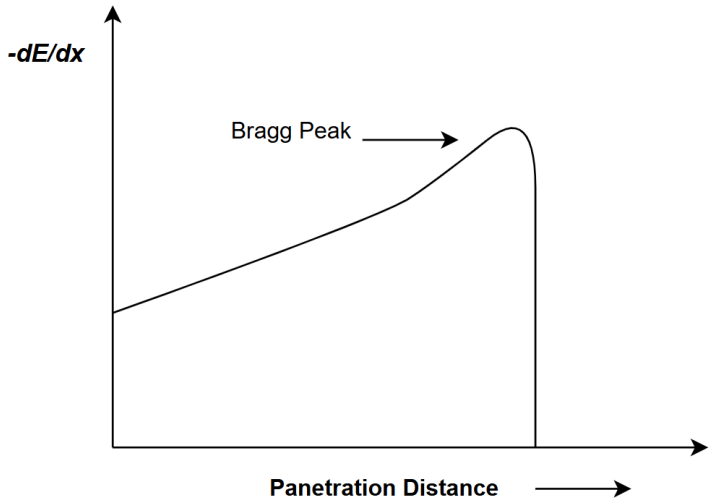

Figure 2.5: Energy loss of an alpha particle as a function of depth in a material, illustrating the Bragg peak as a rapid increase in energy deposition near the end of the particle's range.

This equation shows that energy loss is inversely proportional to the square of the particle's velocity. As a result, a faster particle loses less energy per unit distance, while a slower particle experiences greater stopping power. This leads to a rapid increase in energy deposition just before the particle comes to rest, where the particle velocity is low, creating what is known as the Bragg peak (Figure 2.5).

The total distance a charged particle travels through a medium before stopping is referred to as the range. The range of a particle depends on its type (mass and

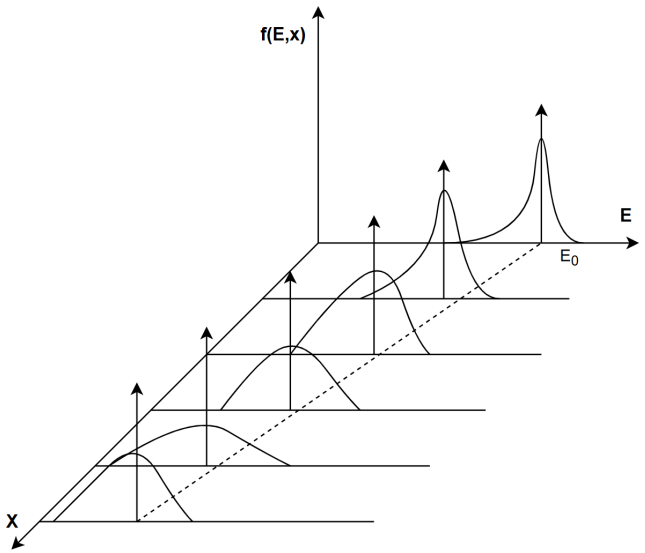

Figure 2.6: Energy distribution of monoenergetic charged particles at different depths in the medium. As the particles lose energy, the distribution broadens, illustrating the effect of energy straggling.

charge), initial energy and the density of the material. Higher-energy particles travel farther before stopping, while denser materials shorten the range due to increased interactions. Theoretical predictions of range and energy loss are often computed using SRIM (Stopping and Range of Ions in Matter) [56], a widely used simulation tool.

Although stopping power provides a mean energy loss per unit path, individual particles experience fluctuations in energy loss due to the statistical probability of the interactions. As a result, not all particles within a monoenergetic beam reach the same final energy, leading to a spread in their stopping distances. This effect, known as energy straggling, causes a broadening of the energy distribution as the beam penetrates the material. Figure 2.6 illustrates how a beam of charged particles develops a broader energy spread as it traverses matter.

2.7.2 Gas Ionisation Chambers

Ionisation chambers [57] are widely used in nuclear astrophysics experiments to study low-energy nuclear reactions. This detector provides high detection efficiency, accurate measurements of energy loss, and the ability to track charged particles as they traverse the gas. Over the years, many detectors, including MUSIC [58], TACTIC [59], ANASEN [60], and AT-TPC [61], have incorporated ionisation chamber mechanism to investigate nuclear reactions under astrophysical conditions. A typical gas ionisation chamber consists of a gas volume held between two electrodes (Figure 2.7).

When the beam passes through the gas, it ionises the gas molecules, creating positive ions and free electrons. An applied electric field forces the negative electrons to drift toward the anode and the positive ions toward the cathode. The collected charge generates a measurable electric current, which is proportional to the energy deposited by the radiation.

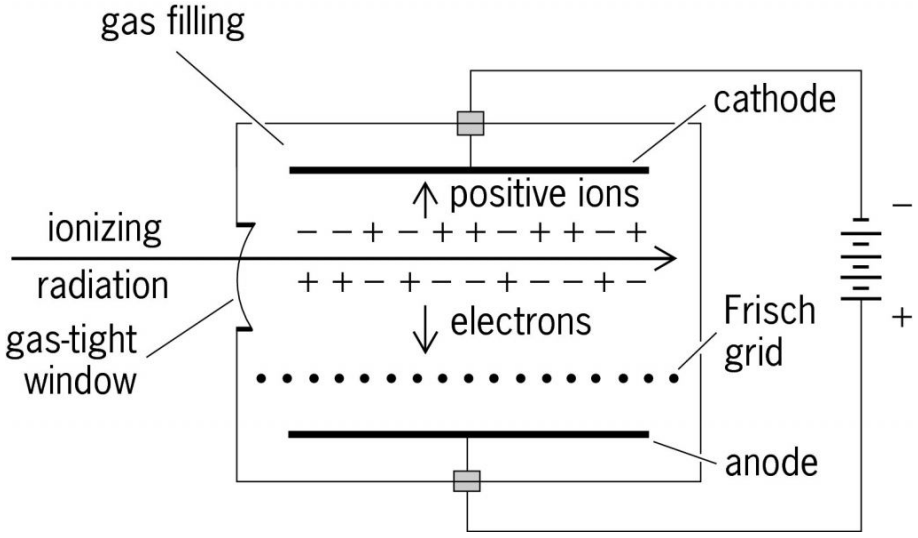

Figure 2.7: A parallel-plate ionisation chamber, illustrating the gas volume, electrodes, and electric field lines [62].

In some ionisation chambers, the active target method is used, where the gas

serves as both the detecting medium and the target for nuclear reactions. This design allows for complete detection and measurement of energy loss (ΔE), the primary beam, and the residual charged particles. Later, the recorded energy-loss patterns are used for particle identification.

Chapter 3

Literature

3.1 $^{16}\mathrm{O}(\mathrm{p},\alpha)^{13}\mathrm{N}$ Rates in Stellar Libraries

The thermonuclear reaction rate for $^{16}\mathrm{O}(\mathrm{p},\alpha)^{13}\mathrm{N}$ remains poorly constrained, particularly in the temperature range relevant for explosive oxygen burning in Type Ia supernovae (SNe Ia), due to limited experimental cross-section data and theoretical inconsistencies across rate libraries.

The first published rate was introduced by Wagoner in 1969 [63]. However, the numerical derivation of this rate was not documented, and its extrapolation method was not justified. Furthermore, Woosley et al. [17] demonstrated that Wagoner's rate overestimated the impact of $^{16}\mathrm{O}(\mathrm{p},\alpha)^{13}\mathrm{N}$ in Type Ia supernova conditions. The widely used REACLIB compilation [6] includes the Caughlan & Fowler (1988) rate [64], but the theoretical methods employed were not detailed, and no uncertainty for the reaction rate is provided. In contrast, the STARLIB [65] rate, based on Hauser-Feshbach statistical models [36], has an uncertainty of approximately a factor of ten. This uncertainty arises from limitations in applying Hauser-Feshbach

models to light nuclei such as ^{17}F, where the assumption of high-level density is not valid.

In the absence of a well-constrained rate, SNIa models have had difficulty reproducing the observed calcium-to-sulphur Ca/S abundance ratios in supernova remnants across various progenitor metallicities [66], [67]. To address the discrepancy between observational data and models, Martinez-Pinedo et al. [68] retained the CF88 rate for the reaction $^{16}\mathrm{O}(\mathrm{p},\alpha)^{13}\mathrm{N}$ but reduced the competing $^{16}\mathrm{O} + {}^{12}\mathrm{C}$ reaction rate by a factor of 0.1. This adjustment effectively reduced the destruction of ^{16}O particles via carbon burning and improved the agreement with the observed Ca/S ratios. Conversely, Bravo [5] found that increasing the $^{16}\mathrm{O}(\mathrm{p},\alpha)^{13}\mathrm{N}$ rate by approximately seven times the REACLIB value better reproduced the Ca/S yields across different progenitor metallicities while keeping the $^{16}\mathrm{O}+{}^{12}\mathrm{C}$ rate at its original value. Figure 3.1 presents estimates for the $^{16}\mathrm{O}(\mathrm{p},\alpha)^{13}\mathrm{N}$ reaction rate from different compilations (CF88, WAG69, STARLIB), along with observational constraints suggested by Bravo, illustrated in a grey shade.

3.2 Evaluating the Available Experimental Cross-Section Measurements of the $^{16}\mathrm{O}(\mathrm{p},\alpha)^{13}\mathrm{N}$

This section presents a detailed evaluation of studies that have measured the cross-section of $^{16}\mathrm{O}(\mathrm{p},\alpha)^{13}\mathrm{N}$ reaction in energy ranges relevant to SNIa nucleosynthesis ($E_{\mathrm{cm}} \approx$ 6-8 MeV). The experimental cross-section data were compiled from the EXFOR database [69], yielding five relevant studies: Whitehead & Foster (1958) [70], McCamis et al. (1973) [71], Nero & Howard (1973) [72], Gruhle & Kober (1976) [73], and Sajjad et al. (1986) [74].

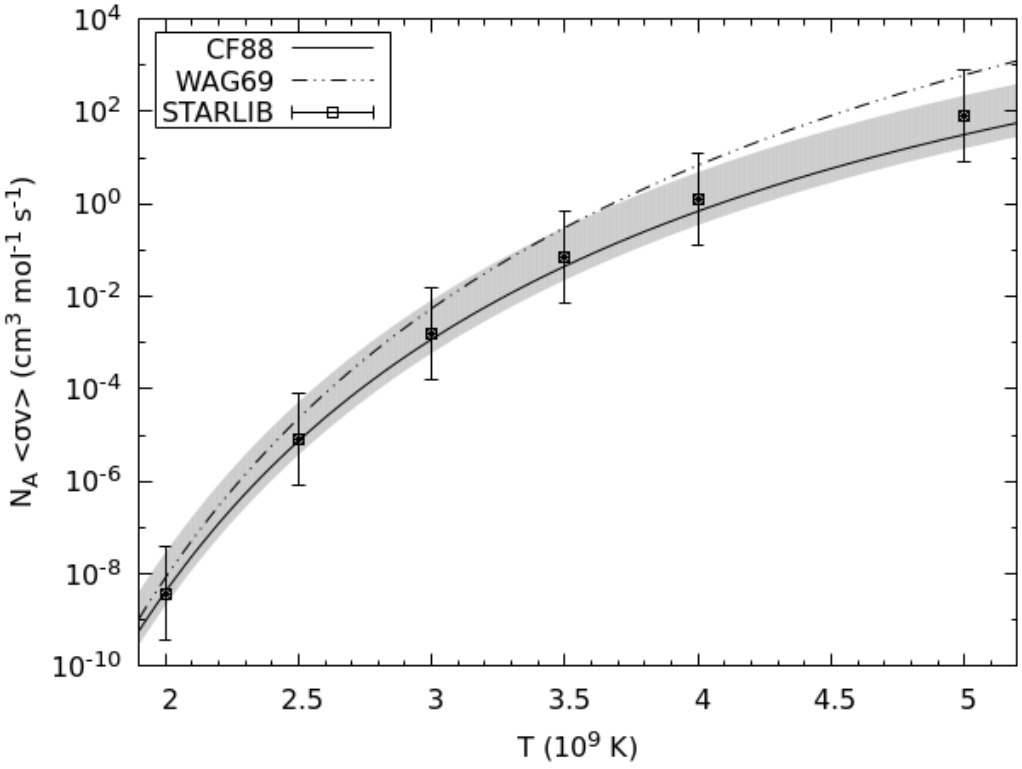

Figure 3.1: Reaction rate of $^{16}\mathrm{O}(\mathrm{p},\alpha)^{13}\mathrm{N}$ as a function of temperature (in GK), based on different compilations: Caughlan & Fowler (1988, CF88), Wagoner (1969, WAG69), and Sallaska et al. (2013, STARLIB). The uncertainty from the STARLIB compilation is represented by vertical error bars, while the shaded region denotes the uncertainty range inferred from observational studies of Ca/S and Ar/S mass ratios in supernova remnants. Figure adapted from [5].

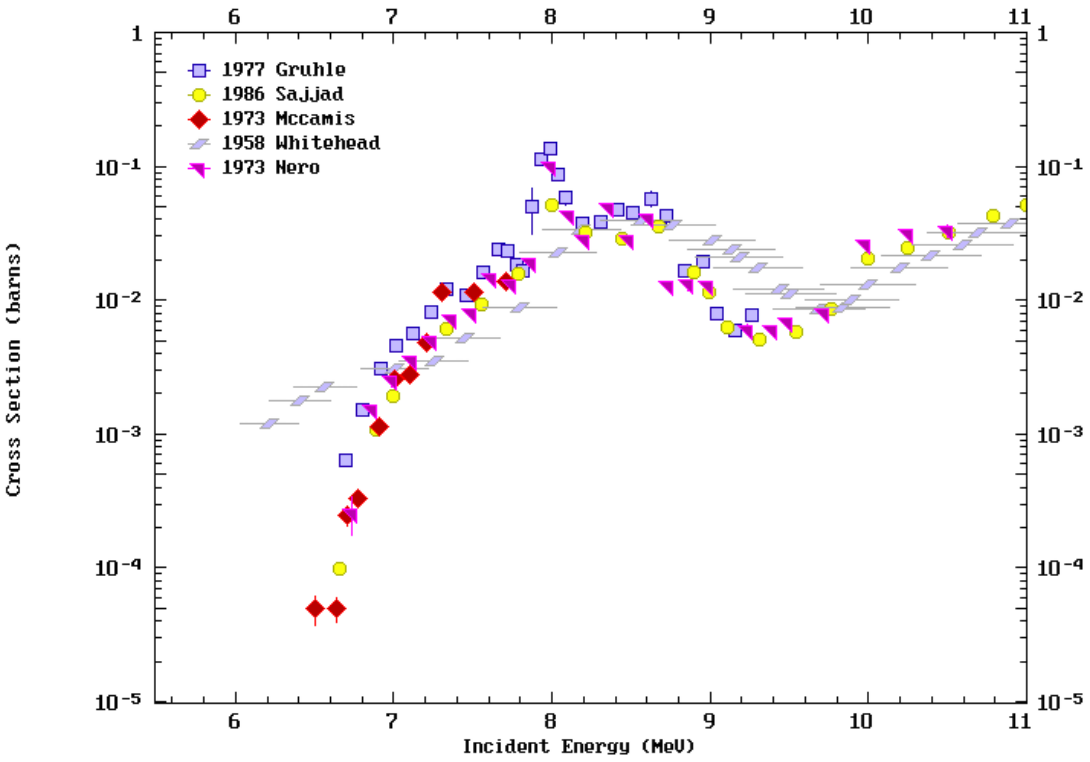

Figure 3.2: Experimental cross-section measurements of $^{16}\mathrm{O}(\mathrm{p},\alpha)^{13}\mathrm{N}$ extracted from the EXFOR database, showing five data sets: Gruhle (blue circles), Sajjad (orange squares), McCamis (green diamonds), Whitehead (red crosses), and Nero (purple Xs). The cross-section is plotted as a function of proton beam energy ($E_{\mathrm{lab}} = 5.8 - 10.5$ MeV). This plot was generated using the EXFOR Plotly2 tool [69].

Figure 3.2 shows the reported cross-sections from Gruhle, Sajjad, McCamis, Whitehead, and Nero, as reported in the EXFOR database.

Whitehead & Foster 1958

Whitehead & Foster [70] conducted measurements of the $^{16}\mathrm{O}(\mathrm{p},\alpha)^{13}\mathrm{N}$ cross-section using the McGill synchrocyclotron. Their experiment employed thin plastic foils of composition $C_4H_6O_2$ (Gelva) as targets, which were irradiated with the proton beam. Post-irradiation, the target foils were cut and mounted between aluminium disks for activity measurement. The annihilation radiation was detected using a NaI scintillation crystal. The cross-sections were normalised against the $^{12}\mathrm{C}(\mathrm{p},\mathrm{pn})^{11}\mathrm{C}$ reaction, with the initial energy determination having an accuracy of 3% and more precise relative energy spacing between points.

A contribution from the $^{13}\mathrm{C}$ $(\mathrm{p},n)^{13}\mathrm{N}$ reaction was detected and subtracted from the measurements; however, the cross-section of the $^{13}\mathrm{C}$ $(\mathrm{p},n)^{13}\mathrm{N}$ reaction used for this subtraction was later found to be inaccurately determined [74]. Furthermore, the target material of Gelva solid targets was found to experience a loss of activity during irradiation, which is consistent with observations from similar studies [75] [76]. Since Whitehead's study did not report the thickness of their foils, it was not possible to quantify the impact of this activity loss.

McCamis & Cameron (1973)

McCamis et al. [71] used a Van de Graaff accelerator to measure the $^{16}\mathrm{O}(\mathrm{p},\alpha)^{13}\mathrm{N}$ cross-section from threshold to $E_{\mathrm{cm}} = 7.7$ MeV. Their setup included a magnesium peroxide(MgO_2) target $300 - 400\mu\mathrm{g/cm}^2$ thick deposited on a thin Gold (Au) back-

ing, specifically prepared to minimise carbon contaminants, which could interfere with the reaction. Activity measurements were conducted using a NaI(Tl) scintillation counter. McCamis et al. reported that small amounts of ^{18}F and ^{11}C were produced during irradiation. These beta-emitting isotopes were accounted for by fitting the decay curves using their known half-lives.

Measurement uncertainties included detector efficiency$1.4-5\%$, target thickness determined by elastic proton scattering, and gamma counting statistics $2-16\%$. Additionally, McCamis incorporated data from Dangle [77] for energies above $E_{\mathrm{cm}} = 7.7$ MeV. The added cross-section points were obtained by integrating differential cross-sections extracted from Dangle's graphs. This process introduced large errors due to the integration procedure and graph-reading errors.

Notably, the derived reaction rate was calculated at $E_{\mathrm{cm}} = 7.6$ MeV under the assumption that contributions from higher energies were negligible for the $^{16}\mathrm{O}(\mathrm{p},\alpha)^{13}\mathrm{N}$ reaction rate in the explosive stage of Oxygen. In the absence of any sharp resonance, McCamis et al. reported a rate of $N_A < \sigma v >= 0.049\ \mathrm{cm^3\,s^{-1}\,mol^{-1}}$ at $T = 3.5\,\mathrm{GK}$. This value is significantly lower than previous predictions made by Wagoner [63].

Nero & Howard (1973)

Nero & Howard [72] measured the $^{16}\mathrm{O}(\mathrm{p},\alpha)^{13}\mathrm{N}$ cross-section in the centre-of-mass energy range of $5.4 \leq E_{\mathrm{cm}} \leq 9.9$ MeV using the ONR-CIT tandem accelerator. Their targets consisted of tungsten trioxide (WO_3) with natural isotopic composition, evaporated onto 0.5 mm thick tantalum blanks. The (WO_3) layer had a mass density of 4.0 mg/cm^2, and the ^{16}O content was measured with 10% accuracy. After irradiation with a proton beam, targets were transferred to an off-line annihilation

spectrometer, which counted coincidence pulses between two NaI(Tl) crystals to measure the 0.511 MeV annihilation γ-rays from ^{13}N positron decay. The energy loss of the proton beam in (WO_3) target was calculated using stopping power tables of ref. [78]. Cross-sections were calculated by subtracting the background activities of $^{16}O(\mathrm{p},n)^{18}F$ and the absorbed ^{16}O in the Ta packing material. An unexpected increase in cross-section below 6.2 MeV was noted, which was attributed to contamination from the ^{13}C p, $n)^{13}$N reaction. Hence, the data beyond 6.2 MeV was regarded as upper limits. The overall reported uncertainty in the cross-section is $\pm 15\%$, resulting from the target thickness and composition introducing an uncertainty of $\pm 10\%$, the spectrometer efficiency of $\pm 0.4\%$. Depending on the energy and cross-section magnitude, statistical uncertainties ranged from $2\% - 19\%$.

Gruhle & Kober (1976)

Gruhle & Kober [73] measured absolute cross-sections and deduced modified S-factors from threshold to 3 MeV above, using the Cologne FN tandem accelerator. The experiment utilised a target of O_2/N_2 gas to avoid carbon contamination. The gas was kept at pressures of $300 - 400$ mbar and a thickness of 12 mm behind a 5μm thick tantalum foil. After proton bombardment, the positron activity of the residual ^{13}N nuclei was detected using two 7.6×7.6 cm NaI(Tl) scintillation detectors. The reported sources of uncertainty in the measurements included an absolute calibration error of $\pm 9\%$ and a statistical error that ranged from $\pm 2\%$ at high energies, with the error increasing to $\pm 15\%$ at lower energies. Further information about systematic errors was not detailed. The computed reaction rate was much lower than Wagoner rates [63] in agreement with Woosley rates [17].

Sajjad, Lambrecht, & Wolf (1986)

Sajjad, Lambrecht, & Wolf [74] measured the $^{16}O(p,\alpha)^{13}N$ cross-section over an energy range of 6.5 MeV to 16.5 MeV, focusing on energies relevant to the production of ^{13}N for biological and clinical research. The experiments used the BNL Tandem Van de Graaff accelerator with an energy resolution of 2 keV.

The targets used consisted of a gas mixture of 2% NO_2 in O_2, contained in irradiation cells with aluminium foil windows. After irradiation, the absolute disintegration rates of ^{13}N were determined using a least-squares decay analysis program.

The uncertainty in the proton beam energy ranged from 85 keV at lower energies to 47 keV at higher energies. This variation was attributed to energy loss in the Faraday cup window, the target window, and the target gas. The overall uncertainty in the cross-section was 7%. This uncertainty resulted from several factors, including uncertainty in the target thickness(1%), challenges in transferring the active ^{13}N target(5%), variations in beam currents (1%), detector efficiency (4%), and activity loss in the walls($< 1\%$). A statistical uncertainty of 2% was included, derived from the analysis of the decay curves of ^{13}N.

IAEA evaluation

A recent evaluation by the International Atomic Energy Agency (IAEA) [79] assessed the $^{16}O(p,\alpha)^{13}N$ cross-section as part of a broader project on radionuclides used in positron emission tomography (PET). This evaluation compiled and analysed data from fourteen publications covering energies up to 35 MeV. The IAEA team employed Padé fits [80, 81] to the selected and corrected experimental data to derive a recommended cross-section, with uncertainties estimated using a Padé

least-squares method. A 4% systematic uncertainty was added to the estimated experimental uncertainties. The resulting Padé fit, using 40 parameters for 607 selected data points, yielded a χ^2 of 1.96 over an energy range up to 18 MeV. The uncertainties in the IAEA evaluation vary significantly with energy, ranging from 65% near the reaction threshold to below 7% for energies higher than 11 MeV [82]. Although this evaluation provides an additional point of comparison, its reliability may be limited due to several factors:

1. Some datasets, such as those of Whitehead [70] and Furukawa [83], appear to have been adjusted during the evaluation process without explicit experimental justification. While such modifications may aim to reduce the discrepancies, they introduce additional uncertainty regarding the accuracy of the fitted data.

2. The presence of poor-quality or inconsistent data can significantly affect the averaging process, potentially skewing the resulting cross-section values in energy regions with limited agreement.

3. The Padé fitting approach incorporates expert judgment in selecting and weighting datasets. In regions of substantial data scatter, this reliance may limit the objectivity of the final evaluation, especially in the absence of the experimental validation.

Therefore, caution should be exercised when using this evaluation for astrophysical rates.

3.3 Reaction Rate Calculation from Cross-Section Measurements

To evaluate the reaction rate of $^{16}\mathrm{O}(\mathrm{p},\alpha)^{13}\mathrm{N}$ from previous cross-section measurements, necessary assessments and adjustments must be applied to the cross-section data to address experimental issues and account for missing uncertainties. The dataset from Whitehead & Foster was excluded due to certain concerns regarding the reported data. Their reported cross-section values were substantially higher than all subsequent measurements near the reaction threshold, and no uncertainties were provided. Furthermore, the EXFOR database applied a downward shift of 0.3 MeV to their reported values without documented experimental justification. For the experimental data from McCamis et al. (1973), Nero and Howard (1973), Gruhle and Kober (1976), and Sajjad et al. (1986), the following corrections in the present work were implemented to the data points, based on the procedures documented in the original publications.

- Energy loss corrections were applied to the data from Nero. For each point, the tabulated energy was shifted to the bin midpoint by subtracting half of the reported energy loss value, i.e. $E \rightarrow E - \frac{1}{2}\Delta E$. Although ΔE values were provided in the original publication, they were not included in the EXFOR tables.

- Sajjad et al. reported a variation in beam energy resolution ranging from 0.7 to 0.8 MeV when the beam passed through the target. This range was used as the uncertainty on the energy ΔE. For centre-of-mass energies (E_{cm}) higher than 7 MeV, the ΔE was set at 0.75 MeV, and ΔE was set at 0.85 MeV for E_{cm} values below 7 MeV.

- Since Gruhle and McCamis did not provide any information about the energy

loss or resolution, the energy loss (ΔE) was estimated using the Stopping and Range of Ions in Matter (SRIM) code [56]. Furthermore, McCamis et al. cross-section data were limited to E_{cm} =7.7 MeV; additional data points of Dangel[77] were added, including E_{cm} =7.2, 7.4, 7.5, and 7.6 MeV.

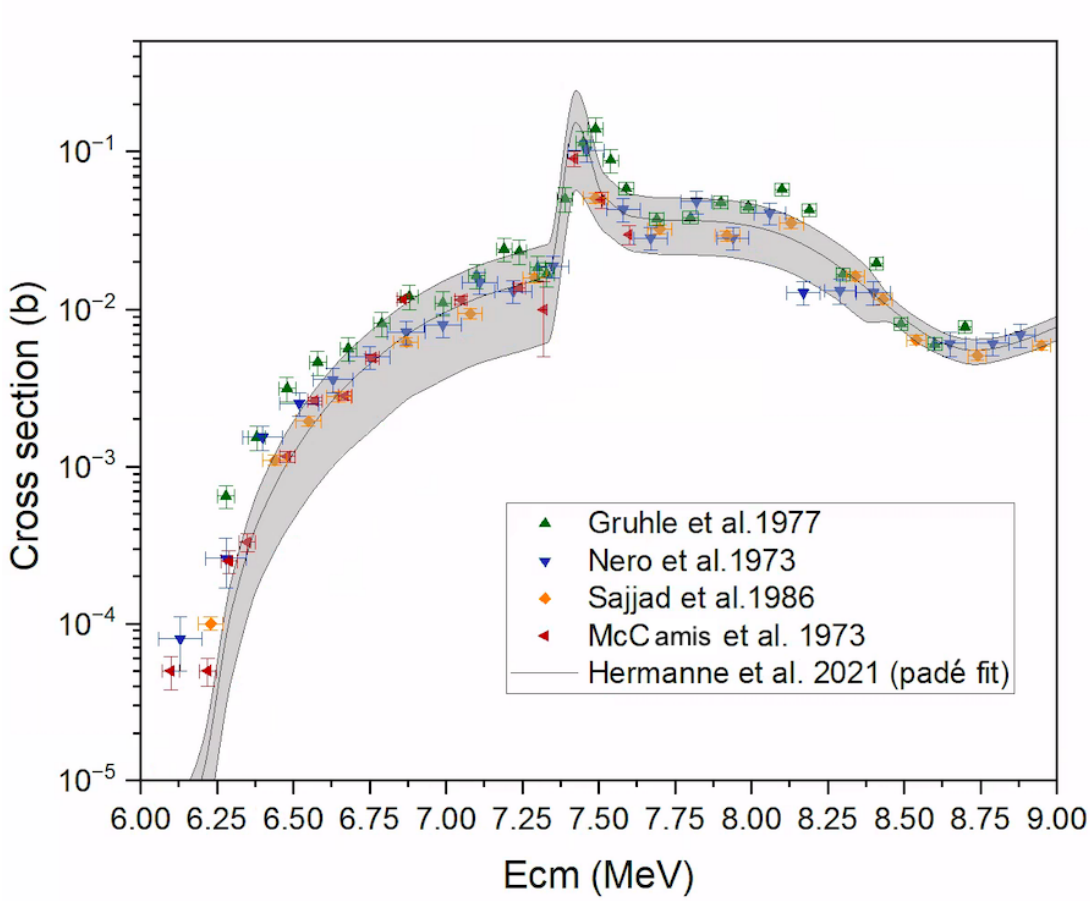

Figure 3.3: Experimental cross-section measurements for the $^{16}\mathrm{O}(\mathrm{p},\alpha)^{13}\mathrm{N}$ reaction as a function of centre-of-mass energy (in mb). Data points are shown for McCamis et al. (1973), Nero & Howard (1973), Gruhle & Kober (1976), and Sajjad et al. (1986). For the Gruhle and McCamis datasets, energy loss was estimated using SRIM. The purple line represents the Padé fit from the Hermanne et al. evaluation, with associated uncertainties indicated by the grey-shaded region.

Figure 3.3 shows good agreement among datasets at energies above 7.25 MeV. However, notable discrepancies appear at lower energies. Differences in resonance heights, absolute cross-section values, and resonance positions can be observed across the datasets. These inconsistencies may arise from background contributions at low energies, where activation and positron-counting techniques are particularly

sensitive to contamination. In several of the earlier measurements, any reaction producing ^{13}N could contribute to the observed β^+ activity and thereby distort the inferred cross sections. Relevant backgrounds include $^{13}\mathrm{C}(\mathrm{p},n)^{13}\mathrm{N}$ and $^{12}\mathrm{C}(\mathrm{p},\gamma)^{13}\mathrm{N}$. In addition, the production of ^{17}F introduces further complications, as its β^+ decay falls within the same activity window used to detect ^{13}N, potentially impacting the extracted yields.

To calculate the reaction rate, cross-section data from McCamis, Nero, Gruhle, Sajjad, and the Padé fit from the IAEA evaluation were used as input to the `Exp2Rate` code, which calculates reaction rates and associated uncertainties [84]. Comparing these rates to the CF88 rate reveals substantial discrepancies between datasets, with variations up to a factor of two at temperatures around 3 GK. As anticipated from the cross-section data, Gruhle and Nero's higher cross-sections yield elevated rates. Meanwhile, McCamis' and Sajjad's lower cross-sections result in lower rates with tighter uncertainties, failing to overlap with the higher data. These discrepancies prevent the derivation of a single recommended rate from the currently available cross-section data.

In addition, the rate derived from the recommended cross-section for $^{16}\mathrm{O}(\mathrm{p},\alpha)^{13}\mathrm{N}$ by the IAEA evaluation was calculated. This rate reveals higher uncertainty, ranging from 0.4 to 2 times the CF88 rate. This large uncertainty in the IAEA-derived rate can be attributed to two main factors: the use of a mathematical fit to a diverse set of data points and the inclusion of outdated measurements adjusted to match more recent data. The considerable variation in the rates calculated from older measurements illustrates the challenges in determining a definitive rate for this reaction based on currently available data.

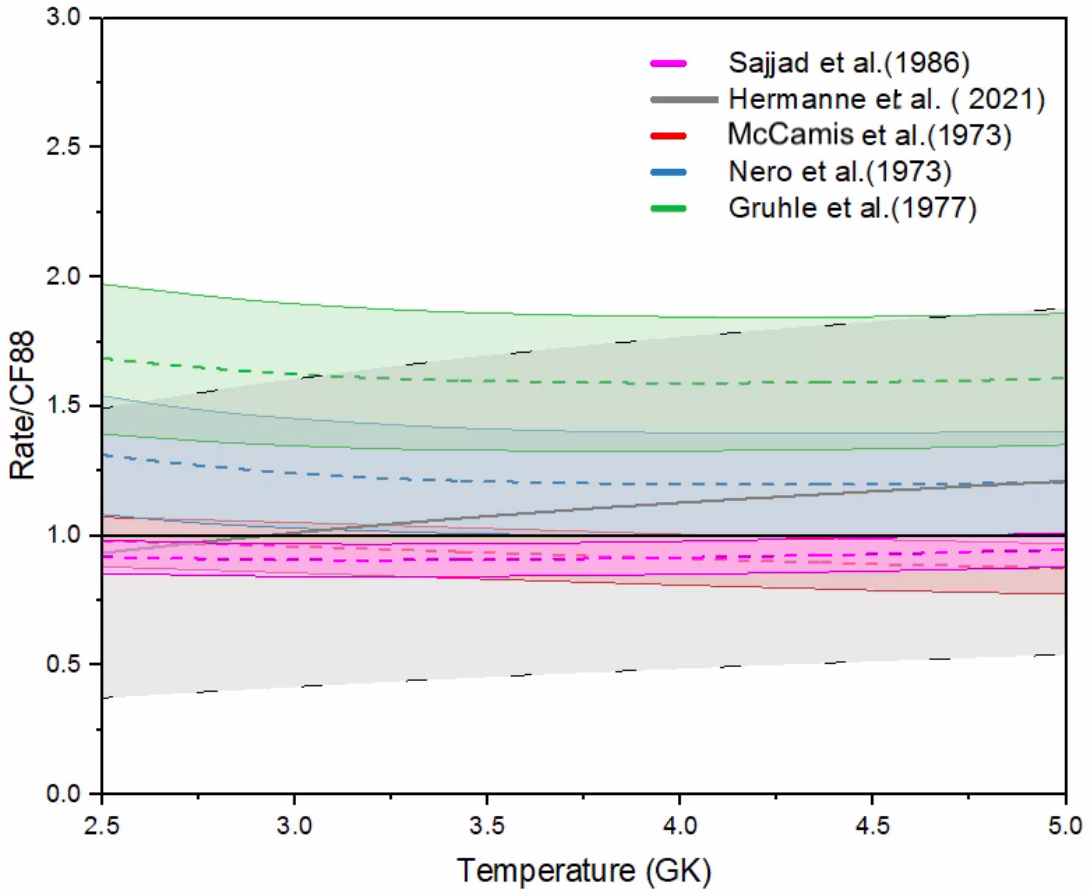

Figure 3.4: Reaction rates for $T = 2.5$–5 GK, relevant to Type Ia supernovae (SNIa), derived from the experimental datasets of Gruhle, McCamis, Nero, and Sajjad, as well as the evaluated Hermanne et al. (IAEA Padé fit), all normalised to the CF88 rate. The rates from McCamis (red) and Sajjad (magenta) remain within 0.8 times the CF88 rate, whereas those from Nero (black) and Gruhle (green) exhibit higher values, ranging between 1.1 and 2 times the CF88 rate.

3.4 Reaction Rate at Lower Temperature

For lower temperatures at a range of 0.1–1 GK relevant to CCSNe, a new rate evaluation was proposed by Meyer et al. [7]. This new rate was derived from analysing unbound states in the compound nucleus ^{17}F, using spectroscopic information from analogue states in ^{17}O. The Monte Carlo approach was used to provide a reaction rate with uncertainty using the code of RatesMC [85, 86]. A comparison between the experimental reaction rate and the Meyer rate is shown in Figure 3.5. Due to the limited available data at lower energy regions, existing experimental measurements for temperatures below 0.6 GK do not provide sufficient information on the rate. However, comparing the rates at temperatures higher than 0.6 GK highlights the substantial variation between the proposed rate by Meyer et al. and the rates from experimental cross section measurements. This variation reinforces the need for further experimental investigations. In particular, at energies above the α-threshold to reduce uncertainties and refine the reaction rate.

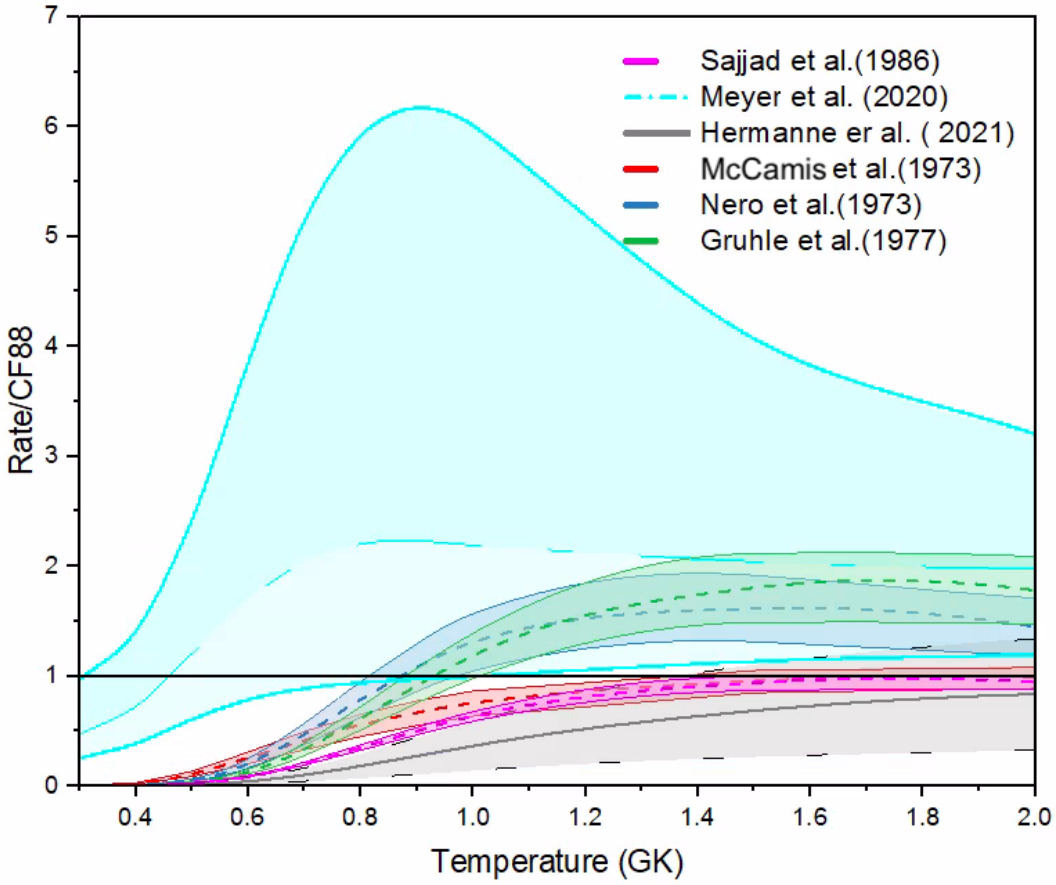

Figure 3.5: Reaction rates of $^{16}\mathrm{O}(\mathrm{p},\alpha)^{13}\mathrm{N}$ for $T = 0.1$–2 GK, relevant to Core Collapse supernovae (CCSN), normalised to the CF88 rate. The solid and dashed lines represent rates derived from experimental cross-section datasets using Exp2Rate, while the shaded regions indicate their respective uncertainties. The recently proposed rate by Meyer et al. (2020) is shown as a blue dash-dotted line, exhibiting a significant increase at $T \approx 0.6$ GK, with a broad uncertainty band (light blue). The evaluated rate from Hermanne et al. (IAEA Padé fit) is displayed in grey. Reaction rates extracted from experimental cross-section measurements by McCamis (red), Nero (black), Gruhle (green), and Sajjad (magenta) are also shown. The comparison highlights substantial discrepancies between the rate proposed by Meyer et al. and experimental constraints.

Chapter 4

Evaluation of ^{17}F States

4.1 Significance of the ^{17}F Levels Above the α-Threshold for CCSN Nucleosynthesis

As it was shown in Section 2.2, the $^{13}\mathrm{N}(\alpha,\mathrm{p})^{16}\mathrm{O}$ reaction strongly influences the fate of ^{13}N in the helium shell of core-collapse supernovae, shaping the production ratios of ^{13}C, ^{15}N, and ^{16}O observed in presolar SiC grains [7]. At $T = 0.4 - 1$GK, this reaction proceeds through resonant states in ^{17}F located above the α-threshold. Therefore, accurate information about these ^{17}F states (excitation energies, spins, and partial widths) is crucial for determining the competition between α-capture and β^+-decay of ^{13}N. Figure 4.1 shows the decay channels of the ^{17}F compound nucleus above the α-threshold, where the high Q-value of the α-decay channel causes the excited states of ^{17}F to favour the proton emission, i.e. $\Gamma_p \approx \Gamma_{\mathrm{tot}}$.

Consequently, the α-particle widths (Γ_α) become the dominant factor in determining how strongly each resonance influences the $^{13}\mathrm{N}(\alpha,\mathrm{p})^{16}\mathrm{O}$ reaction rate at the

energies relevant to CCSN helium shell nucleosynthesis. Despite the astrophysical significance of the ^{17}F states above α-threshold, key parameters such as energies, spins, parities, and partial widths remain uncertain.

This chapter provides a comprehensive analysis of the experimental studies of the ^{17}F level parameters above the α-threshold, focusing on their methodologies, assumptions, and sources of uncertainty. Additionally, the determined parameters were compared with direct $^{16}\mathrm{O}(\mathrm{p},\alpha)^{13}\mathrm{N}$ cross-section measurements using Azure2 to identify the current discrepancies and emphasise the need for better information on ^{17}F states.

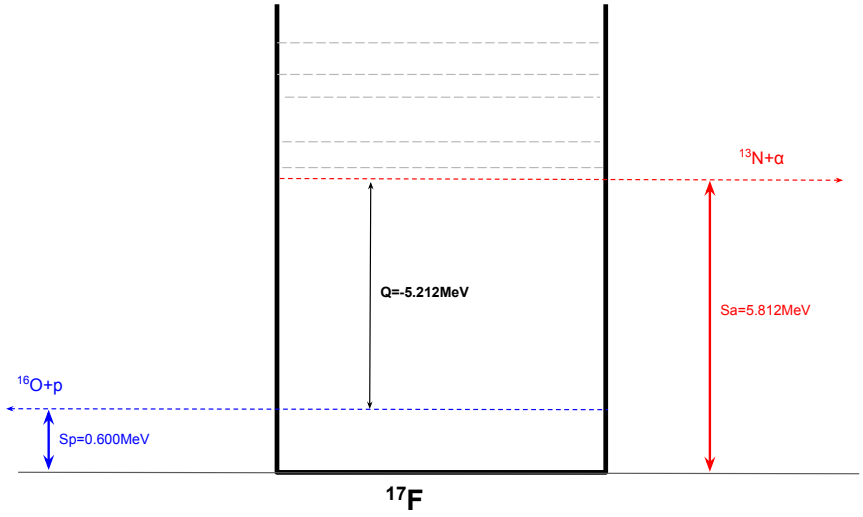

Figure 4.1: Energy levels of the ^{17}F compound nucleus. For the proton channel, the separation energy is $S_p = 0.600$ MeV, while for the α-channel it is $S_\alpha = 5.818$ MeV, resulting in a Q-value for $^{16}\mathrm{O}(\mathrm{p},\alpha)^{13}\mathrm{N}$ of $Q = -5.218$ MeV.

4.2 Review of ^{17}F Levels Above the α-Threshold: Limitations and Uncertainties

The spectroscopic information for the ^{17}F nucleus is documented in the NNDC database [87]. Most of the data within the range of $E_x = 5.2$ to 9.0 MeV come mainly from two experimental studies: Salisbury et al. [88, 89] and Dangle et al. [77]. However, many of these levels lack firm spin-parity assignments and have limited information about the alpha widths. In addition, uncertainties on the excitation energy, partial widths, and total widths are often missing or unreported.

4.2.1 Salisbury et al. (1962) Study for States at $E_p = 4.25$–7.6 MeV

Salisbury et al. measured differential cross-sections for the elastic scattering of protons on ^{16}O within the energy range $E_p = 4.25$–7.4 MeV, corresponding to excitation energies $E_x = 4.69$–7.5 MeV, using phase-shift analysis to determine resonance energies, spins, parities, and widths. A total of 22 resonances were identified.

The experiment used a tandem Van de Graaff accelerator to generate a proton beam with an energy spread of less than 3 keV. Scattered protons were detected using a CsI(Tl) scintillation detector, which achieved systematic uncertainties of $\pm 0.5\%$ for most cross-sections and $\pm 0.7\%$ at backward angles.

Several challenges were noted in the study. Several broad resonances, particularly around $E_p \approx 5.55$ MeV and $E_p \approx 6.33$ MeV, exhibited significant interference with neighbouring states, leading to multiple possible solutions for each state and discrepancies in phase shift assumptions. On the other hand, narrow resonances,

such as those at $E_p = 6.484$ MeV and $E_p = 6.564$ MeV, had widths comparable to the beam resolution, further limiting precision in their characterisation.

A key limitation of Salisbury's study is its exclusive focus on the elastic scattering channel in the analysis. By neglecting other channels, such as $^{16}\mathrm{O}(\mathrm{p},\alpha)^{13}\mathrm{N}$, the study fails to account for the contributions of the α-decay width (Γ_α) to the total width. This oversight may lead to an underestimation of the extracted total widths. Since the reaction rate calculations for $^{13}\mathrm{N}(\alpha,\mathrm{p})^{16}\mathrm{O}$ channels are sensitive to Γ_α, this limitation significantly affects the ability to constrain the $^{13}\mathrm{N}(\alpha,\mathrm{p})^{16}\mathrm{O}$ reaction rate at low energy above the threshold. Consequently, the phase shift interpretation of this study holds some uncertainty, and it remains unclear whether the reported width represents the total width or only the proton width.

4.2.2 Dangle et al. (1962) Study for States at $E_p = 7.18$–12.9 MeV

Building on Salisbury's work, Dangle et al. extended the investigation of ^{17}F resonances to $E_p = 13$ MeV and included additional reaction channels, such as $^{16}\mathrm{O}(\mathrm{p},\alpha)^{13}\mathrm{N}$ and $^{16}\mathrm{O}(\mathrm{p},\mathrm{p}')^{16}\mathrm{O}^*$.

While the experimental setup was broadly similar to Salisbury's, key refinements in the detection system were applied. The refinements included employing a solid-state detector with a smaller angular acceptance ($< 3.6°$) to achieve the resolution necessary for separating different proton states. In addition, thin nickel foils were used to help separate overlapping energy signals from the alpha and proton channels using the difference in energy loss (dE/dx) between alpha particles and protons. These modifications allowed the detection of multiple reaction channels.

Dangle et al. accounted for multiple sources of uncertainty: proton energy calibration errors ranged from 0.1% to 0.13% above 8 MeV; background subtraction contributed up to 5% error at lower energies; and target impurities (mainly hydrogen and nitrogen) impacted the cross-sections by as much as 0.52%. Statistical uncertainties spanned 1.2–25%, depending on the resonance strength.

A significant limitation reported in this study arose from their approach to parity assignments. Their parity assignments were based on the assumption that the 8.1 MeV state in ^{17}F is the mirror of the 7.75 MeV state in ^{17}O , relying on similarities in total widths. However, total widths are the sum of partial widths into different decay channels, which can vary significantly between mirror nuclei. Thus, while two resonances may exhibit comparable total widths, they may still differ substantially in nuclear structure if the partial widths are distributed differently across decay channels. This assumption was then extrapolated to other ^{17}F resonances, leading to multiple parity solutions for each state as more than one set of spin and parity assignments could accommodate the measured widths.

Additionally, both Salisbury et al. and Dangle et al. used a proton separation energy of $S_p = 596$ keV, which has been revised to $S_p = 600.27(25)$ keV based on more recent mass evaluations [90].

4.2.3 Spin-Parity Revisions for the $E_x = 6.699$ MeV and $E_x = 7.026$ MeV States in ^{17}F

Experimental limitations in Salisbury's work led to uncertainties in the spin-parity assignments of several ^{17}F states. In particular, the $E_x = 7.026$ MeV state ($E_p = 6.833$ MeV) was originally assigned $3/2^-$. However, subsequent γ-correlation studies suggested that 5/2 was more likely [91], motivating Darden & Hiddleston [92] to

ascertain the correct spin of this state. In their measurement, Darden & Hiddleston employed a polarised proton beam to record both cross sections and polarisations in the ^{16}O(p, p′)^{16}O reaction around $E_p \approx 6.8$ MeV. This approach overcame Salisbury's experimental limitation by incorporating polarisation-sensitive detectors and finer energy steps, enabling a more precise determination of the spin. As a result, they confirmed that the state is $5/2^-$, since only that assignment could accurately reproduce the observed excitation functions.

Similarly, the state of $E_x = 6.699$ MeV ($E_p = 6.482$ MeV) was initially assigned a spin-parity of $3/2^-$ in Salisbury's study. However, the authors noted a poor agreement between the fit and the experimental data. This state had a narrow width of 1.6 keV and the limited beam resolution of approximately 3 keV was insufficient for correct characterisation [93]. A subsequent investigation at the University of Wisconsin later demonstrated that the $3/2^-$ assignment was incorrect [94]. Finally, Sen [95] overcame these resolution limitations by deploying a polarised proton beam to measure both cross sections and polarisations near $E_p \approx 6.48$ MeV, thereby refining the characterisation of the $E_x = 6.699$ MeV state and confirming its revised spin-parity of $5/2^+$.

Table 4.1 presents the resonance parameters as reported by Salisbury et al. [88, 89], including excitation energies E_x, spin-parity assignments J^π, and measured widths. While Salisbury assigned an uncertainty of ±0.01 MeV to the proton energies, uncertainties on the extracted resonance widths were not explicitly provided.

Table 4.2 summarises the states properties measured by Dangle et al. [77] in the range $E_p = 7.58$–8.88 MeV. Dangle reported two possible reduced widths for each state, reflecting the uncertain spin–parity assignments. In the present work, these reduced widths were converted into partial widths ($\Gamma_{p0}, \Gamma_{p1}, \Gamma_\alpha$). For states where a preferred solution exists, only the corresponding partial widths are adopted; where

no preference is indicated, both solutions are retained. Uncertainties were reported only for the total widths in the original work, limiting the precision of the derived partial widths.

Table 4.1: Excitation energies and properties of ^{17}F states above the α-threshold reported by Salisbury et al.

E_p[a] (MeV)	E_x[b] (MeV)	J^π	Total Width Γ_{lab} (MeV)	Notes
4.787	5.106	$3/2^+$	1.63	Very broad, sub-threshold state
5.546	5.824	$3/2^+$	0.191	Interference with 5.101 MeV state
5.779	6.039	$1/2^-$	0.03	Narrow and isolated
6.332	6.560	$1/2^+$	0.216	Very broad, uncertain width and spin
6.484[c]	6.703	$5/2^-$	0.0017	Width comparable to beam resolution
6.564	6.778	$3/2^+$	0.0048	Width comparable to beam resolution
6.833[d]	7.037	$5/2^+$	0.0040	Very narrow
7.313	7.482	$3/2^+$	0.45	Very broad, significant contribution
7.381	7.551	$7/2^-$	0.027	Narrow and well-defined

[a] All E_p values in Salisbury et al. were reported with an uncertainty of ± 0.01 MeV.
[b] E_x values are recalculated using: $E_x(^{17}\text{F}) = (16/17) \times E_{\text{lab}} + 0.60027\,\text{MeV}$.
[c] Taken from [95].
[d] Taken from [92].

4.2.4 Evaluation of ^{17}F States by Meyer et al. (2020) from $E_x = 5.6$ to 8.2 MeV

In 2020, Meyer et al. [7] presented a new evaluation for the reaction rate of $^{13}\text{N}(\alpha, p)^{16}\text{O}$ by utilising updated resonance parameters for ^{17}F. Instead of only focusing on the states within the Gamow window for temperatures between 0.4 and 1 GK, they expanded their analysis to a wider excitation energy range. This wider energy range of ($E_x = 5.6$ to 8.2 MeV) accounts for possible contributions from the tails of broad resonances outside the Gamow window.

A major challenge in calculating the rate arises from the absence of direct measurements of α-widths (Γ_α), which strongly influence the reaction rate. To address this, Meyer et al. primarily relied on mirror symmetry assumptions to estimate

Table 4.2: Excitation energies and partial widths of ^{17}F above the α-threshold states deduced from Dangle et al.

E_p[a] (MeV)	E_x[b] (MeV)	J^π	Γ_{p0}[c] (keV)	Γ_{p1}[d] (keV)	Γ_α[d] (keV)	Total Width[e] (keV)
7.58	7.753	$1/2^+$	134	34	10	179(28)
7.58	7.753	$1/2^+$	135	10	33	179(28)
7.94	8.073	$5/2^+$	82	9	12	103(19)
8.1	8.224	$3/2^-$	633	46	26	705(235)
8.27	8.384	$5/2^-$	10	1	0.4	11(5)
8.27	8.384	$5/2^-$	9	1	1	11(5)
8.31	8.421	$7/2^+$	41	0.2	1	42(9)
8.63	8.723	$15/2^+$	181	-	7	188(28)
8.63	8.723	$15/2^+$	112	-	76	188(28)
8.88	8.958	$5/2^-$	118	3	2	122(19)
8.88	8.958	$5/2^-$	116	4	3	122(19)

[a] Some states appear twice when no preferred parity assignment was clear.

[b] E_x values recalculated as: $E_x(^{17}\mathrm{F}) = (16/17) \times E_{\mathrm{lab}} + 0.60027\,\mathrm{MeV}$.

[c] Γ_{p0} is calculated as: $\Gamma_{p0} = \Gamma_{\mathrm{total}} - (\Gamma_{p1} + \Gamma_\alpha)$.

[d] Values derived from Table 2 in [77], using: $\Gamma_\nu = 2P\left(\frac{\gamma_0^2}{\Delta P}\right)\left(\frac{\Delta P}{a}\right)$ and converted in to (C-M) system.

[e] Total width taken from Table 3 in Dangle and converted into (C-M).

[f] The total widths reported here were taken directly from Dangle, while the partial widths were reconstructed from the reduced widths. Because the exact penetrability definition used in the original analysis is not fully specified, the reconstructed partial widths do not exactly sum to the published total widths. The deviations are small ($\leq 2\%$) and have no impact on the subsequent analysis.

these missing widths.

To determine the mirror parameters, Meyer et al. used earlier measurements from the ^{13}C(^{7}Li,t)^{17}O transfer reaction, which had been performed at the Tandem-ALTO facility [96]. In the experiment, a 34 MeV $^{7}Li^{3+}$ beam bombarded a self-supporting enriched ^{13}C target. The resulting triton projectiles were analysed using a magnetic spectrometer and a focal-plane detection system. The spectra obtained provided excitation energies for ^{17}O states with a resolution of 50 keV. The resulting differential cross-sections were analysed using the finite-range distorted-wave Born approximation (FR-DWBA), yielding α-spectroscopic factors (C^2S_α) and partial widths (Γ_α) for ^{17}O.

For each ^{17}F level with possible analogue in ^{17}O, Meyer et al. assumed mirror symmetry, pairing states based on spin, parity, and consistency of total, and partial widths. The α-spectroscopic factor for ^{17}F then was calculated as $C^2S_\alpha(^{17}\mathrm{F}) = C^2S_\alpha(^{17}\mathrm{O})$.

An overall uncertainty factor of 2.5 was assigned on the α-widths of ^{17}F inferred from mirror symmetry. This uncertainty reflects two factors of: a 50% uncertainty in the spectroscopic factor from the transfer reaction, and an additional factor of 2 uncertainty associated with the mirror symmetry assumption.

For ^{17}F states without an identified analogue in ^{17}O, the α-width was statistically estimated from a Porter-Thomas distribution, adopting $\langle\theta^2\rangle = 0.04 \pm 0.02$following the approach of Pogrebnyak et al. [97].

Additionally, for states previously studied by Dangle et al. [77], reduced widths were taken from their analysis and converted to partial widths for the p_0, p_1, and α channels. A conservative 20% uncertainty was assumed for proton widths when

explicit uncertainties were unavailable.

To evaluate the impact of these revised parameters on the reaction rate, Meyer et al. employed a Monte Carlo method using the `RatesMC` code to propagate uncertainties from excitation energies, spin-parity assignments, and partial widths into the reaction rate. The resulting rate exhibited a total uncertainty of approximately a factor of 3, with the dominant contributions arising from the states of $E_x = 6.036$, $E_x = 6.560$, and $E_x = 6.778$ MeV.

Table 4.3: Selected ^{17}F states from Meyer et al. [7]. The width source indicates whether Γ_α was inferred using mirror symmetry (Mirror), estimated from a statistical model (Assumed), or directly measured (Measured).

E_x (MeV)	J^π	Γ_α (keV)	Γ_{p0} (keV)	Γ_{tot} (keV)	α-width Source
5.820 (20)	$3/2^+$	6.92×10^{-283}	180	180	Assumed
6.039 (9)	$1/2^-$	2.63×10^{-13}	28	28	Mirror
6.560 (20)	$1/2^+$	1.88×10^{-3}	200	200	Mirror
6.778 (20)	$(3/2^+)$	3.00×10^{-2}	4.47	4.5	Assumed
7.031 (20)	$5/2^-$	3.59×10^{-2}	3.76	3.8	Mirror
7.361 (20)	$(3/2^+)$	2.20	7.20	9.4 (19)	Assumed
7.483 (20)	$3/2^+$	4.64	790.36	795	Mirror
7.551 (20)	$7/2^-$	1.10×10^{-2}	29.98	30	Mirror
7.753 (40)	$(1/2^+)$	11	135	180 (28)	Measured*
8.073 (30)	$5/2^+$	14	79	104 (19)	Measured
8.224 (40)	$3/2^+$	25	636	706 (235)	Measured

* The small differences in partial width values between Meyer's study and Table 4.2 (less than 1.2%) are likely resulted from variations in the definition of the penetrability factor used to convert reduced widths into total widths.

4.3 Evaluation of Discrepancies Between Meyer's Spectroscopic Parameters of ^{17}F and The Experimental $^{16}\mathrm{O}(\mathrm{p},\alpha)^{13}\mathrm{N}$ Cross-Section measurements

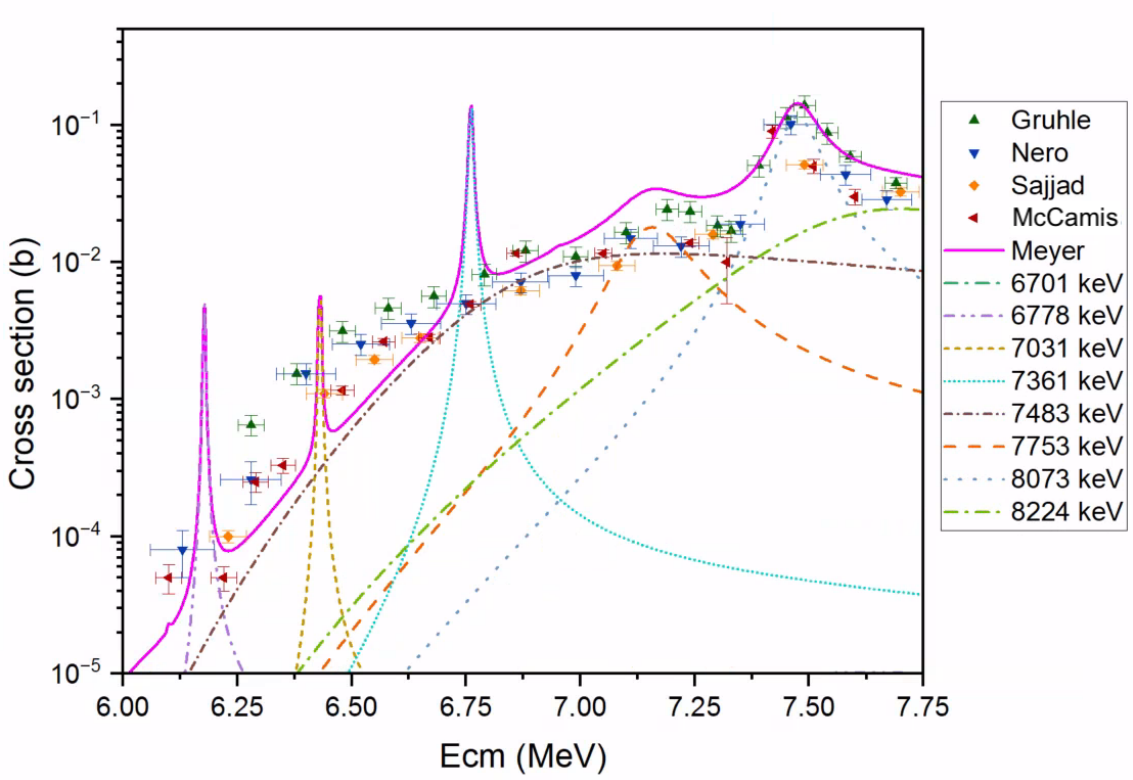

Figure 4.2: Comparison of the theoretical cross-section from Meyer et al.'s $\mathcal{R}$-matrix fit (based on spectroscopic parameters) with experimental cross-section measurements from Gruhle, Nero, Sajjad, and McCamis.

In addition to calculating the reaction rate for $^{13}\mathrm{N}(\alpha,p)^{16}\mathrm{O}$, Meyer et al. used the AZURE2 $\mathcal{R}$-matrix code to generate theoretical cross sections based on the spectroscopic information of ^{17}F. Figure 4.2 presents these calculated cross sections, converted into the $^{16}\mathrm{O}(\mathrm{p},\alpha)^{13}\mathrm{N}$ direction, with the individual resonance representation. A comparison with experimental datasets from Gruhle, Nero, Sajjad, and McCamis reveals significant discrepancies, which can be categorised into three key trends:

1. High-Energy Region ($E_{\text{cm}} = 6.8 - 7.0$ MeV): Experimental cross sections tend to be lower than those predicted by Meyer's parameters.

2. Intermediate-Energy Region ($E_{\text{cm}} < 6.75$ MeV): The broad resonance at $E_x = 7.483$ MeV appears systematically higher in experimental measurements.

3. Missing Narrow Resonances: The sharp resonances at $E_x = 7.361$ MeV and $E_x = 6.778$ MeV are not clearly observed in the experimental data.

4.3.1 Fitting α-Particle Widths to Experimental Data Using AZURE2

An attempt was made to constrain the unmeasured α-widths reported by Meyer using experimental data. The AZURE2 $\mathcal{R}$-matrix code was used to fit the unmeasured Γ_α values against the available experimental data, and the results of the fitted α-widths are summarised in Table 4.4.

For the fitting procedure, the resonance parameters from Meyer et al. were used as the initial input for AZURE2. The excitation energies (E_x) and measured total widths were held constant to minimise the number of free parameters. Only the Γ_α values of unmeasured states were allowed to vary, while proton widths were fixed at the values reported by Meyer. To assess the variation across different experimental measurements, fits were performed separately for each dataset (Gruhle, Nero, Sajjad, and McCamis). The low-lying states at $E_x = 5.82$ MeV and $E_x = 6.039$ MeV were kept fixed at Meyer's values, as no experimental data were available in this range to constrain them.

Figure 4.3 presents a comparative visualisation highlighting the deviations of the α-widths from Meyer's predictions. While some broad resonances, such as $E_x =$

Table 4.4: Fitted α-particle widths (Γ_α) for unmeasured ^{17}F states, obtained from AZURE2 fits to individual experimental datasets (McCamis, Nero, Sajjad, Gruhle). The last column lists the total width (Γ_{tot}) for each state.

State E_x (MeV)	McCamis (keV)	Nero (keV)	Sajjad (keV)	Gruhle (keV)	Total width (Γ_{tot}) (keV)
6.560	2×10^{-3}	5×10^{-3}	5×10^{-4}	2×10^{-3}	200
6.701	6.4×10^{-5}	1.9×10^{-2}	7×10^{-2}	1.4×10^{-2}	4.5
6.778	4.1×10^{-2}	2×10^{-3}	2×10^{-3}	2.2×10^{-1}	3.8
7.031	1×10^{-2}	3.35×10^{-1}	4×10^{-2}	3.8×10^{-1}	9.4(19)
7.361	8.07×10^{-4}	6.39×10^{-1}	3.5×10^{-3}	2.5×10^{-1}	795
7.483	2.4	2.9	3.6	5.4	30
7.551	1.7	4×10^{-5}	5×10^{-7}	2.8×10^{-1}	30

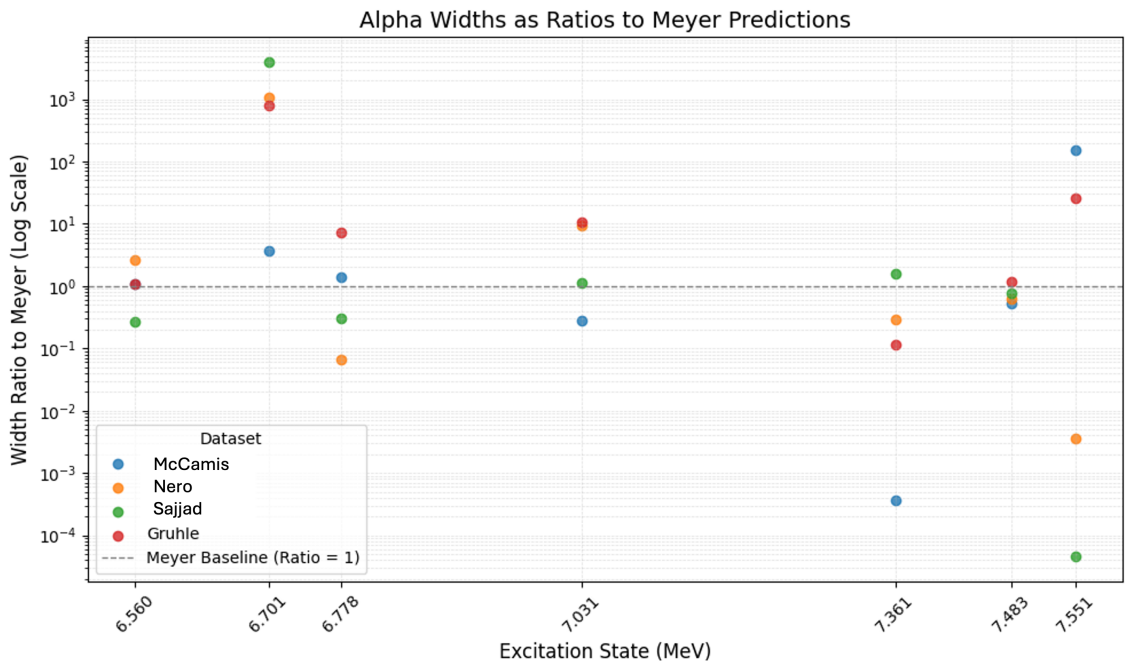

Figure 4.3: Comparison of α-particle widths (Γ_α) for key ^{17}F states, showing AZURE2-fitted values from experimental datasets (McCamis, Nero, Sajjad, and Gruhle) as a ratio to Meyer's assumed α-widths.

6.560 MeV and $E_x = 7.483$ MeV, showed relatively minor variation, other states, notably $E_x = 7.361$ MeV and $E_x = 7.551$ MeV, displayed significant differences, with Γ_α values varying by factors of 4 to 7 across datasets. These discrepancies in the fitted α-widths values highlight the difficulty of constraining Γ_α using experimental data. Moreover, the lack of strong agreement between experimental datasets and existing resonance parameters raises questions about the reliability of using the current ^{17}F states parameters in the rate calculation.

4.3.2 The Impact of Interference on the $^{16}\mathrm{O}(\mathrm{p},\alpha)^{13}\mathrm{N}$ Reaction at Energies Near the α-Threshold

Since fitting the α-widths of individual resonances alone was insufficient to fully constrain the parameters required for the ratesMC [98] code, as done in Meyer's work, an alternative approach was adopted. This method aimed to generate a new cross-section that better aligns with existing data while extending into the lower energy region relevant to hydrogen ingestion in the He-shell during the core-collapse supernova shock wave.

To achieve this, AZURE2 was used to reconstruct the total cross-section based on Meyer's parameters, with the following considerations:

1. Inclusion of interference effects between broad resonances, particularly in energy regions with overlapping states ($E_x = 5.2$–7.55 MeV).

2. Incorporation of the sub-threshold state at $E_x = 5.100$ MeV ($\Gamma = 1$ MeV), which Salisbury suggested may strongly interfere with the neighbouring broad $3/2^+$ broad resonance at $E_x = 5.821$ MeV ($\Gamma = 0.200$ MeV).

3. Systematic variation of interference signs (constructive or destructive) to explore how different states interact and influence the total cross-section.

These interference effects were not included in Meyer's cross-section calculations, potentially contributing to the discrepancies observed in Figure 4.2.

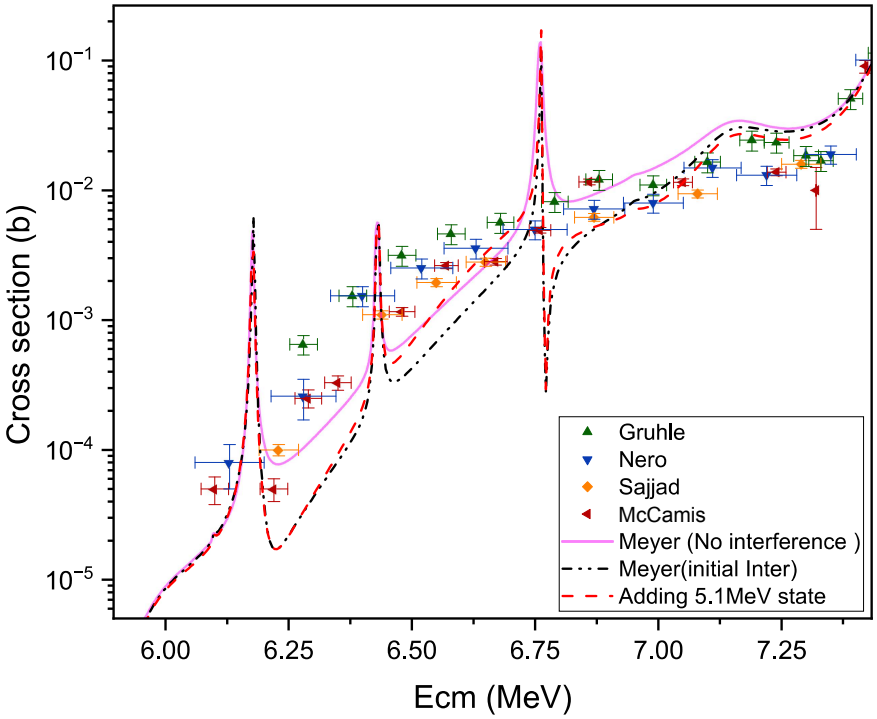

Figure 4.4: Impact of interference from broad resonance overlap and sub-threshold states on the total cross-section, calculated using AZURE2. The black dashed dotted line is Meyer cross section when including interference.The red dashed line represents the effect of adding the 5.1 MeV state, showing its contribution to the interference pattern.

By accounting for interference effects, as shown in Figure 4.4, the agreement with experimental data improved, particularly at $E_{\text{cm}} > 6.75$ MeV, where Meyer's calculations had underestimated the cross-section.

To further refine the cross-section, multiple interference signs were tested for each state. It was found that the states at $E_x = 6.56$ MeV and $E_x = 7.753$ MeV

($J^{\pi} = 1/2^{+}$) exhibited strong mutual interference, while the states at $E_x = 6.778$, $E_x = 7.361$, and $E_x = 7.482$ MeV also interacted significantly.

Notably, choosing destructive interference for the $E_x = 6.56$ MeV and $E_x = 6.778$ MeV states, with an associated 30% uncertainty, refined the overall shape of the resulting cross-section as can be seen in Figure 4.5. Azure2 input for this new cross section is represented in table 6.1. Moreover, the updated uncertainty band captured all available experimental data. Figure 4.6 compares the recalculated $\mathcal{R}$-matrix cross section, obtained using the modified Meyer resonance inputs, with the original Meyer calculation without interference. The comparison is shown in terms of the astrophysical S-factor in the inverse $^{13}\mathrm{N}(\alpha, \mathrm{p})^{16}\mathrm{O}$ direction to facilitate visualisation of the resonant structure and highlight the impact of the applied corrections.

Despite some remaining discrepancies and the absence of new insights into the nuclear states, this analysis offers a conservative approach for constraining the cross-section at lower energy regions. The experimental data were used to refine the interference pattern in Meyer's cross-section by exploring interference scenarios and selecting those that reproduce the measured cross-section most accurately. The necessary modifications applied to achieve this agreement were then used to define an uncertainty range. Finally, a new cross-section was generated by adjusting Meyer's cross-section within this uncertainty band, ensuring a more reliable extrapolation into the unmeasured energy range.

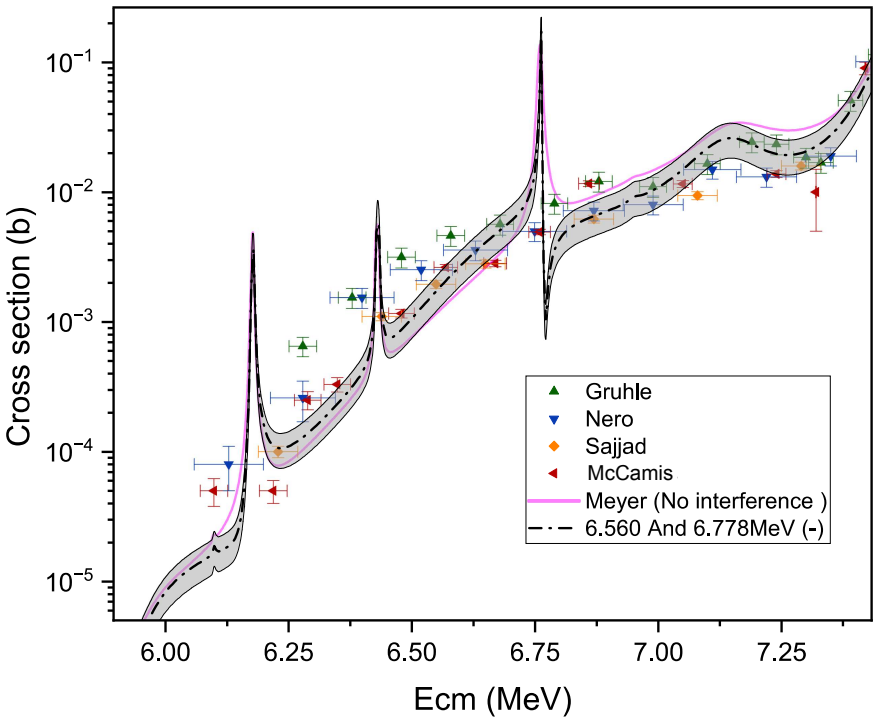

Figure 4.5: Recalculated $^{16}\mathrm{O}(\mathrm{p},\alpha)^{13}\mathrm{N}$ cross section obtained with AZURE2 using the resonance parameters adopted from Meyer *et al.*, after applying the corrections implemented in the present work. These corrections include the assignment of interference signs for overlapping broad resonances and the inclusion of the $E_x = 5.100$ MeV state. The shaded band indicates the uncertainty range derived by comparing the calculated cross section to available experimental data.

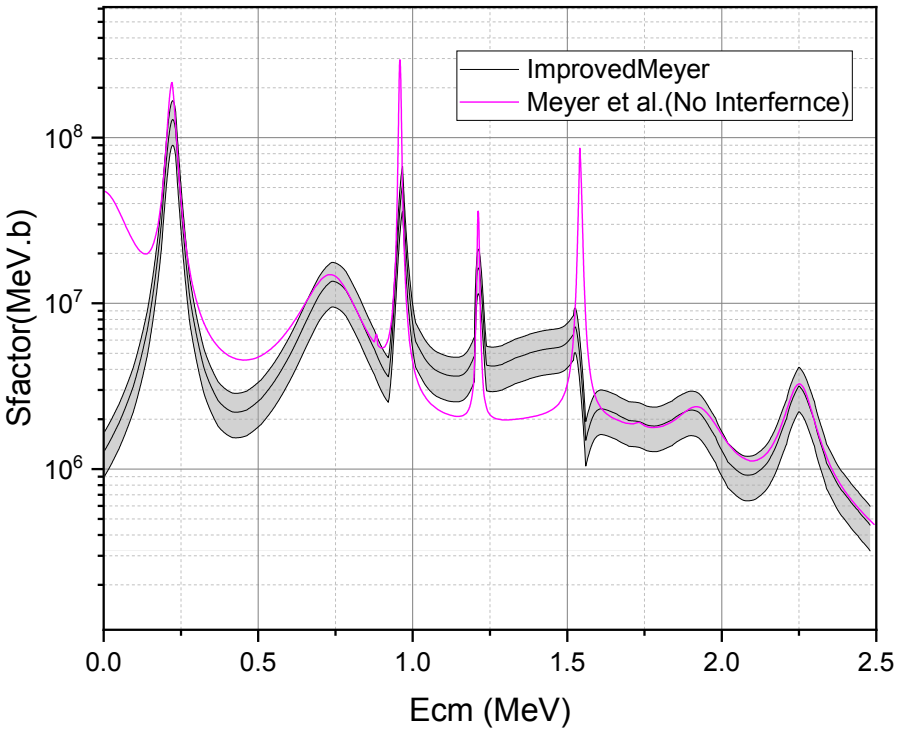

Figure 4.6: Astrophysical S-factor for the inverse reaction $^{13}\mathrm{N}(\alpha,\mathrm{p})^{16}\mathrm{O}$. The solid black curve shows the recalculated cross section obtained in the present work using corrected Meyer resonance parameters, including the chosen interference signs and the addition of the $E_x = 5.100$ MeV state. The shaded band represents the uncertainty range derived from comparison with experimental data. The magenta curve corresponds to the original Meyer calculation without interference.

4.4 Summary and Conclusion

This chapter presented an extensive analysis of the resonance parameters of ^{17}F states above the α-threshold for their role in determining the $^{13}\mathrm{N}(\alpha, p)^{16}\mathrm{O}$ reaction rate. A review of previous experimental measurements of ^{17}F states reveals significant uncertainties in excitation energies, widths, and spin-parity assignments. While employing mirror symmetry to predict α-widths has proven useful in situations where direct measurements are unavailable, the significant uncertainties in ^{17}F resonance parameters and their disagreement with measured cross-sections hinder the reliability of reaction rate calculations based on current ^{17}F resonance parameters. Furthermore, this study demonstrated that interference effects play a crucial role in shaping the reaction cross-section, particularly for broad resonances such as those at $E_x = 6.560$MeV and $E_x = 7.753$MeV. The lack of precise spin constraints for these states introduces further uncertainties in their interference contributions, underscoring the necessity of improved constraints on their quantum properties.

These findings reinforce the need for high-precision experimental measurements to refine spin-parity assignments, partial widths, and the characterisation of ^{17}F states above α-threshold. Addressing these uncertainties will be essential for accurately determining the $^{13}\mathrm{N}(\alpha, \mathrm{p})^{16}\mathrm{O}$ reaction rate in astrophysical environments.

Chapter 5

MUSIC experiment

5.1 Overview of the MUSIC Detector Structure

The Multi-Sampling ionisation Chamber (MUSIC) [99] detector is an advanced active target system. Originally developed for relativistic heavy-ion measurements in the late 1980s [100], MUSIC detectors have recently been successfully employed in various nuclear reaction studies. These include fusion reactions [101], as well as (α, p) [102] and (α, n) reactions [103]. The MUSIC detector at Argonne National Laboratory is housed within the Argonne Tandem Linac Accelerator System (ATLAS) [104] in a compact aluminium box of 30 cm (L) $\times$ 10 cm (W) $\times$ 20 cm (H). The chamber can be filled with various gases, such as helium, methane, neon, or argon, depending on experimental requirements. MUSIC uses the active target system, in which the gas in the chamber serves as the target material for nuclear reactions and as the counting gas for detecting reaction products. The active gas volume is contained with a cathode plane at the bottom (typically at negative high voltage), a Frisch grid above the drift region, and a segmented anode plane located at the

top (near ground potential). The beam enters and exits the chamber through thin titanium (Ti) windows (1.3 mg/cm^2 thickness) along the beam axis. For energy calibration purposes only, a silicon (Si) detector was installed at 0° along the beam axis downstream of the MUSIC detector (See Figures 5.1 and 5.2).

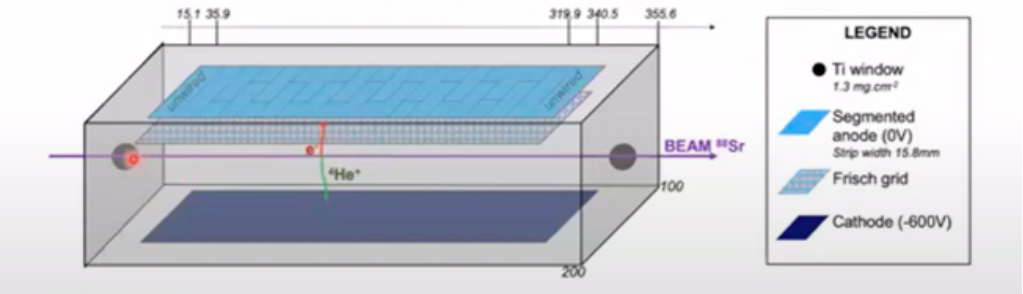

Figure 5.1: Schematic three-dimensional representation of the MUSIC detector geometry, illustrating the segmented anode plane on the top, the cathode plane on the bottom, the Frisch grid, and the beam axis through the entrance and exit titanium windows [105].

A key feature of the MUSIC detector is its segmented anode structure, which enables multi-sampling along the particle trajectory. The anode plane is divided into 18 strips in total: the first and last strips (S_0 and S_{17}) serve as control strips (not used in this experiment), while the central 16 strips constitute the active detection region, as illustrated in Figure 5.3 and Figure 5.4. This segmentation allows MUSIC to measure the energy-loss at multiple positions inside the gas volume. The 16 active strips are further split into left and right halves, which function as a multiplicity filter providing spatial information on the different ionisation patterns.

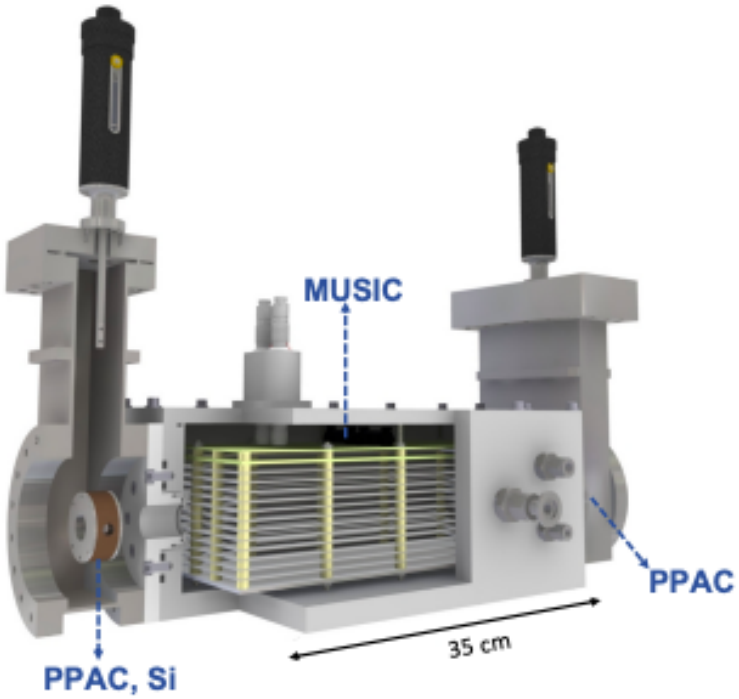

Figure 5.2: External view of the MUSIC detector, showing its overall structure. Both the silicon detector and the PPAC could be removed when needed [106].

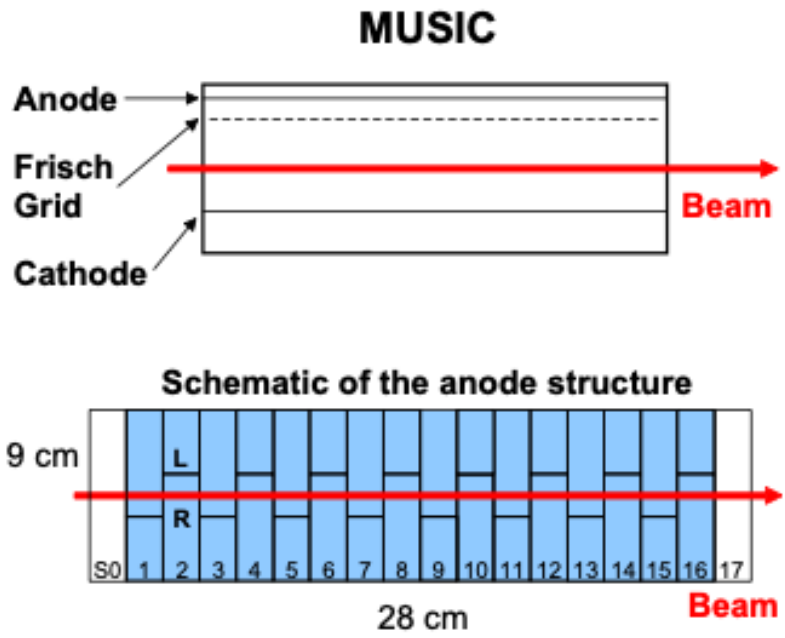

Figure 5.3: Schematic layout of the MUSIC detector anode structure. The upper panel shows a lateral view of the detector, indicating the relative positions of the anode plane, Frisch grid, and cathode. The lower panel shows the segmented anode geometry, including the left and right segments of each strip, the strip numbering, and the active length of the detector along the beam axis [99].

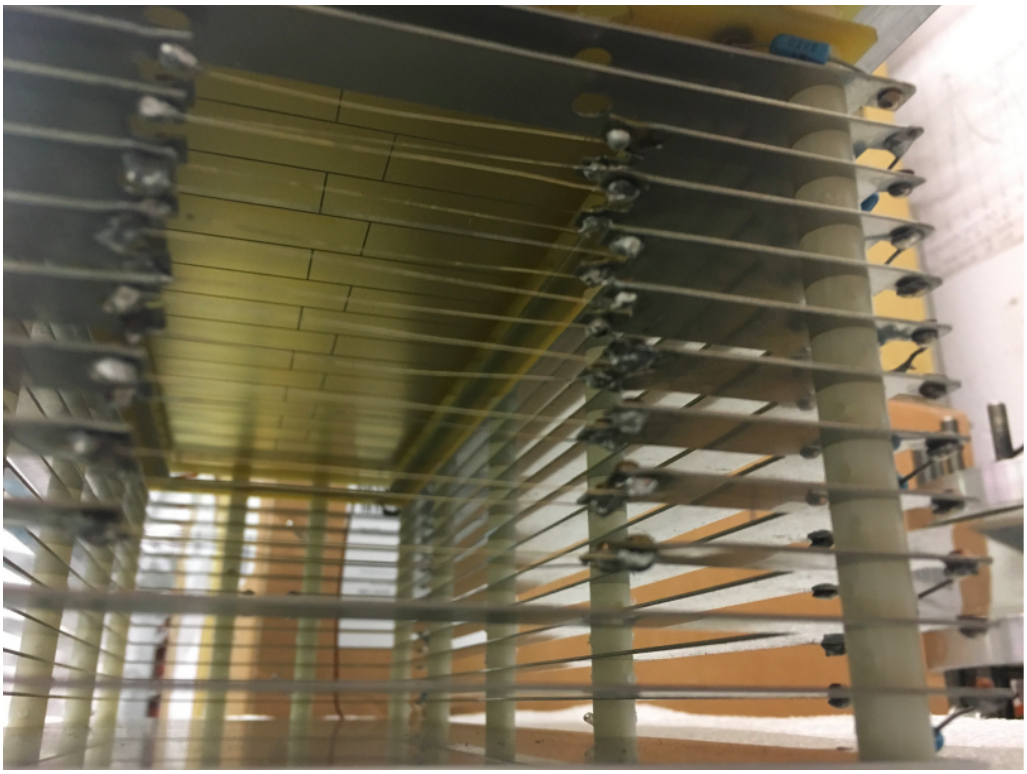

Figure 5.4: Downstream view of the MUSIC detector showing the segmented anode structure at the top. Field shaping rings create a voltage gradient that directs electrons toward the anode plane [107].

5.1.1 Signal Generation in the MUSIC Detector

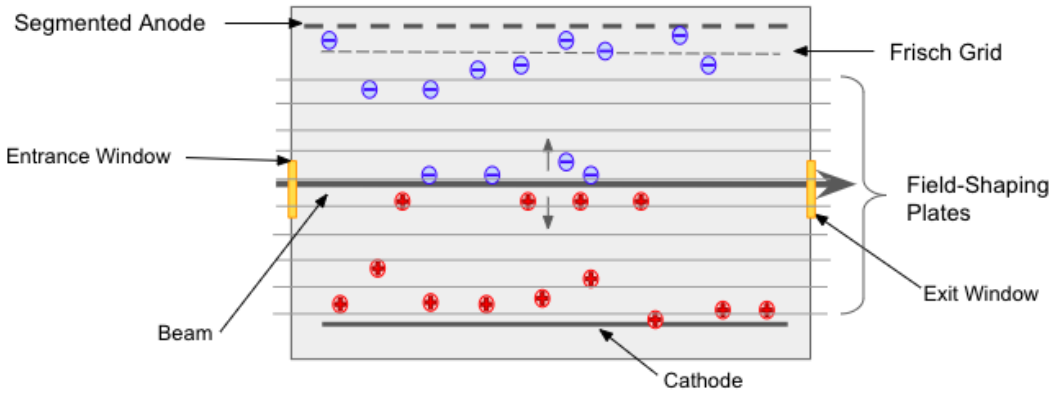

Figure 5.5: Schematic illustration of signal generation in the MUSIC detector. As the beam passes through the gas, it creates electron-ion pairs (shown as blue electrons and red positive ions). The cathode at the bottom is biased at −2.5 kV, while the segmented anode at the top is grounded. Field-shaping plates establish a uniform electric field that guides the electrons upward toward the anode strips. The Frisch grid, located between the drift region and the anode plane, shields the anodes from slowly moving positive ions, ensuring fast, uniform signal collection.

In the MUSIC detector, the general principles of gas ionisation chambers (See Section 2.7) are applied. In principle, the charged particle travels through the MUSIC detector, loses energy by ionising the gas, and creates electron–ion pairs along its path. As shown in Figure 5.5, the liberated electrons drift toward the anode while the positive ions drift toward the cathode, inducing measurable signals on the read-out electrodes. The cathode at the bottom of the detector was biased at −2.5 kV, and the anode was grounded. A uniform electric field supplied by the field-shaping plates guides the liberated electrons to the detector anodes. The segmented anode captures each particle's energy-loss profile, or "trace". Typically, this trace shows a gradual increase in energy-loss as the particle slows down. When a nuclear reaction occurs, the resulting particle causes a sudden change in the energy-loss pattern. The energy-loss of each particle inside the detector is approximately proportional to the

square of the particle's charge:

$$\Delta E \propto Z^2 \tag{5.1}$$

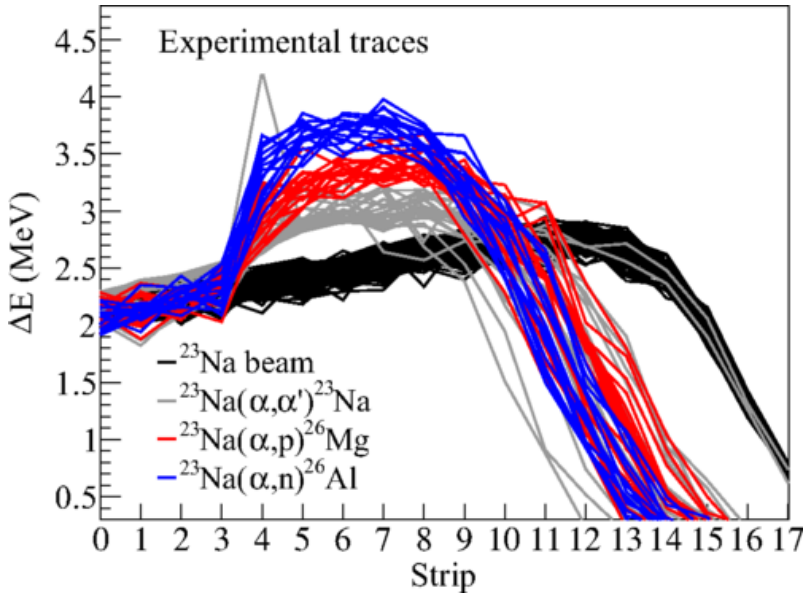

Figure 5.6: Example of experimental traces detected at strip 3 from a previous MUSIC measurement [108]. Each reaction channel producing a distinct trace: ^{23}Na(α,α')^{23}Na (grey), ^{23}Na(α,p)^{26}Mg (red), and ^{23}Na(α,n)^{26}Al (blue). Traces corresponding to the unreacted ^{23}Na beam are shown in black. The horizontal axis shows the anode strip number, while the vertical axis shows the measured energy-loss ΔE in units of MeV.

Depending on the charge of the produced particle, the change in energy-loss appears as a characteristic "dip" or "spike" in the energy-loss trace, relative to the beam's energy-loss.

Figure 5.6 shows representative examples of energy-loss traces recorded in the MUSIC detector, taken from a previous experiment investigating the ^{23}Na(α,p)^{26}Mg and ^{23}Na(α,n)^{26}Al reactions [108]. These traces illustrate the characteristic detector response and demonstrate how reaction events are identified through a sudden deviation from the beam energy-loss pattern. In this example, clear jumps are observed in strip 3, where the formation of new reaction products leads to a distinct change in the detected energy-loss behaviour. Each reaction channel produces a unique trace that differs from the unreacted beam, enabling event classification. Since each

anode strip in the detector corresponds to a specific beam energy (will be detailed in Section 5.2.5), the location of a "dip" or "spike" helps to determine the reaction energy. Hence, the MUSIC detector can measure nuclear reaction cross-sections across a range of energies using a single beam energy, offering an advantage over traditional methods that require multiple measurements at different beam energies.

5.2 Detector preparation and Calibration

5.2.1 Simulation for Experimental Optimisation and Detector Response

Simulations of the MUSIC detector response were performed before the experiment with the primary aim of optimising the experimental setup. These simulations were used to determine appropriate beam energies and gas pressures, ensuring that the Bragg peak of the primary beam was within the detector's active region and that different reaction products could be clearly distinguished by their energy-loss behaviour. The simulated energy-loss traces, shown in Figure 5.7, illustrate the expected separation between the unreacted ^{16}O beam particles (black), (p, α) reaction products (green), and $(\mathrm{p}, \mathrm{p}')$ elastically scattered particles (red). In addition, simulated ΔE–ΔE histograms were used to confirm that the (p, α) channel (green) could be isolated from competing reaction channels under the chosen experimental conditions.

It is important to emphasise that these simulations were not used for event-by-event comparison with the experimental data, nor employed to reproduce measured cross-sections or event yields. As is standard in MUSIC analyses, the simulations serve solely as a tool for detector response validation and experimental optimisation.

The measured cross-sections are obtained directly from experimental data using the MUSIC detector.

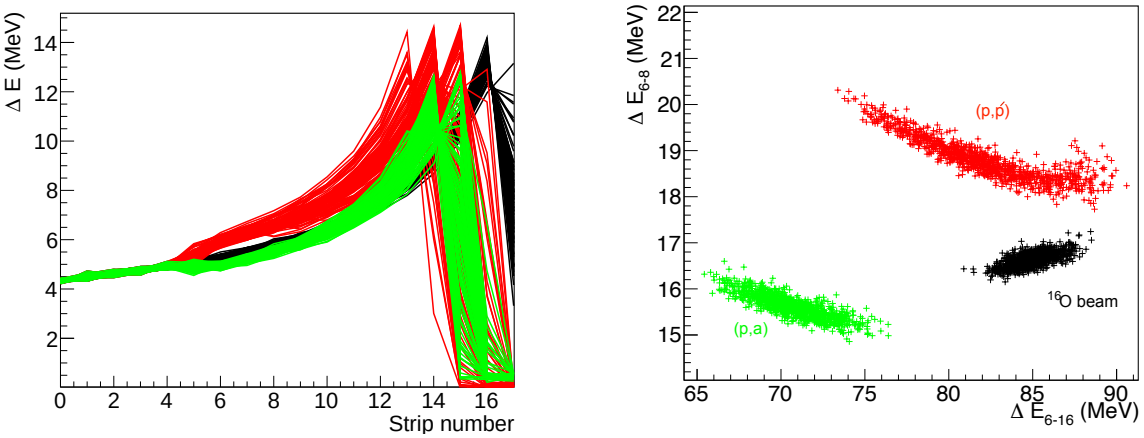

(a) (b)

Figure 5.7: Detector response simulation of energy-losses in strip 4 of the MUSIC detector, showing the expected energy-loss behaviour of different reaction products under the chosen experimental conditions. The simulated events correspond to unreacted ^{16}O beam particles (black), elastically scattered $(\mathrm{p}, \mathrm{p}')$ events (red), and (p, α) reaction products (green). (a) Simulated energy-loss traces demonstrating the qualitative differences in stopping behaviour and the location of the Bragg peak for each channel. (b) Corresponding simulated ΔE–ΔE distribution, used to assess the feasibility of separating the reaction channels based on their energy-loss characteristics.

5.2.2 Beam production and properties

A stable ^{16}O beam was provided by the ATLAS accelerator facility at ANL [104] for the experiment. The beam energy was measured using the ATLAS Time-of-Flight (ToF) system. The measured energy was 136.27 ± 0.54 MeV. The beam was tuned to a charge state of 5^+. Only a single charge state was transported to the experimental area. The beam was considered fully stripped for energy-loss calculations and simulations. This approximation, widely employed in MUSIC experiments, offers a practical balance between simplicity and accuracy for energy-loss calculations in the

MUSIC analysis methodology.

5.2.3 Gas Pressure Calibration of the MUSIC Detector

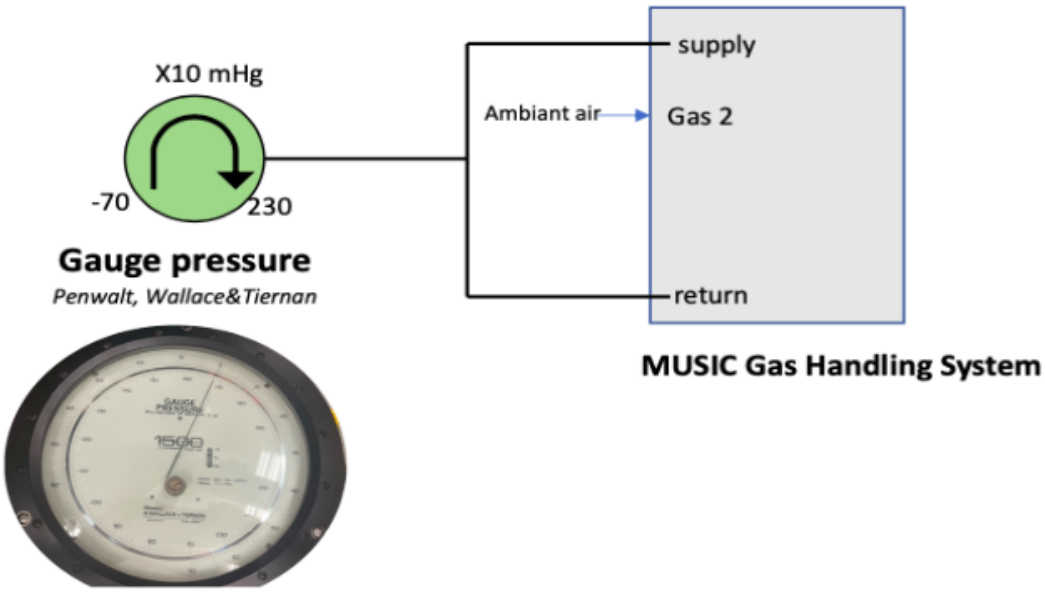

Figure 5.8: Reference pressure gauge (Penwalt, Wallace & Tiernan) and schematic of its connection to the MUSIC gas-handling system used for pressure calibration. The gauge was coupled directly to the gas return line, enabling an independent measurement of the detector gas pressure for calibration of the MUSIC pressure.

The MUSIC Gas Handling System was calibrated using an independent reference gauge of Penwalt, Wallace & Tiernan gauge pressure meter (Figure 5.8). The gauge has an operating range from -70 to 230 mmHg; the displayed values were scaled by a factor of ten. Throughout this work, pressures measured in mmHg were directly converted to Torr (1 Torr $\approx$ 1 mmHg). The pressures reported by the MUSIC internal pressure system were compared with those measured by the reference gauge over the range of 0-710 Torr. Figure 5.9 shows the correlation between the two measurements. A clear linear relationship is seen and was parameterised by the fit:

$$y = 1.0062\,x + 2.4618, \tag{5.2}$$

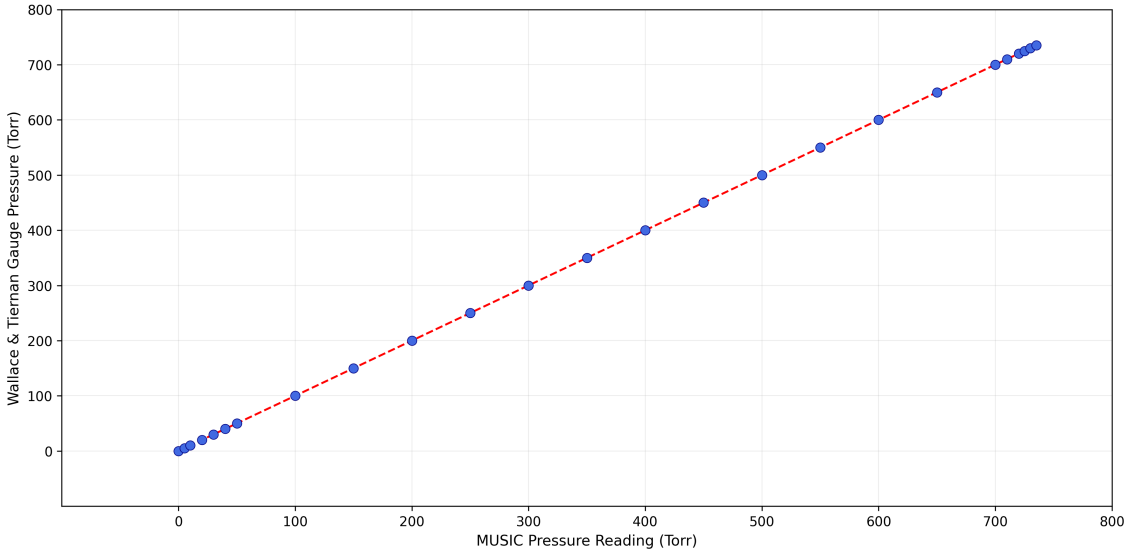

Figure 5.9: Correlation between the pressure measured by the MUSIC gas-handling system and that measured using an independent reference gauge over the range 0–710 Torr. The horizontal axis shows the MUSIC pressure readout (Torr), while the vertical axis shows the reference gauge pressure (Torr). The red dashed line represents a linear fit to the data, showing the excellent agreement between the two measurements.

Where y is the pressure measured by the reference gauge and x is the pressure reported by the MUSIC system. The coefficient of determination ($R^2 = 0.99998$) indicates excellent agreement between the two measurements. The uncertainty associated with the pressure calibration was about (0.1%-0.3%) and was propagated into the uncertainty of the target thickness and centre of mass determination, as will be discussed in Section 5.2.6.

5.2.4 Energy Calibration of the Silicon Detector

Calibration runs were performed to determine the energy response of the silicon (Si) detector. The calibration was performed using two different beams. First, the ^{228}Th α-particle source was employed to establish reference calibration points. Second, the ^{16}O beam runs were carried out at several beam energies. All measurements were conducted under vacuum conditions, with no gas in the MUSIC chamber and

no entrance or exit windows in place, ensuring that the Si detector recorded the full beam energy without additional energy-loss corrections.

For the ^{16}O beam calibration, three runs were performed with beam energies of 136.27(54) MeV, 125.13(29) MeV, and 100.1(1) MeV. The beam energies for these runs were determined independently using the ATLAS Time-of-Flight (ToF) system. For each run, the energy spectrum recorded by the Si detector was fitted with a Gaussian function, and the centroid position in ADC channels was extracted. The centroid positions obtained from both the α-source and the ^{16}O runs were correlated with their corresponding beam energies to establish the energy calibration of the Si detector. Figure 5.10 shows the correlation between the Si detector response and particles energy over the investigated range, which is well described by a linear relationship of:

$$y = 0.026\,x - 2.13, \tag{5.3}$$

Where y is the beam energy E in MeV as determined by the ATLAS ToF system and x is the Si detector signal in ADC channels. The coefficient of determination ($R^2 = 0.99974$) demonstrates the excellent linearity of the Si detector response over the investigated energy range of both sources. Although the Si detector was not employed during the cross-section measurements, its calibration provided an independent verification of subsequent energy-loss studies, including comparisons with energy-loss tables calculations and centre of mass energy determination.

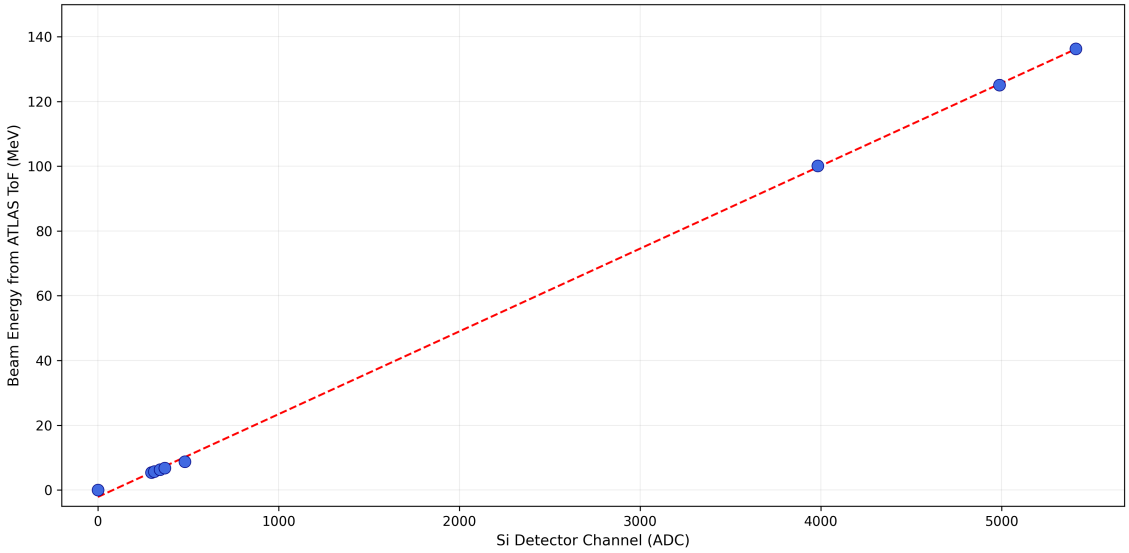

Figure 5.10: Energy calibration of the silicon detector used in experimental setup. The horizontal axis shows the silicon detector response in ADC channels, obtained from α-source measurements and the ^{16}O calibration runs, while the vertical axis shows the corresponding beam energy independently determined using the ATLAS time-of-flight (ToF) system. The solid line represents a linear fit to the data.

5.2.5 Stopping Power calibration of the Beam

In MUSIC experiments, validating the stopping-power tables is essential because the beam energy at each anode strip in the MUSIC detector is determined from calculated energy-losses rather than direct measurements (see Figure 5.11). To perform this validation, in-beam measurements were carried out to check the accuracy of stopping-power calculations describing the energy-loss of the ^{16}O beam as it traverses the entrance and exit titanium (Ti) windows (1.3 mg/cm^2) and the methane (CH_4) gas at different pressures.

A fixed ^{16}O beam energy of 135.48(15) MeV was used for all validation runs. First, a reference run was performed with the entrance and exit Ti windows in place and no gas in the detector volume. This configuration isolates energy-loss in the Ti windows. The residual beam energy after transmission through the windows was measured using the silicon detector calibrated in the previous section (Section 5.2.4).

Subsequently, a series of runs was carried out with the same Ti windows and with CH_4 gas introduced into the detector volume at five different pressures. For each pressure setting, the beam energy deposited in the Si detector was recorded, allowing the incremental energy-loss in the gas to be measured as a function of gas pressure.

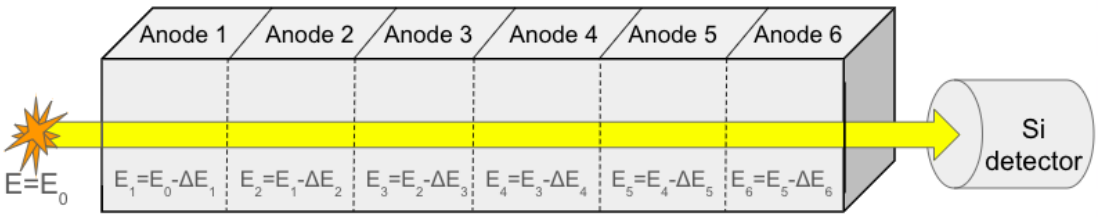

Figure 5.11: Schematic representation of the MUSIC detector, illustrating the progressive energy-loss of the beam along the detector length. As the beam traverses the active gas volume, its energy decreases from E_0 at the detector entrance to $E_i = E_0 - \sum_{k=1}^{i} \Delta E_k$ after the i-th anode strip. The residual beam energy is measured using a downstream silicon detector. For clarity, the number of anodes shown is reduced and does not represent the full segmentation of the MUSIC detector.

Table 5.1 summarises the measured beam centroids in the Si detector and the corresponding beam energies after transmission through the Ti windows and CH_4 gas for the different pressure settings. The observed decrease in beam energy with increasing gas pressure reflects the increasing energy-loss in the methane target.

Table 5.1: Residual ^{16}O beam energies measured in the silicon detector after transmission through the CH_4 gas target at different methane pressures in the MUSIC detector.

Gas Pressure (Torr)	Beam Centroid in Si (Channel)	Energy in Si (MeV)
2.46(0.44)	5193	130.81(1.25)
203.71(0.63)	4084	102.42(1.08)
404.95(0.82)	2553	63.21(0.84)
555.88(0.97)	1202	28.64(0.63)
606.19(1.02)	528	11.38(0.52)
621.29(1.03)	259	4.49(0.48)

The measured energy-losses were compared with theoretical predictions obtained from stopping-power calculations using the SRIM [56] and ATIMA [109] tables. Figures 5.12 and 5.13 compare energy-loss calculations based on SRIM and ATIMA stopping power tables, respectively. While both calculations reproduce the general trend, ATIMA provides better overall agreement with the measured energy-losses. In contrast, SRIM exhibits deviations of up to approximately 10%, particularly at lower residual beam energies. Based on this comparison, ATIMA stopping-power tables were adopted for all subsequent energy-loss calculations in the MUSIC analysis, including the determination of beam energies inside the detector volume. The remaining differences between measured and calculated energy also contributed to the uncertainty on the target width, as will be discussed in Section 5.2.6.

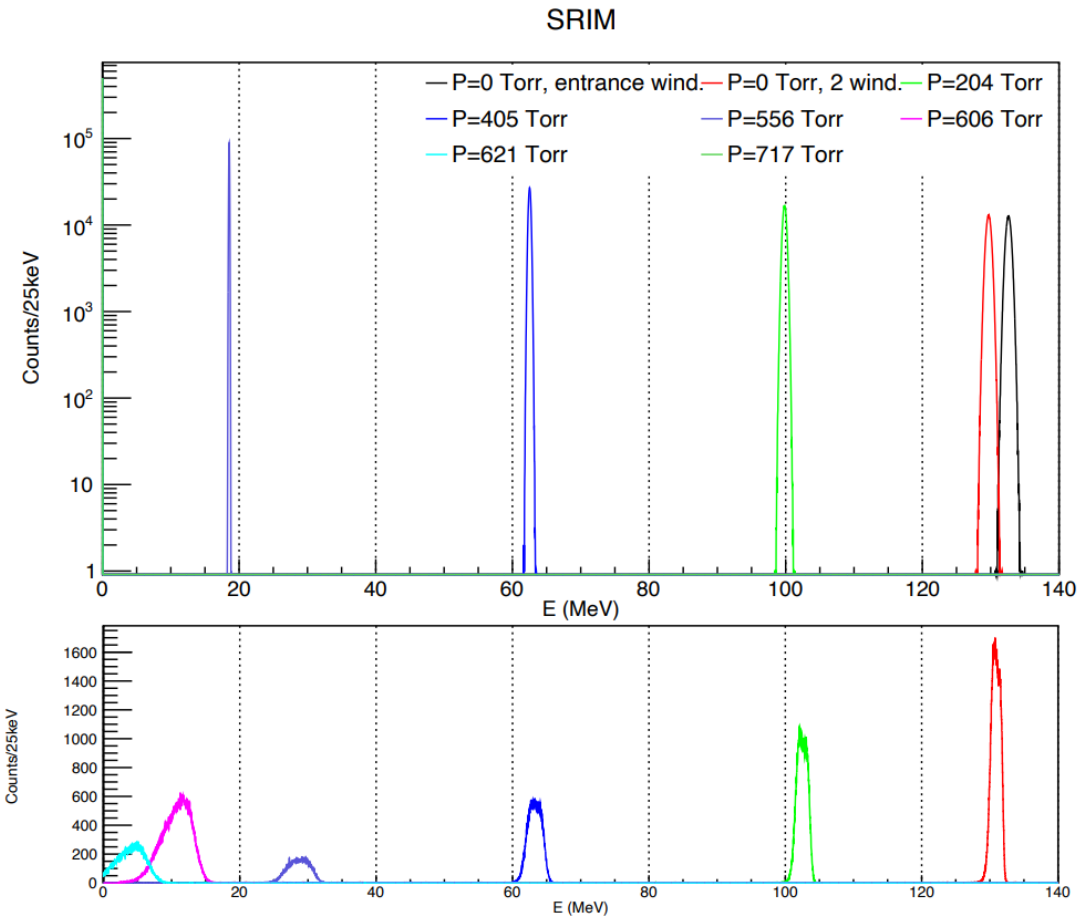

Figure 5.12: Comparison between experimentally measured beam energies and SRIM stopping-power calculations for different gas pressures and window configurations. The lower panel shows the energy spectra measured by the downstream silicon detector. The upper panel shows the corresponding beam energies calculated using SRIM stopping-power tables. At high energies, excellent agreement is observed between the experimental measurements and SRIM predictions. At lower energies, systematic deviations appear, with SRIM predicting slightly lower residual energies at $P = 556$ Torr and failing to accurately reproduce the lowest-energy spectra at $P = 606$ and 621 Torr.

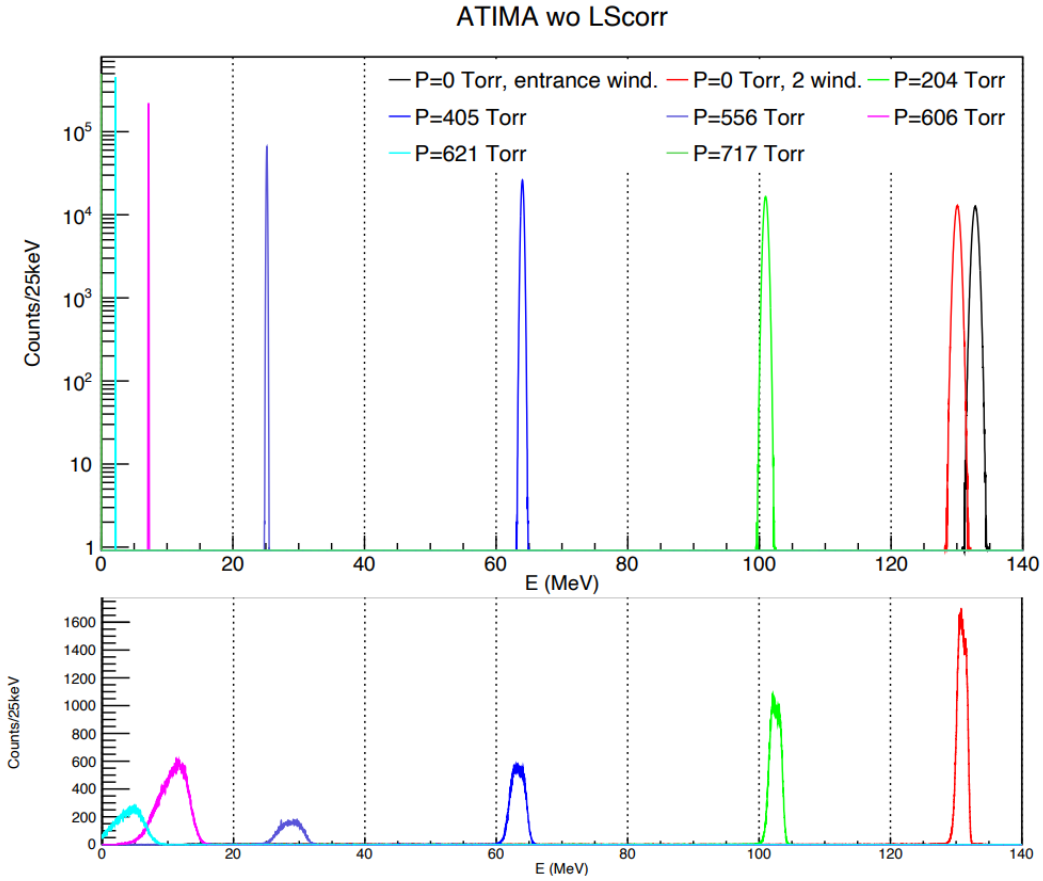

Figure 5.13: Comparison between experimentally measured beam energies and ATIMA stopping-power calculations for different gas pressures and window configurations. The lower panel shows the energy spectra measured by the downstream silicon detector, while the upper panel shows the corresponding beam energies calculated using ATIMA stopping-power tables. In contrast to SRIM-based calculations, ATIMA provides significantly better agreement with experimental data at low energies, accurately reproducing both peak positions and spectral shapes across the full investigated pressure range.

5.2.6 Determination of the Centre-of-Mass Energy

Following the validation of the stopping-power calculations, the centre-of-mass energy (E_{cm}) for the $^{16}\mathrm{O}(\mathrm{p},\alpha)^{13}\mathrm{N}$ reaction was determined for each anode strip of the MUSIC detector using Monte Carlo simulations. Because the beam continuously loses energy as it traverses the gas target, reactions occurring at different positions within the detector correspond to different centre-of-mass energies. As a result, each anode strip samples a range of energies rather than a single, well-defined value. The Monte Carlo simulations modelled the transport of the $^{16}\mathrm{O}$ beam through the entrance titanium (Ti) window, the methane (CH_4) gas, and the exit Ti window using ATIMA stopping-power tables, which were validated in the previous section (Section 5.2.5). The initial beam energy was taken as 135.48(15) MeV, as determined independently by the ATLAS Time-of-Flight (ToF) system. The methane gas pressure was fixed at 716.88 Torr, corresponding to the operating conditions of the experiment, with the pressure converted to density based on the calibrated gas handling system.

The simulations included the actual shape of the MUSIC detector, especially the division of the anode plane into strips 15.8 mm wide along the beam direction. Since nuclear reactions may occur at any position within a given strip, the reaction vertex was sampled uniformly along the strip width. For each sampled position, the beam energy at that depth was calculated by propagating the energy-loss through the gas, and the corresponding centre-of-mass energy was then determined from the reaction kinematics. This procedure accounts for the finite strip width and its contribution to the uncertainty in the centre-of-mass energy. For each anode strip, the resulting distribution of centre-of-mass energies was used to define the centre of mass energy, $\langle E_{\mathrm{cm}} \rangle$, taken as the mean of the distribution. The dominant contribution to ΔE_{cm} arises from the finite width of the anode strip. Additional contributions from the

uncertainty in the incident beam energy and from the gas-density determination were also included in the simulations, but are subdominant compared to the geometric effect of the strip width.

Table 5.2: Centre-of-mass energies (E_{cm}) and corresponding uncertainties for each detector strip, derived from Monte Carlo simulations.

Strip	E_{cm} **(MeV)**	ΔE_{cm} **(MeV)**
2	6.91	0.13
3	6.64	0.14
4	6.36	0.14
5	6.07	0.15
6	5.79	0.15
7	5.47	0.16
8	5.14	0.16

The centre-of-mass energies and their corresponding uncertainties for each active anode strip are summarised in Table 5.2. These values were calculated down to the reaction threshold at $E_{\mathrm{c.m.}} = 5.218$ MeV and were subsequently used in the extraction of the reaction cross-sections.

5.3 Data Acquisition System

Signals generated in the MUSIC detector were collected and processed using a fully digital data acquisition system. As charged particles traversed the detector gas, the induced charge signals from the segmented anode strips were routed to charge-sensitive preamplifiers, which converted the collected charge into voltage pulses suitable for digitisation. The analogue signals were digitised using four CAEN V1725 waveform digitiser boards [110]. Each digitiser provides multi-channel, high-speed analogue-to-digital conversion (ADC) and performs digital pulse processing. The use of multiple digitiser boards allowed simultaneous readout of all anode strips, with events time-stamped to enable offline correlation across channels and boards. Data

acquisition, configuration, and online monitoring were managed using the CoMPASS software framework [111]. During data acquisition, key quantities, including pulse height (energy), timing information, and channel identifiers, were extracted and stored.

The acquired data were written to disk in ROOT format as a `TTree` structure, which formed the basis for the subsequent offline analysis. Each recorded event contained the following information:

- `Channel`: identifies the anode strip or detector segment producing the signal,
- `Board`: specifies the digitiser board associated with the channel,
- `Timestamp`: provides the time at which the signal was recorded,
- `Energy`: represents the digitised pulse height after digital signal processing, proportional to the energy deposited in the detector.

The overall signal formation, processing, and data acquisition chain from ionisation in the detector gas to digitisation and data storage is summarised schematically in Figure 5.14. This diagram provides an overview of the MUSIC data acquisition system and the flow of information from the detector anode strips through the preamplifiers and CAEN digitiser boards to the CoMPASS software and ROOT data output.

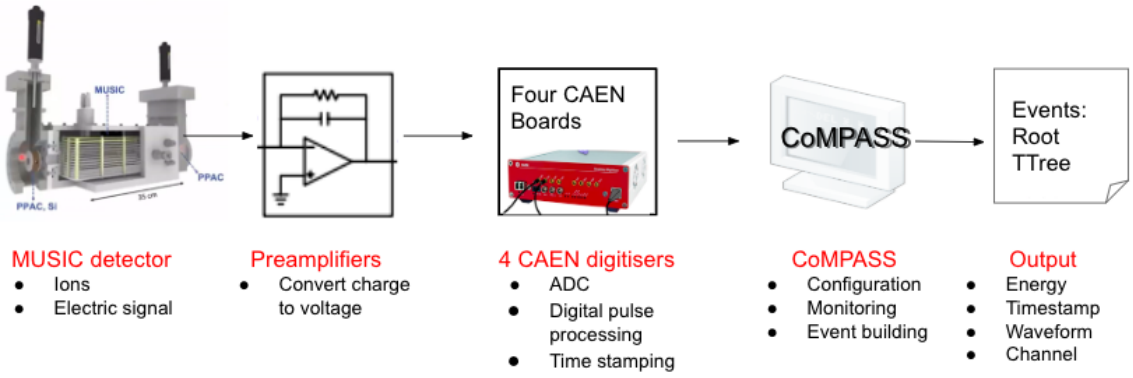

Figure 5.14: Simplified block diagram of the MUSIC data acquisition system, showing the signal-processing and data-flow chain from the detector anode strips through the charge-sensitive preamplifiers and CAEN digitisers to the CoMPASS acquisition software and ROOT-based data output.

5.4 Experimental Conditions and Data Taking

The measurement of the $^{16}\mathrm{O}(\mathrm{p},\alpha)^{13}\mathrm{N}$ reaction ($Q = -5.218$ MeV) was performed in inverse kinematics using a ^{16}O beam delivered by the ATLAS accelerator. The beam energy at the entrance of the MUSIC detector was 136.0 ± 0.15 MeV, as determined by the ATLAS Time-of-Flight system. The MUSIC detector chamber was filled with high-purity methane (CH_4) gas at a pressure of 710 Torr. The beam entered the detector through a titanium (Ti) entrance window with a thickness of 1.3 mg/cm^2, followed by a dead gas region of 35.9 mm. After traversing these materials, the beam energy at the active detector volume was reduced to approximately 124 MeV. During the experiment, the ^{16}O beam propagated through the methane gas along the full length of the detector (structure illustrated in Figures 5.1 and 5.2), undergoing continuous energy-loss before exiting through the downstream window.

For the primary production runs, the beam intensity was limited to approximately 3×10^4 particles per second to ensure stable data acquisition and minimise pileup effects. Data were collected continuously for a total beam time of approxi-

mately 27 hours. Online monitoring of detector performance and data quality was carried out using the CoMPASS data acquisition software [112]. The digitised signals were recorded by the CAEN data acquisition system and stored as raw ROOT files, which were subsequently processed in an offline pre-analysis stage before the (p, α) events analysis.

5.5 Raw Data Processing and Event Reconstruction

The conversion of the raw data, carried out by Chloé Fougères [113], involves two main steps: time synchronisation and strip gain matching.

5.5.1 Time Synchronisation

The MUSIC data were recorded using four independent digitiser boards, each with its own clock. To enable multi-board event reconstruction, constant inter-board time offsets were determined using high-rate beam channels selected with energy gates around the beam peak. The offsets were obtained by aligning characteristic time-interval patterns between the reference board (Board 3) and the other boards, and then applied as board-dependent timestamp shifts,

$$T_{\mathrm{aligned}} = T_{\mathrm{raw}} - \Delta t_{\mathrm{Board}}, \tag{5.4}$$

where

- T_{raw} is the original timestamp recorded by the digitiser for a given hit,
- Δt_{Board} is the constant time offset associated with the digitiser board on which the hit was recorded, determined relative to a chosen reference board,
- T_{aligned} is the corrected timestamp after time synchronisation, used for event building.

Figure 5.15 illustrates the timing correction procedure for Board 0 relative to the reference Board 3. The same procedure was applied independently to the remaining digitiser boards (Boards 1 and 2), yielding the same improvements in timing alignment. Figure 5.16 shows the resulting event time distributions after the full multi-board synchronisation.

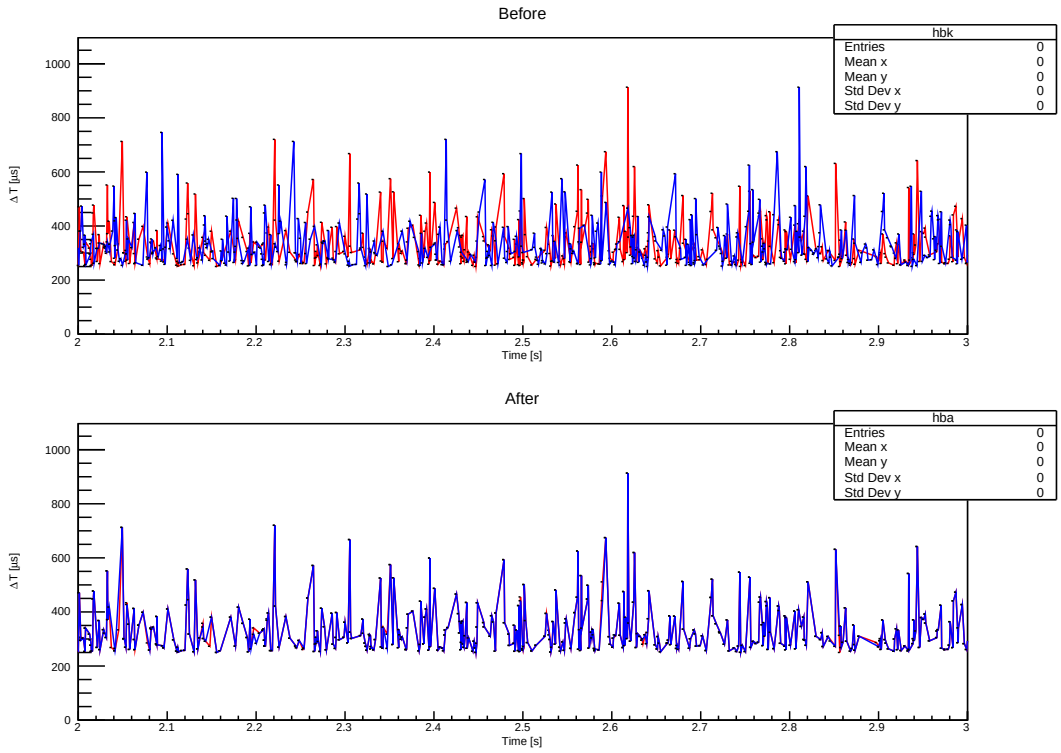

Figure 5.15: Determination of the constant timing offset for Board 0 relative to the reference Board 3. The upper panel shows the distribution of the measured time difference (ΔT) in (μS) as a function of event time (T) (S) before correction, while the lower panel shows the same distribution after applying the board-dependent timestamp shift.

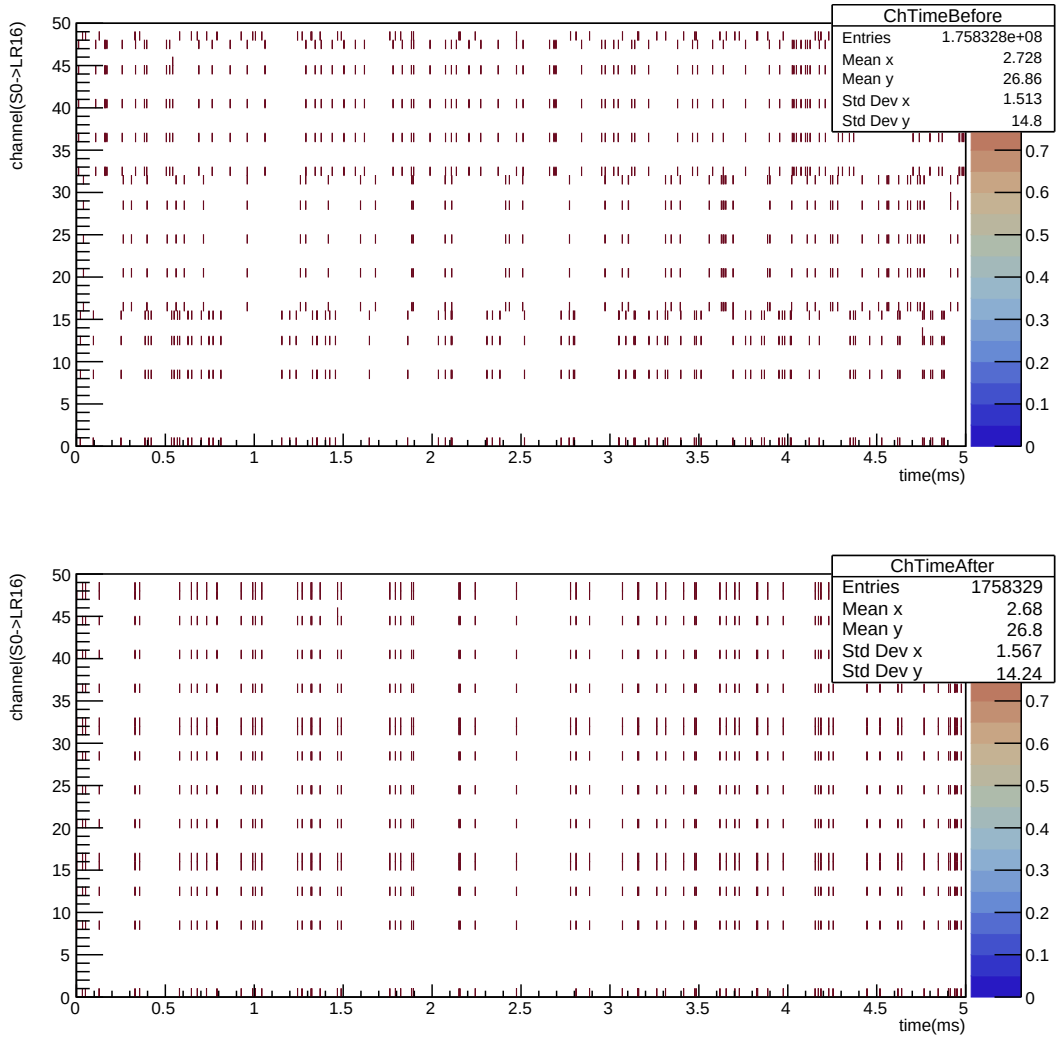

Figure 5.16: Event-level time distributions for individual detector channels before (top panel) and after (bottom panel) application of the multi-board time synchronisation corrections. The horizontal axis shows the event time, while the vertical axis indicates the detector active channels strips (0-16). After correction, the improved temporal alignment across channels demonstrates the effectiveness of the timing calibration and enables reliable multi-channel event reconstruction.

5.5.2 Strip Gain Matching

For each anode segment, the raw energy response was first histogrammed using events corresponding to the unreacted beam. The centroid of the beam peak was then determined by fitting a Gaussian function to the energy distribution. Figure 5.17 shows an example of the energy histogram and Gaussian fit for the left segments of strips 1 and 2; the same procedure was applied to all left and right segments of the 16 MUSIC strips. A strip-dependent gain-matching factor, g_i, was defined as

$$g_i = \frac{E_{\mathrm{ref}}}{\mu_i}, \tag{5.5}$$

where μ_i is the fitted centroid of the beam peak (in raw ADC units) for strip i, and $E_{\mathrm{ref}} = 6$ is an arbitrary reference value in arbitrary units (a.u.) chosen solely to normalise the response of all strips to a common relative scale. The corrected energy for each event in strip i was then calculated as

$$E_i^{\mathrm{matched}} = g_i \, E_i^{\mathrm{raw}}, \tag{5.6}$$

where E_i^{raw} denotes the unnormalised ADC signal recorded by the digitiser. This procedure equalises the electronic gain between strips, allowing energy-loss patterns to be compared consistently across the detector. After applying the gain-matching correction, energy-versus-strip maps were used to verify that the beam peak aligned uniformly across all anode segments at 6 (a.u) (Figs. 5.18 and 5.19), yielding a typical energy resolution of approximately 6–7% (FWHM).

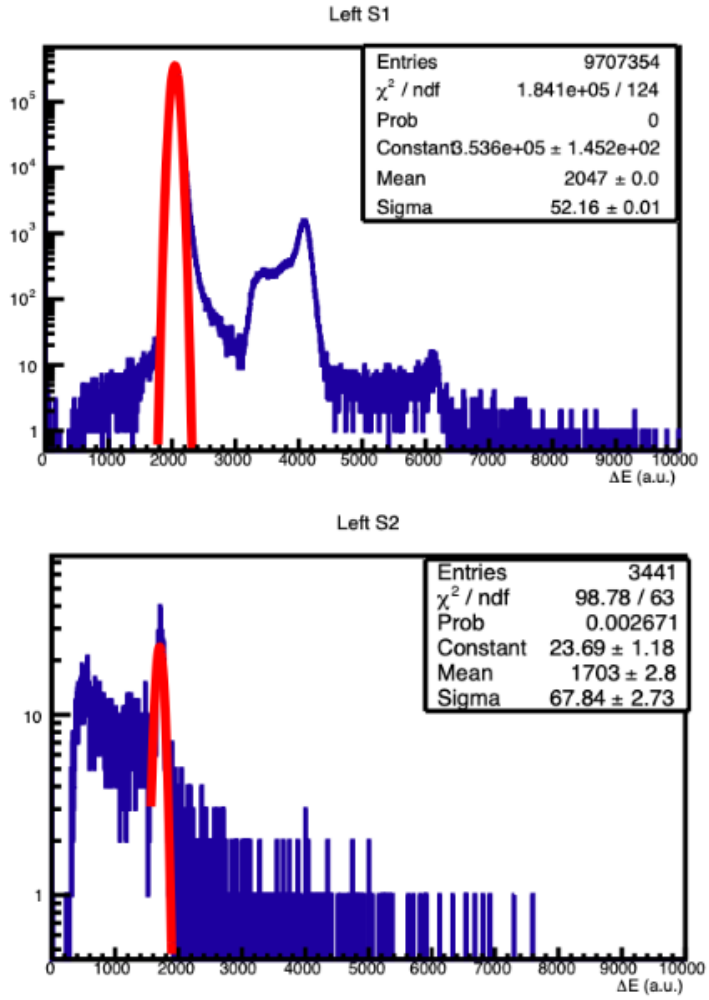

Figure 5.17: Gaussian fits were used on the energy-loss spectra of the beam in the left segments of strips 1 and 2 of the MUSIC detector to determine the centroid positions of the beam peak. Due to the asymmetric segmentation of the anodes, the majority of the beam charge is collected by the longer segments (e.g., strip 1L), leading to lower statistics in the shorter segments (e.g., strip 2L). The same fitting procedure was systematically applied to both the left and right segments of all 16 anodes.

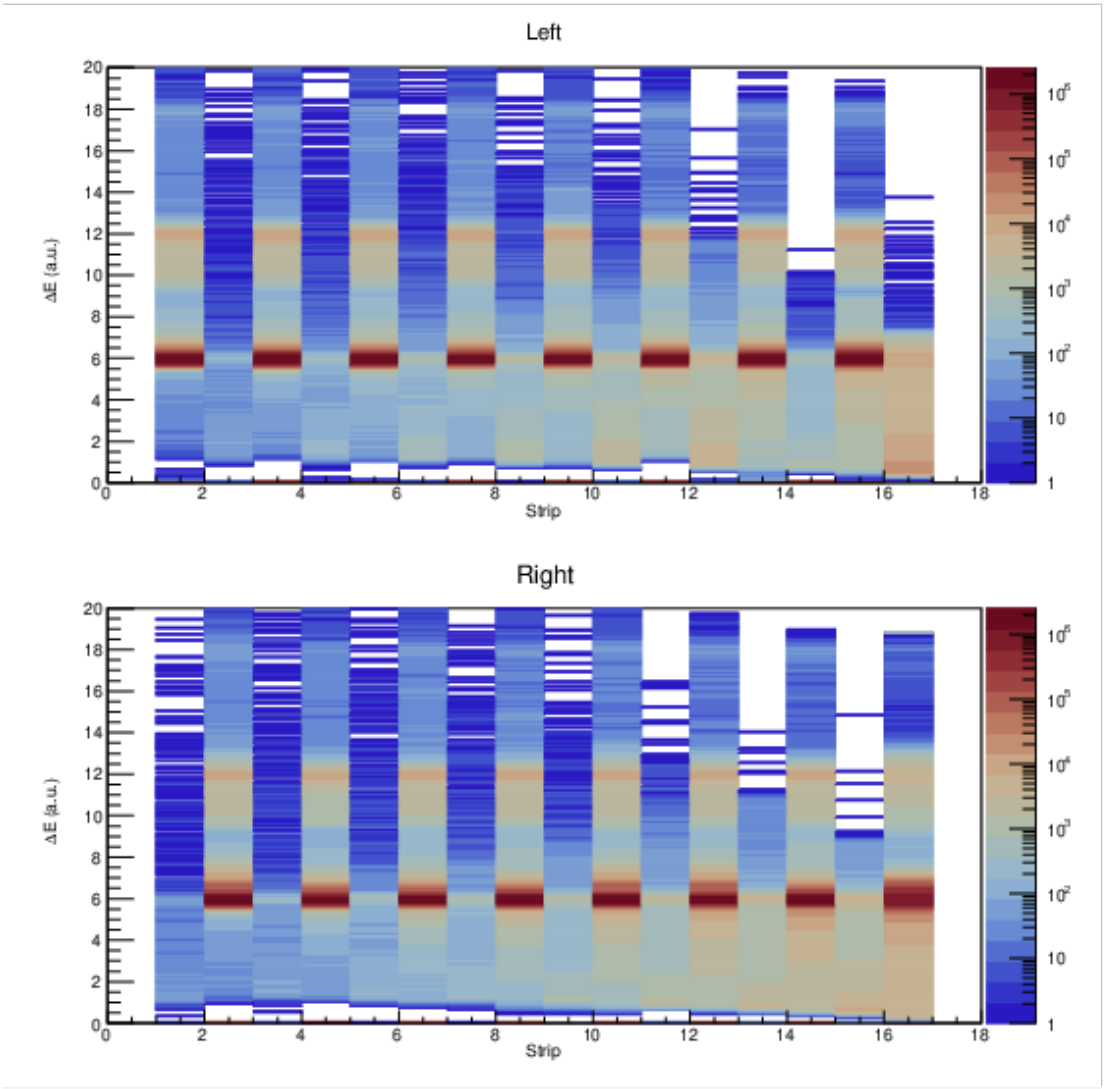

Figure 5.18: Strip-by-strip energy-loss distributions for the left (upper panel) and right (lower panel) anode segments of the 16 active strips of the MUSIC detector after gain matching. Each segment was rescaled such that the centroid of the unreacted beam peak is aligned at $E_{\text{loss}} = 6$ a.u., ensuring a uniform detector response across all channels.

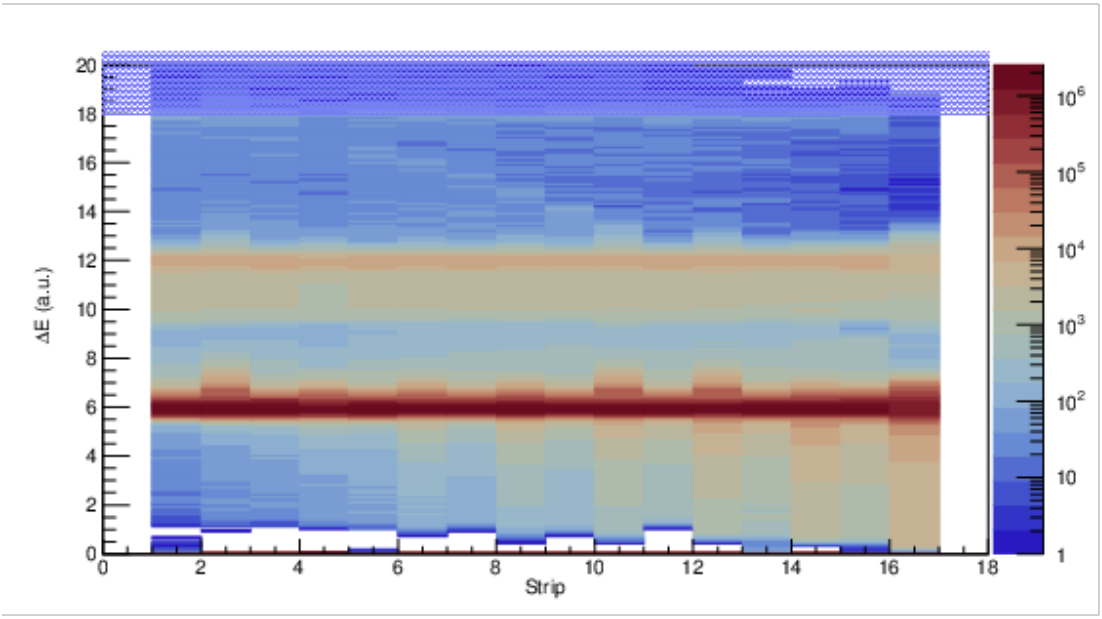

Figure 5.19: Combined left and right anode segment energy-loss distributions for all 16 active strips of the MUSIC detector after gain matching and normalisation. The summed distributions demonstrate uniform alignment of the unreacted beam peak at $E_{\text{loss}} = 6$ a.u. across all strips.

5.5.3 Event Building

After time synchronisation and strip gain matching, events were formed by grouping consecutive hits within a fixed coincidence window of 5 μs, defined relative to the start time of the current event. Each hit was mapped to a detector element (left/right strip segment, S0, S17, cathode, and grid).

To suppress time pileup and ambiguous channel assignments, events were rejected if more than one hit was recorded in the same detector element within the coincidence window. Accepted events were written to an event-level ROOT tree used for subsequent (p, α) reaction analysis.

5.6 Overview of (p, α) Event Identification

Following the raw data processing and event reconstruction described in Section 5.5, the MUSIC dataset was prepared for the classification of (p, α) reaction events. At this stage, all detector channels were time-synchronised and gain matched to a common reference of 6 a.u., enabling consistent comparison of the energy-loss (E_{loss}) signals from different particles.

The (p, α) event-identification procedure began by applying a gate on the first active strip (strip 1) to select particles corresponding to beam ions entering the detector gas volume. This removed events that could be associated with interactions in the entrance window or with particles scattered before reaching the active region. A multiplicity condition was then applied to suppress events involving large-angle scattering. In addition, a continuity requirement was imposed to ensure that valid events produced a continuous energy-loss trace across successive strips, as expected for particles traversing the detector along the beam axis.

Although each anode strip in MUSIC is electrically isolated and triggered independently, limited charge sharing between neighbouring anode strips can occur due to transverse diffusion of the ionisation electrons during their drift toward the anode plane. Since event identification relies on continuity requirements and summed energy-loss information across multiple consecutive strips, the total collected charge is conserved. Consequently, charge sharing does not affect the classification of reaction events or the extracted yields.

After these selections, the energy-loss patterns of the remaining events were examined. Nuclear reactions leading to ^{13}N production are characterised by a sudden decrease in E_{loss} (a dip) relative to the unreacted ^{16}O beam. To guide the identification of this feature, approximate expectations for the energy-loss separation between

the beam and ^{13}N particles were obtained using `LISE++` calculations with ATIMA stopping powers.

To evaluate the robustness of the event selection, all the gating conditions (Detailed in the following sections) were systematically varied from loose to strict, and the resulting (p, α) yields were compared. The mean yield obtained over this range of selections was adopted as the nominal result, while the observed spread was taken as an estimate of the systematic uncertainty associated with the event-identification procedure.

5.6.1 Strip 1 Energy Deposition: Beam-Related Events

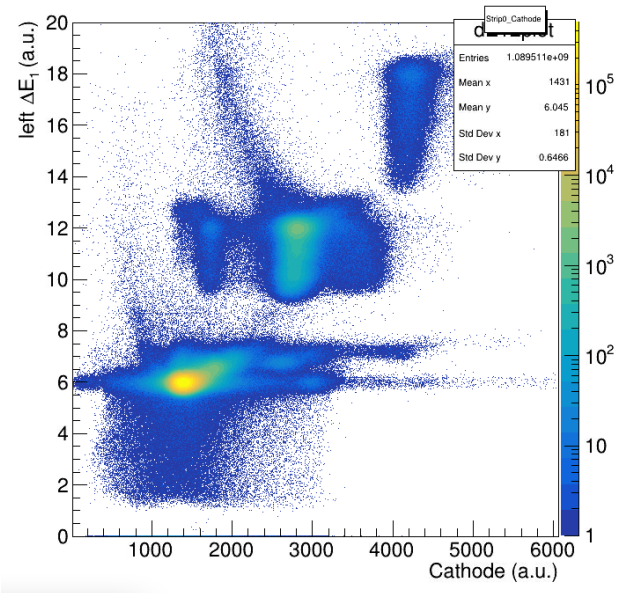

Figure 5.20: Two-dimensional ΔE–ΔE correlation histogram. The vertical axis shows the energy-loss of strip 1 (a.u.), while the horizontal axis shows the corresponding cathode energy deposition (a.u.). The dominant locus at $E_{\text{loss}} \approx 6$ a.u. corresponds to the unreacted beam. Additional clusters at higher energy-loss values, around 12 and 18 a.u., are primarily attributed to pileup events.

After gain matching, the energy-loss distributions in all strips were normalised such that the unreacted ^{16}O beam peak appeared at $E_{\text{loss}} = 6$ a.u. (see Section 5.5.2).

The correlation between the energy deposited in the first active strip (strip 1) and the cathode signal is shown in Figure 5.20. A dominant cluster centred at 6 a.u. corresponds to beam ions entering the active gas volume, while a smaller population at higher energy-loss ($\sim$ 12 and 18 a.u.) arises from pileup events at strip 1.

To define a clean sample of beam-related events entering the detector, a gate was applied to the energy-loss distribution of strip 1. An initial wide gate of $6 \pm 5\sigma$ around the beam peak was used to include the full beam population. However, this broad selection was found to complicate the reliable separation of reaction channels due to increased unwanted background events. The gate was therefore progressively tightened to $6 \pm 2\sigma$, which significantly improved event separation while retaining the majority of true beam events.

The impact of the strip 1 gate is illustrated in Figs. 5.21, 5.22, and 5.23, which show the corresponding two-dimensional ΔE–ΔE distributions for events occurring in strip 2 for three gating conditions: no gate, wide gate of $(6 \pm 5\sigma)$, and narrower gate of $(6 \pm 2\sigma)$, respectively. Upon application of the initial gate around the beam peak, several unwanted clusters are removed, including the prominent feature at approximately 12 a.u., which is primarily attributed to pile-up events originating in strip 1, as was demonstrated in Figure 5.20. Subsequent tightening of the gate to $6 \pm 2\sigma$ further enhances the separation between the (p, α) reaction locus and the unreacted beam, leading to a cleaner discrimination of reaction events.

However, some clusters remain visible even after tightening the gate to $\pm 2\sigma$. The persistence of these features indicates that they are not solely associated with beam-related pile-up and therefore require further selection criteria to be removed.

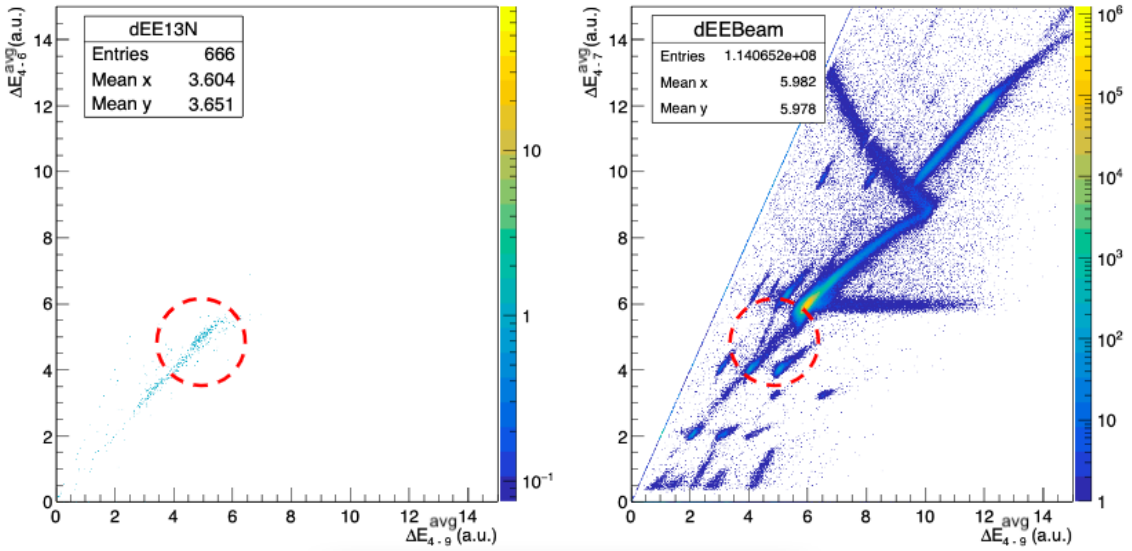

Figure 5.21: Two-dimensional energy-loss (ΔE) distributions for events associated with strip 2 of the MUSIC detector before applying any gating conditions. Left panel: events with energy-loss lower than the unreacted beam, corresponding to the region where candidate (p, α) reactions are expected (indicated by the red dashed circle). Right panel: the full event distribution, dominated by the unreacted beam. For both panels, the horizontal axis shows the average energy-loss deposited in strips 4–9, while the vertical axis shows the average energy-loss deposited in strips 4–7. In the absence of gating, multiple clusters are visible, including a prominent high-energy-loss structure around 12 a.u. in the full event distribution.

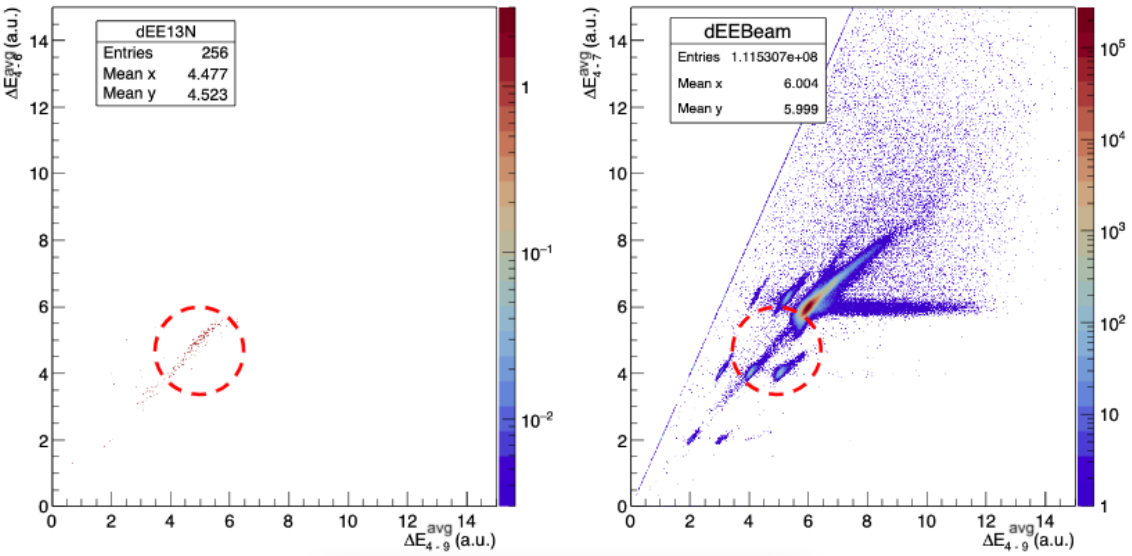

Figure 5.22: Same as Figure 5.21, but after applying a $\pm 5\sigma$ gate on the strip 1 energy-loss distribution. Several spurious clusters visible in the ungated case are excluded; however, additional structures remain, indicating that further event-selection criteria are required.

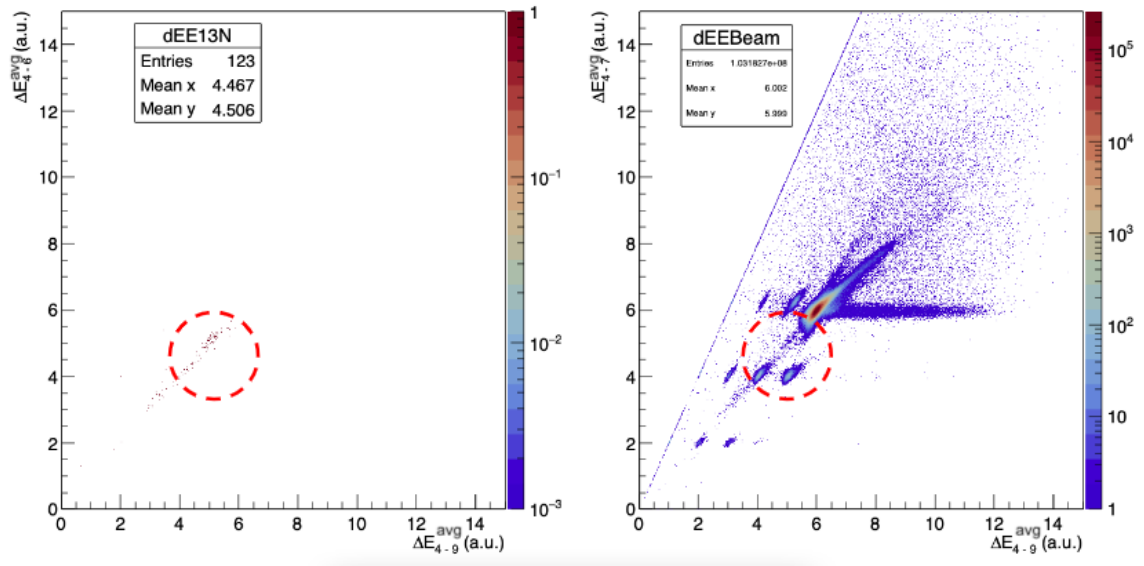

Figure 5.23: Same as Figure 5.22, but after applying a $\pm 2\sigma$ gate on the strip 1 energy-loss distribution. This tighter gate further suppresses residual structures, leading to clearer separation of candidate (p, α) events from the unreacted beam.

5.6.2 Multiplicity and Continuity Conditions

As explained in Section 5.1, the segmentation of the MUSIC detector enables the application of selection criteria to filter events. Two such criteria were applied: a multiplicity condition and a continuity condition. Together, these conditions remove events associated with large-angle scattering, pileup, and incomplete charge collection.

Multiplicity condition: The multiplicity condition exploits the fact that each anode strip in the MUSIC detector is segmented into left and right readout channels. For particles travelling close to the beam axis, the ionisation charge is expected to be collected predominantly by a single (the long) segment in each strip. To implement this selection, a multiplicity parameter was defined for each of the first eight anode strips as

$$\mathrm{mult}(a) = S^{\mathrm{L}}(a) \times S^{\mathrm{R}}(a), \tag{5.7}$$

where $S^{\mathrm{L}}(a)$ and $S^{\mathrm{R}}(a)$ denote the energy-loss amplitude recorded in the left and right segments of strip a, respectively. Events satisfying $\mathrm{mult}(a) = 0$ correspond to signal deposition in only one segment and were kept, while events with non-zero multiplicity were rejected. This multiplicity condition was required to be satisfied consistently across multiple consecutive strips, typically strips 1–8. Under the present experimental conditions, kinematic calculations performed using `CATKIN` [114] confirm that reaction products of interest are not emitted at large laboratory angles. The application of this selection removed approximately 6% of the total events, consistent with expectations, and therefore does not affect genuine (p, α) events (as seen in Figure 5.24).

Despite the application of the multiplicity condition, a small number of residual clusters remain visible in the data, indicating that these features arise from sources other than charge sharing or large-angle scattering and require additional selection criteria.

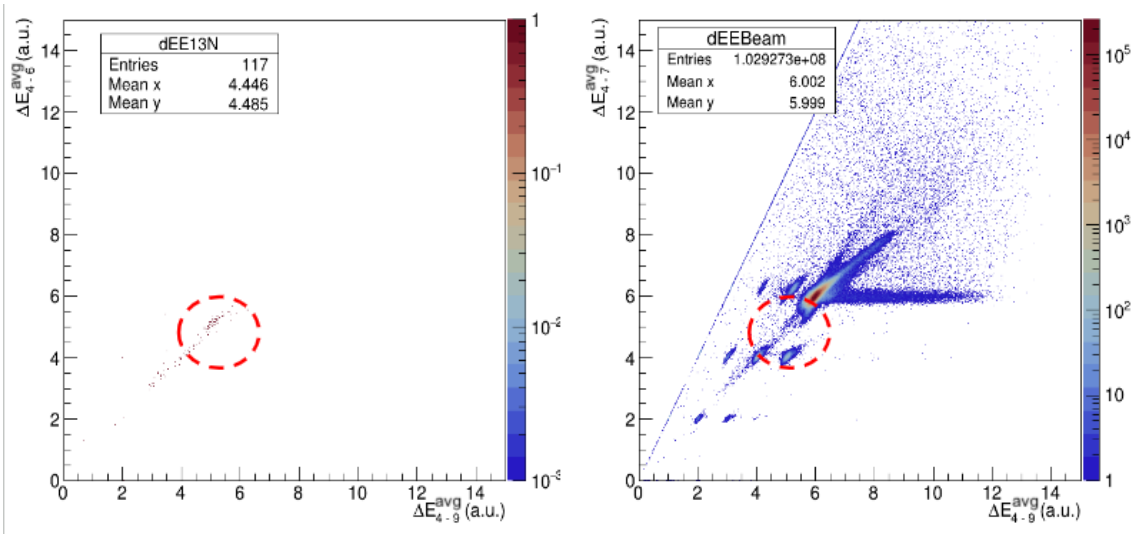

Figure 5.24: Same as figure 5.23, but after adding the multiplicity condition. The left panel shows the region containing candidate (p, α) events (indicated by the red dashed circle), while the right panel shows the full event distribution dominated by the unreacted beam.

Continuity condition: As a charged particle traverses the detector gas, it is expected to deposit energy continuously across several consecutive anode strips before coming to rest. Based on this expectation, a continuity condition was defined, requiring that any accepted event exhibit a non-zero signal across a minimum number of consecutive anodes. To enforce this requirement, a continuity condition was implemented by requiring a non-zero signal in each strip within a specified range:

$$\prod_{a=0}^{j} \left(S^{\mathrm{L}}(a) + S^{\mathrm{R}}(a) \right) > 0, \tag{5.8}$$

where the product is taken over the relevant strip range $[0, j]$ where j spanning strips 6–12, and $S^{\mathrm{L}}(a)$ and $S^{\mathrm{R}}(a)$ denote the energy-loss amplitude recorded in the left and right segments of strip a, respectively, events failing this condition, i.e., events that appear in one strip and disappear in subsequent strips, are characteristic of electronic instabilities or readout errors and were therefore rejected. Figure 5.25 illustrates the effect of the continuity condition and the nature of the rejected events. The application of this requirement removes the clusters previously observed in the full event distributions shown in Figures. 5.21, 5.22, 5.23, and 5.24. This confirms that these structures originate from readout-related issues, where events exhibit discontinuous, unphysical changes in signal that violate the expected continuous energy-loss behaviour across multiple strips. It should be noted that, in Figure 5.25, the continuity condition was applied only to strips 0–8; since strip 9 is included in the figure but not constrained by the condition, an additional cluster remains visible.

While the continuity condition is expected to remove only a small fraction of events from each strip, with a typical overall impact of 1–2%, an unexpectedly significant reduction of approximately 35% of the total events was observed. Further investigation traced this loss to strip 3, where a subset of events disappears in that strip while remaining normal in the preceding and following strips, as shown

in Figure 5.26. This behaviour is investigated in detail, and its impact on the analysis is discussed in Section 5.11.

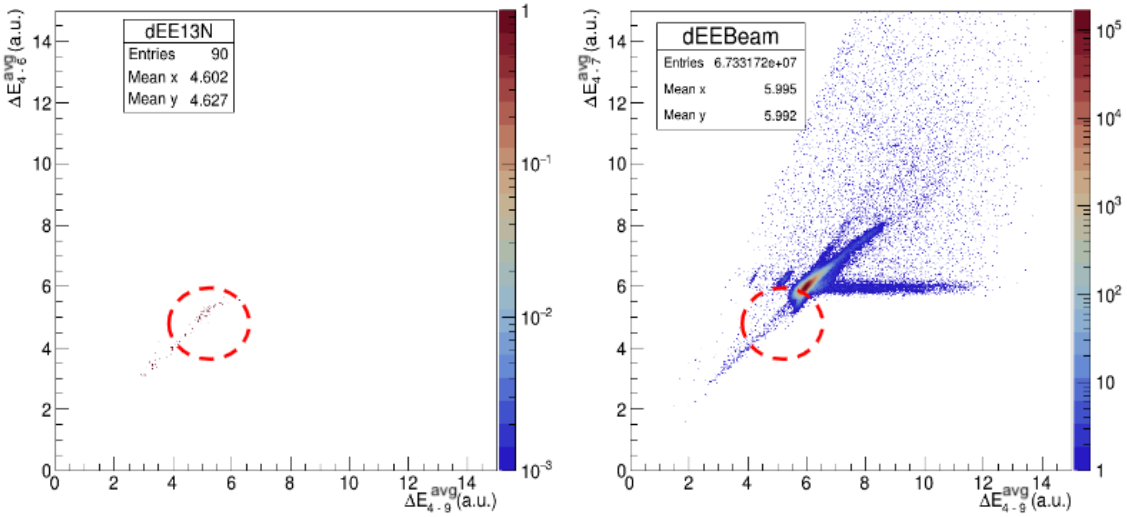

Figure 5.25: Same as the previous figures, but after applying the continuity condition requiring non-zero signals across strips 0–8. This selection removes events with discontinuous energy deposition, reducing the total event population by approximately 35% of the full event distribution (left panel). The left panel shows the region containing candidate (p, α) events (indicated by the red dashed circle), while the right panel shows the full event distribution after this filtering step.

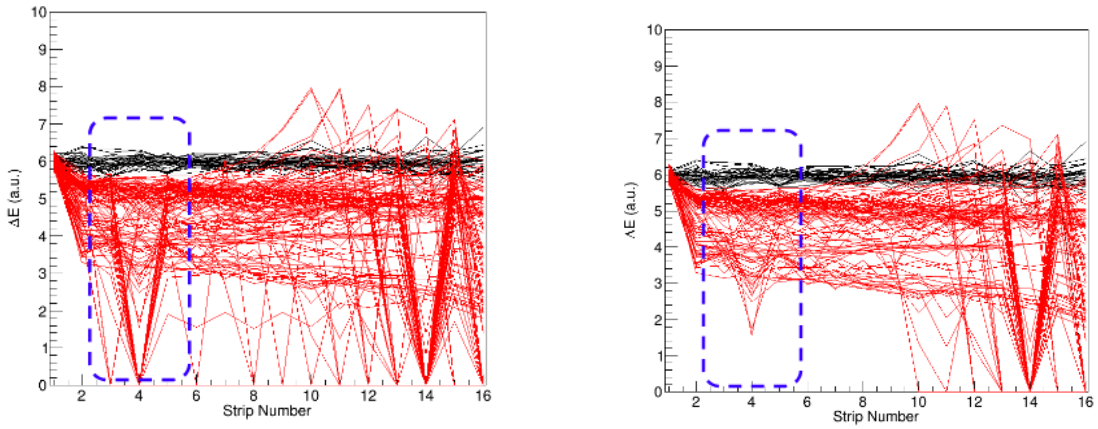

(a) Continuity condition off (b) Continuity condition on

Figure 5.26: Energy-loss traces for events assigned to Strip 2, illustrating the effect of the continuity condition and the irregular behaviour observed in Strip 3. Left panel: continuity condition disabled. Right panel: continuity condition enabled. The dashed blue rectangle highlights events that exhibit a discontinuity in Strip 3, where the signal disappears in that strip but reappears in subsequent strips. Such events violate the continuity requirement and are therefore rejected. This behaviour indicates inconsistencies in event detection associated with strip 3.

5.6.3 Energy-Loss Thresholds for (p, α) Identification

After the application of the beam gate, multiplicity, and continuity conditions, the energy-loss behaviour of the remaining events was examined. Nuclear reactions producing ^{13}N are characterised by a sudden reduction in energy-loss relative to the unreacted ^{16}O beam, appearing as a distinct dip in the ΔE traces. Since the gain-matched beam peak is normalised to $E_{\mathrm{loss}} = 6$ a.u., genuine (p, α) events are expected to populate regions below the beam peak (6 a.u.).

To estimate the expected dip position, stopping-power calculations were performed using `LISE++`. The calculated beam energy-loss was used to determine a scaling factor mapping the `LISE++` beam energy-loss in MeV to the normalised MUSIC beam energy-loss of 6 a.u., and the same factor was applied to the calculated ^{13}N energy-loss in each strip. The expected dip was defined as the difference between the normalised beam signal and the scaled ^{13}N signal. Allowing for an assumed

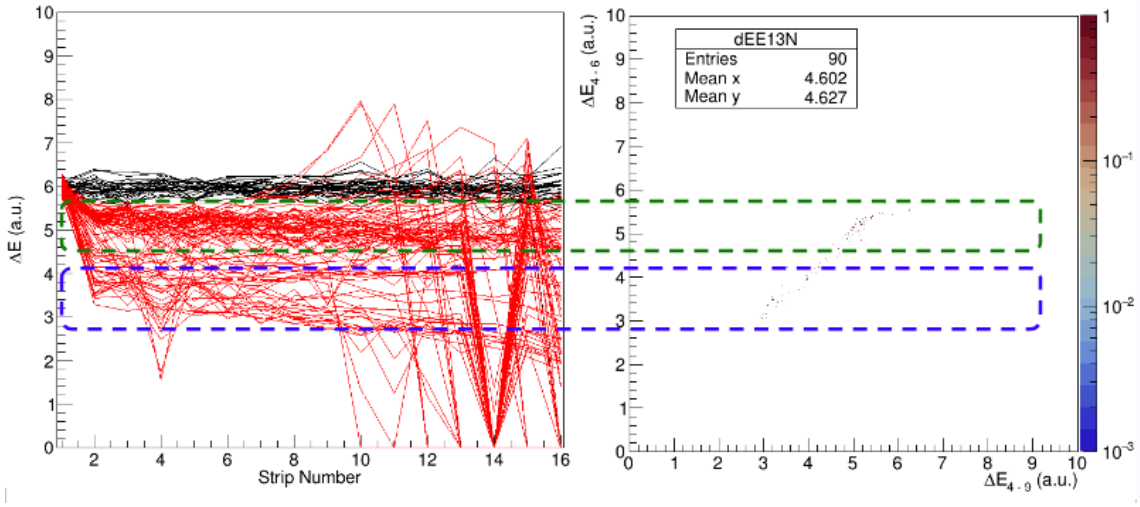

Figure 5.27: Events assigned to Strip 2 are classified according to their energy-loss behaviour. Left: representative energy-loss traces for the selected events. Right: corresponding two-dimensional ΔE distribution showing distinct event populations. Events with energy-loss in the range 4.8–5.6 a.u. are consistent with the expected signal from ^{13}N reaction products.

uncertainty of $\sim 10\%$ in stopping-power calculations, a $\pm 10\%$ interval was adopted to define an approximate dip range.

Table 5.3: Estimated ^{13}N energy-loss values derived from `LISE++` stopping-power calculations. The simulated values (MeV) were rescaled to the MUSIC analysis scale by normalising the calculated beam energy-loss to 6 a.u. The dip corresponds to the difference between the beam signal and the scaled ^{13}N signal. A $\pm 10\%$ interval defines the expected dip-search window.

Strip No.	`LISE++` ^{13}N E_{loss} (MeV)	Normalised ^{13}N E_{loss} (a.u.)	Dip Low (a.u.)	Dip High (a.u.)
2	3.7	5.0	0.79	1.24
3	3.8	5.0	0.79	1.24
4	3.9	5.0	0.77	1.22
5	4.1	5.1	0.75	1.20
6	4.2	5.1	0.74	1.19
7	4.4	5.1	0.71	1.16

Figure 5.27 reveals two distinct event populations below the beam peak. The first group, centred around $E_{\text{loss}} \approx 5.5$ a.u., is consistent with the expected ^{13}N energy-loss inferred from the stopping-power estimates. A second population appears at significantly lower energy-loss (≈ 3.5 a.u.), forming a separate cluster inconsistent with ^{13}N. This lower-energy group is attributed to recoiling ^{12}C nuclei originating

from beam-induced reactions in the detector gas. Candidate (p, α) events were required to sustain a reduction in energy-loss relative to the beam peak (6 a.u.) over a minimum of four consecutive strips. Specifically, the dip depth was required to satisfy

$$0.45 \leq \Delta E_{\mathrm{dip}} \leq 1.2 \text{ a.u.}$$

The lower bound of 0.45 a.u. corresponds to approximately three times the normalised beam energy-loss resolution ($\sigma \approx 0.15$ a.u.), ensuring that the dip represents a statistically significant deviation from the beam signal. The upper bound of 1.2 a.u. was chosen based on the observed separation between the ^{13}N population and the lower-energy cluster (Figure 5.27), preventing contamination from recoiling ^{12}C events. This interval, therefore, isolates the physically expected dip region while maintaining robust separation from both beam fluctuations and recoiling ^{12}C events.

5.6.4 Uniform Energy-Loss Behaviour and Derivative Constraint

After applying the energy-loss thresholds, the remaining events were examined for physical consistency along the detector length. Valid charged-particle tracks are expected to exhibit a smooth and gradually varying energy-loss profile across successive anode strips, reflecting continuous slowing down in the gas. A subset of events, however, showed sharp, non-physical variations in energy-loss between neighbouring strips, indicative of spurious or poorly reconstructed signals (Figure 5.28).

To suppress these events, a derivative constraint was applied by limiting the allowable change in energy-loss between consecutive strips to 1.0 a.u. Events exceeding this variation were rejected. Figure 5.29 illustrates the energy-loss traces and corresponding ΔE distributions after applying this condition. While variations

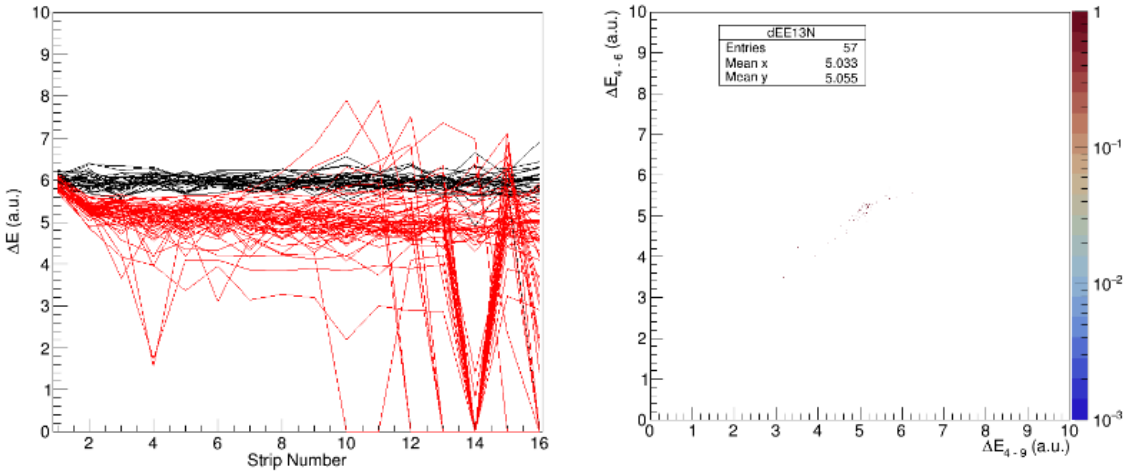

Figure 5.28: Events assigned to Strip 2 after excluding the lower-energy event group. Left panel: corresponding energy-loss traces for the selected events. Right panel: two-dimensional ΔE distribution after removal of the lower-group events.

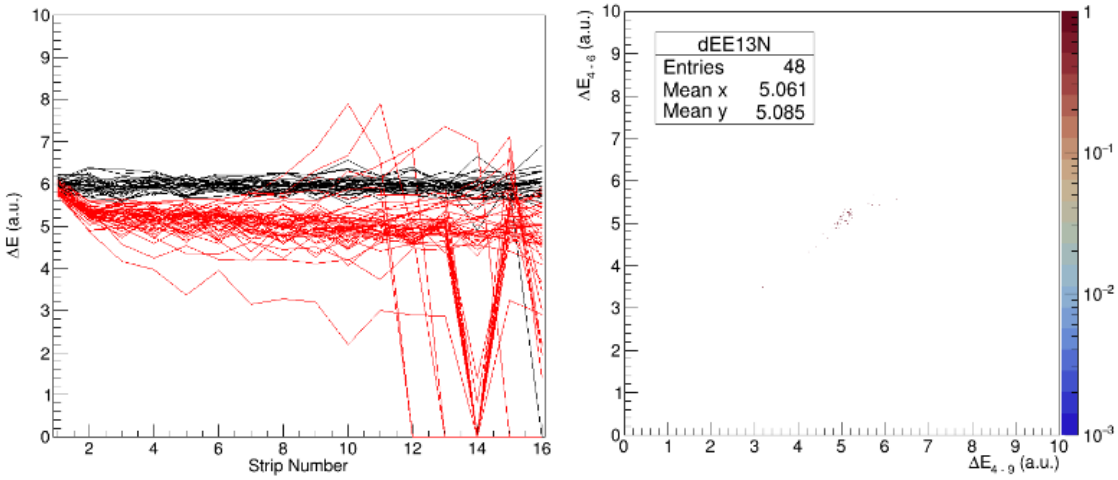

Figure 5.29: Events assigned to Strip 2 after applying the derivative condition, which limits the allowable variation in energy-loss between consecutive strips to 1.0 a.u. Left panel: energy-loss traces satisfying the derivative condition. Right panel: two-dimensional ΔE distribution after applying this selection.

of up to 2 a.u. are observed before the cut (Figure 5.28), only smoothly varying traces with a maximum strip-to-strip variation of 1.0 a.u. remain afterwards.

5.6.5 Summary of Accepted (p, α) Events

The overall procedure used to isolate $^{16}\mathrm{O}(\mathrm{p}, \alpha)^{13}\mathrm{N}$ events in the MUSIC detector is summarised in Figure 5.30. Following event reconstruction, a gate on the energy-loss in strip 1 is first applied to select particles corresponding to beam ions entering the active gas volume. Multiplicity and continuity conditions are then imposed to ensure physically consistent particle trajectories across successive strips. Candidate (p, α) reaction events are subsequently identified through a sustained reduction in energy-loss relative to the unreacted beam, consistent with the expected $^{13}\mathrm{N}$ signature. A final smoothness (derivative) constraint is applied to suppress events exhibiting non-physical fluctuations in the energy-loss profile. Events satisfying all selection criteria are classified as (p, α) candidates,while events failing any condition are rejected.

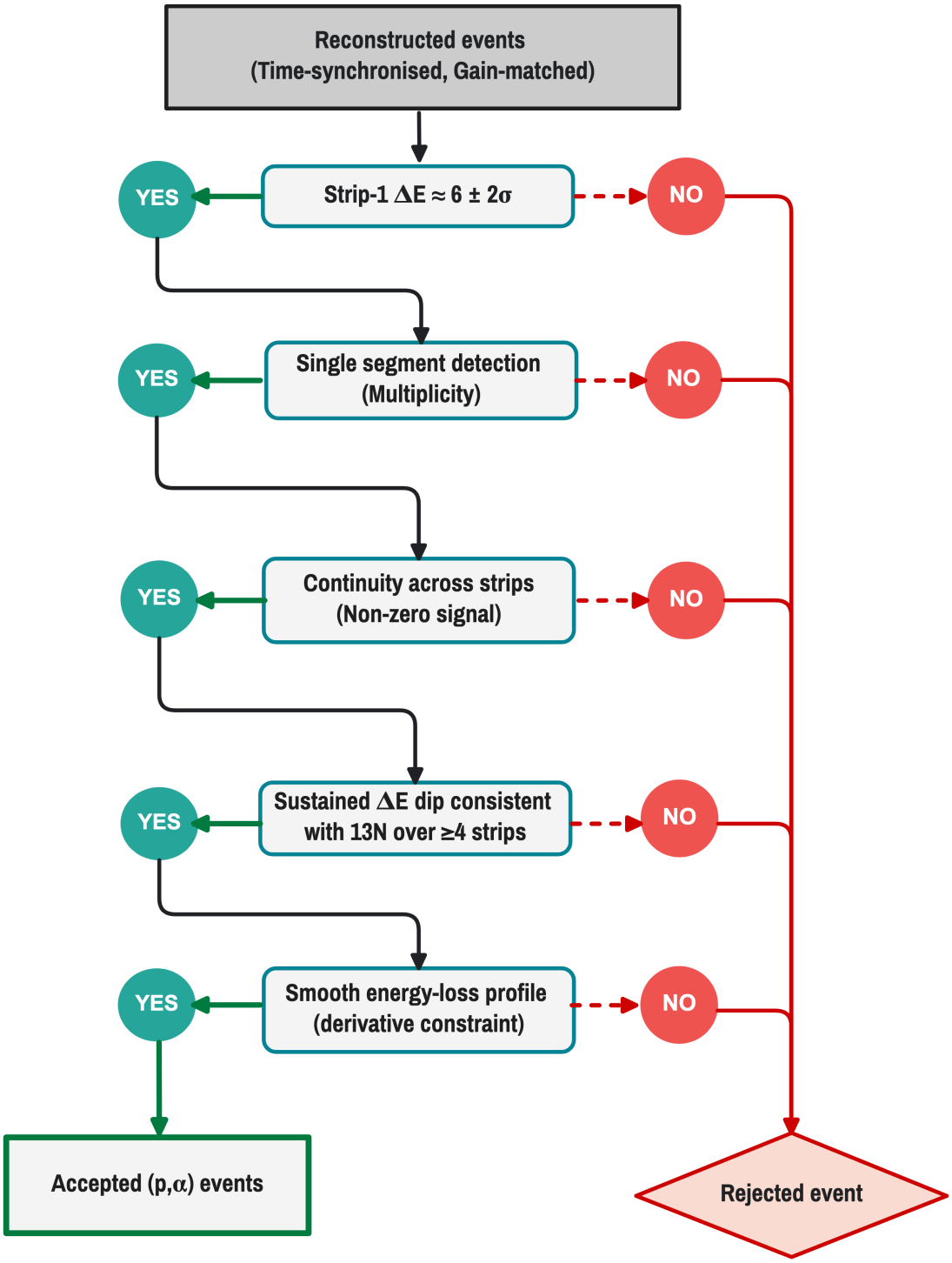

Figure 5.30: Decision tree illustrating the selection of $^{16}\mathrm{O}(\mathrm{p},\alpha)^{13}\mathrm{N}$ events in the MUSIC detector. Events are required to satisfy a strip 1 beam gate, multiplicity and continuity conditions, a characteristic $^{13}\mathrm{N}$ energy-loss dip, and a final smoothness constraint. Events fulfilling all criteria form the accepted (p,α) sample, while events failing any condition are rejected.

5.7 Reaction Yield per Anode Strip

The results of the final (p, α) event selection for strips 2 through 6 are shown in Figures 5.31–5.35. For the ΔE–ΔE representations, energy-loss was summed over three consecutive strips along the horizontal axis and seven consecutive strips along the vertical axis. Each summed value was then divided by the number of contributing strips to obtain the strip-averaged energy-loss. This approach preserves the normalisation of the gain-matched scale, maintains the unreacted beam at $\Delta E \approx 6$ a.u., and enhances the statistical stability of the distributions. As can be seen, the extracted reaction yield decreases rapidly with increasing strip number. Well-defined clusters of (p, α) events are observed in the earlier strips, whereas the separation between reaction events and background becomes progressively less distinct in the later strips (5–6). By strip 6, only a small number of events remain in the expected reaction region, with extracted yields ranging from zero to a few counts depending on the selection configuration. In this low-count regime, statistical fluctuations dominate, and the (p, α) signal can no longer be reliably distinguished from background.

The rapid reduction in yield is primarily attributed to the strong suppression of the $^{16}O(p, \alpha)^{13}N$ cross-section by the Coulomb barrier at lower energies. Furthermore, the 35% event loss caused by irregular behaviour in strip 3 has complicated event classification in the subsequent strips. Owing to these limitations, reaction yields beyond strip 6 were not considered reliable, and the quantitative analysis was restricted to strips 2 through 6.

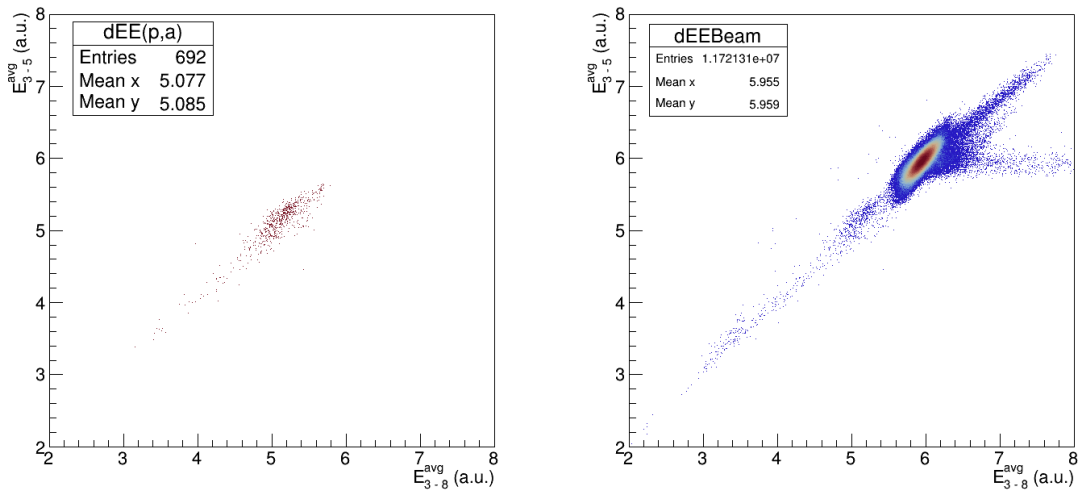

Figure 5.31: Final event selection for Strip 2 after applying all analysis conditions. Left panel: events identified as candidate (p, α) reactions. Right panel: full filtered event distribution, including unreacted beam and reaction events. The (p, α) events are clearly separated from the beam background.

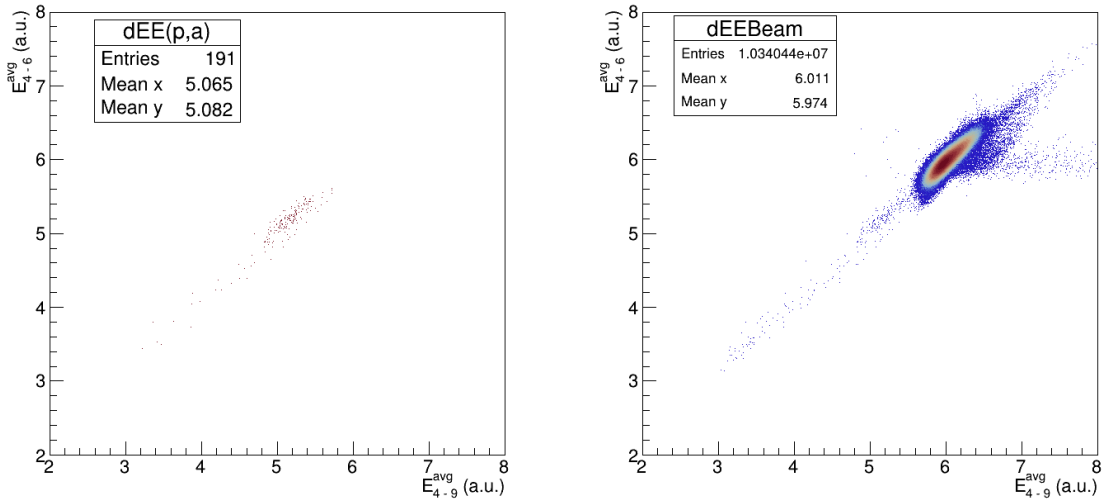

Figure 5.32: Final event selection for Strip 3 after applying all analysis conditions. Left panel: events identified as candidate (p, α) reactions. Right panel: full filtered event distribution, including unreacted beam. A clear separation between the (p, α) events and the beam is maintained.

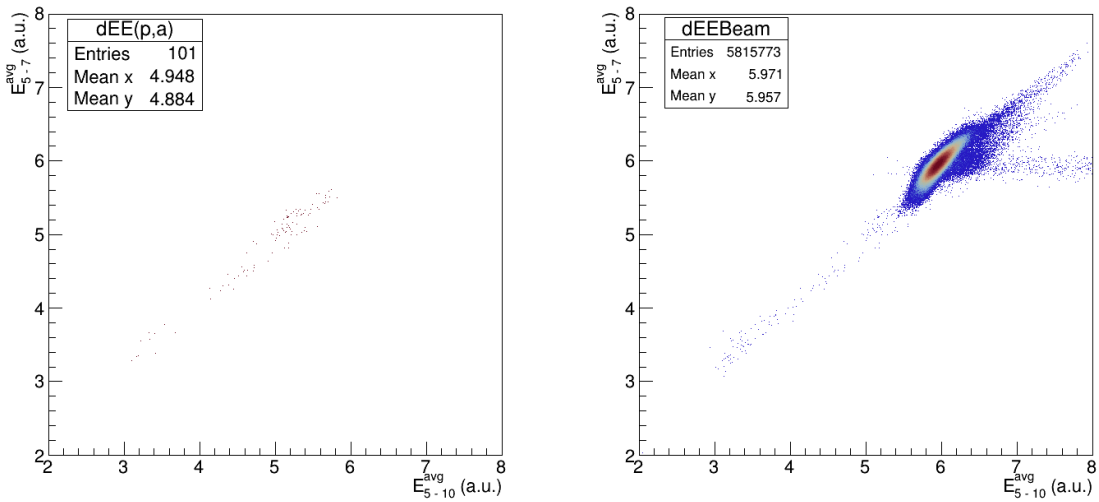

Figure 5.33: Final event selection for Strip 4 after applying all analysis conditions. Left panel: events identified as candidate (p, α) reactions. Right panel: full filtered event distribution. Compared to earlier strips, the separation between reaction events and background becomes less distinct.

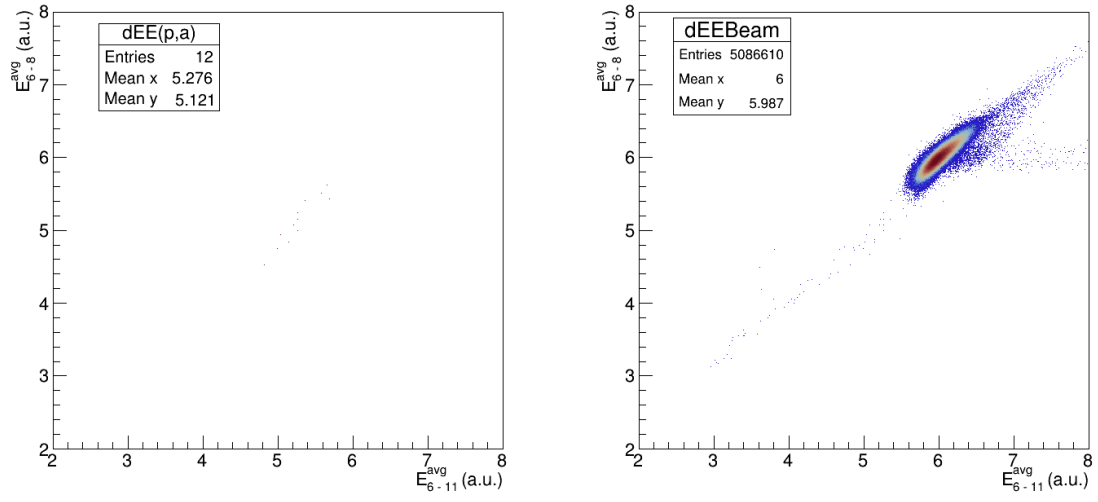

Figure 5.34: Final event selection for Strip 5 after applying all analysis conditions. Left panel: events identified as candidate (p, α) reactions. Right panel: full filtered event distribution. No well-defined cluster of reaction events is observed at this stage.

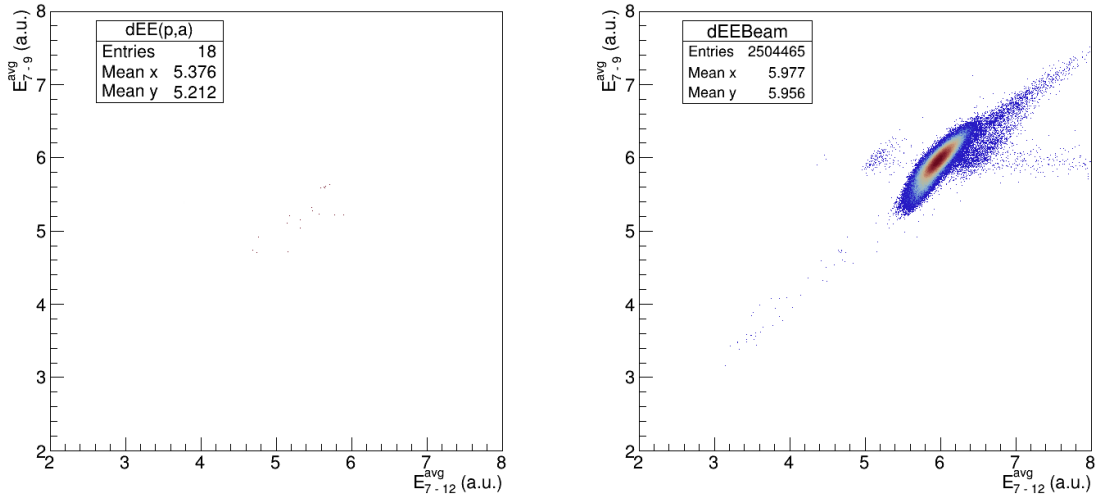

Figure 5.35: Final event selection for Strip 6 after applying all analysis conditions. Left panel: events identified as candidate (p, α) reactions. Right panel: full filtered event distribution. Only a small number of isolated events remain in the expected reaction region.

5.8 Beam Events Counting

Beam events are defined as unreacted ^{16}O ions entering the detector gas and propagating through the MUSIC detector without undergoing a nuclear reaction. Accordingly, beam events were selected by requiring single-segment signal deposition (multiplicity requirement) and a continuous energy-loss trace across the detector anode strips (continuity requirement). In addition, the energy-loss was required to lie within a $6 \pm 2\sigma$ window around the beam centroid for the first eight strips, ensuring a consistent beam-like behaviour. Following these selections, the beam count was evaluated for the the strips of (1-9) independently in each strip. A residual strip-to-strip variation of approximately 3% was observed, primarily attributed to energy straggling and detector response fluctuations. This variation was propagated as a systematic uncertainty in the cross-section calculation as will be discussed next.

5.9 Statistical and Systematic Uncertainties

The identification of (p, α) events relies on the application of multiple selection criteria, as described in Sections 5.6.2, 5.6.3, and 5.6.4. However, the exact numerical cutoffs are not uniquely defined but must be chosen within physically reasonable intervals. As a result, alternative choices of selection parameters can lead to small variations in the extracted reaction yields. The resulting variation in the extracted (p, α) events count reflects the sensitivity of the analysis to the choice of event-selection criteria and was therefore treated as a systematic uncertainty.

In addition, the counting of discrete reaction events is fundamentally subject to statistical fluctuations due to the random nature of nuclear processes and finite event statistics. Consequently, the statistical uncertainty associated with each reaction yield was evaluated assuming Poisson statistics [115], based on the number of events counted in each strip. For low-count regimes, confidence intervals consistent with the Feldman-Cousins [116] approach were adopted to ensure proper statistical coverage.

Systematic uncertainty from event selection

To quantify the systematic uncertainty in the current analysis, the strip yields were collected from four independent event-selection configurations. For each configuration, the full analysis chain was repeated, and the reaction yield was extracted independently for each anode strip. The configurations were designed to span a range of physically reasonable event-selection criteria, progressing from an optimised, restrictive selection to increasingly relaxed conditions to account for potential variations in event behaviour. The most restrictive configuration corresponds to the optimal expectation for clean (p, α) events, requiring the multiplicity and continuity conditions

to be satisfied across all strips (1–10), together with tight limits on the allowable strip-to-strip variation in energy-loss (derivative constraint = 0.9) and on the dip between the beam and ^{13}N energy-loss parameter (0.5–0.95). Recognising that genuine events may exhibit additional broadening due to energy straggling, angular effects, or proximity to the beam envelope, subsequent configurations progressively relaxed these requirements by reducing the number of strips over which continuity was enforced (1–8), allowing larger variations in energy-loss between adjacent strips (derivative constraint = 0.9), and widening the permitted dip range (0.45–1.1). A further configuration allowed a wider dip range (0.4–1.2), fewer strips required to satisfy the continuity and multiplicity conditions (1–6), and a larger derivative limit (derivative constraint = 1.5). The loosest configuration was chosen to accommodate rare but physically possible cases, such as events occurring near the beam envelope that produce large-angle trajectories, or situations in which α particles emitted in association with the formation of ^{13}N generate signals simultaneously with ^{13}N, resulting in both anode segments being triggered. In this configuration, the multiplicity requirement was removed, and the derivative condition was further relaxed (derivative constraint = 2). Together, these configurations span the reasonable range of event-selection choices while preserving physically meaningful (p, α) tracks.

The event counts obtained for a given strip under the four configurations are listed in Table 5.4. The mean of these values was adopted as the nominal reaction yield for that strip. The systematic uncertainty associated with event selection was quantified as the standard deviation of the yields obtained from the four configurations.

Table 5.4: Reaction yields per anode strip obtained from four independent event-selection configurations. For each strip, the minimum and maximum yields bracket the spread due to cut variation. The nominal yield is taken as the mean of the four configurations. The systematic uncertainty from event selection is given by the standard deviation of the yields.

Strip	$\text{Yield}_{\text{min}}$ (counts)	$\text{Yield}_{\text{max}}$ (counts)	Mean Yield (counts)	σ_{sys} (counts)
6	0	2	1	0.96
5	7	9	8	0.96
4	65	78	72	5.91
3	159	189	175	15.20
2	602	750	668	61.67

Statistical uncertainty

Statistical uncertainties were evaluated based on counting statistics. For strips with sufficiently large event counts, the statistical uncertainty was calculated assuming Poisson statistics [115], where the standard deviation is given by $\sqrt{N}$, with N the number of detected events. For strips with low event statistics ($N < 30$), the Gaussian approximation to the Poisson distribution ($\sigma = \sqrt{N}$) is no longer valid, and the resulting confidence intervals become intrinsically asymmetric. In these cases, confidence intervals were determined using the Feldman–Cousins unified approach [116], which provides a statistically rigorous approximation in the low-count regime.

Table 5.5: Statistical uncertainties associated with the mean reaction yields per strip. For low-count strips ($N < 30$), asymmetric confidence intervals were determined using the Feldman–Cousins unified approach [116]. For higher statistics, symmetric uncertainties based on the Gaussian approximation to the Poisson distribution ($\sigma = \sqrt{N}$) were adopted [115]. All uncertainties correspond to one standard deviation (68% confidence level).

Strip	Mean Yield (counts)	σ^{-}_{stat} (counts)	σ^{+}_{stat} (counts)	Method
6	1	0.7	4.3	Feldman–Cousins
5	8	2.8	7.8	Feldman–Cousins
4	72	8	8	$\sqrt{N}$
3	175	13	13	$\sqrt{N}$
2	668	26	26	$\sqrt{N}$

5.10 Cross-Section Calculation

Following the event-identification procedure described in Section 5.7, the cross-section of the $^{16}\mathrm{O}(\mathrm{p},\alpha)^{13}\mathrm{N}$ reaction was determined independently for each active anode strip of the MUSIC detector. In this experiment, each anode strip samples a distinct centre-of-mass energy interval, together covering the range $E_{\mathrm{c.m.}} = 5.8$–6.9 MeV. The mean number of detected (p,α) events in each strip was taken as the reaction yield (Tables 5.4 and 5.5). The cross-section for each strip was then calculated using:

$$\sigma = \frac{N_{p\alpha}}{N_{\mathrm{beam}}\, n_{\mathrm{H}}\, \ell} \times 10^{27}, \tag{5.9}$$

where $N_{p\alpha}$ is the number of detected (p,α) reaction events in the strip, N_{beam} is the number of unreacted beam particles traversing the detector under identical selection conditions (See Section 5.8), n_{H} is the hydrogen number density in the methane gas target, and ℓ is the effective target thickness corresponding to a single anode strip. The factor 10^{27} converts the cross-section from cm^2 to millibarns (mb).

During the experiment, the methane gas pressure was maintained at 710 Torr, corresponding to a total gas mass density of $6.1 \times 10^{-4}\ \mathrm{g\,cm^{-3}}$. Since hydrogen accounts for 25% of the methane molecular mass, the resulting hydrogen mass density is $1.53 \times 10^{-4}\ \mathrm{g\,cm^{-3}}$. This value was converted to a hydrogen number density using Avogadro's constant. The target width per anode strip (ℓ) was (15.8) cm.

The extracted cross-section values and their total uncertainties are listed in Table 5.6. The total uncertainty includes the 3% beam-normalisation uncertainty (Section 5.8), systematic uncertainties arising from event identification (Section 5.9), and statistical uncertainties from event counts (Section 5.9). All contributions were propagated at the cross-section level and combined in quadrature. For low-statistics points, the resulting uncertainties are asymmetric. The quoted centre-of-mass en-

ergies correspond to the energies determined for each strip, with their associated energy uncertainties in Section 5.2.6.

Table 5.6: Measured cross-sections for the $^{16}O(p,\alpha)^{13}N$ reaction obtained using the MUSIC detector. Total uncertainties include statistical and systematic contributions, together with a 3% beam count uncertainty combined in quadrature. For low yield anodes, asymmetric uncertainties are reported.

$E_{c.m.}$ (MeV)	$\Delta E_{c.m.}$ (MeV)	σ (mb)	$\Delta\sigma_{tot}$ (mb)
5.78	0.15	0.01	$^{+0.03}_{-0.01}$
6.07	0.15	0.10	$^{+0.05}_{-0.03}$
6.36	0.14	0.95	0.12
6.64	0.14	2.30	0.20
6.91	0.13	8.80	0.50

The resulting cross-sections are shown in Figure 5.36 and compared with previously published experimental datasets and theoretical evaluations. The present MUSIC data extend the experimental coverage in the lower-energy region and provide new constraints where earlier measurements showed large systematic uncertainties.

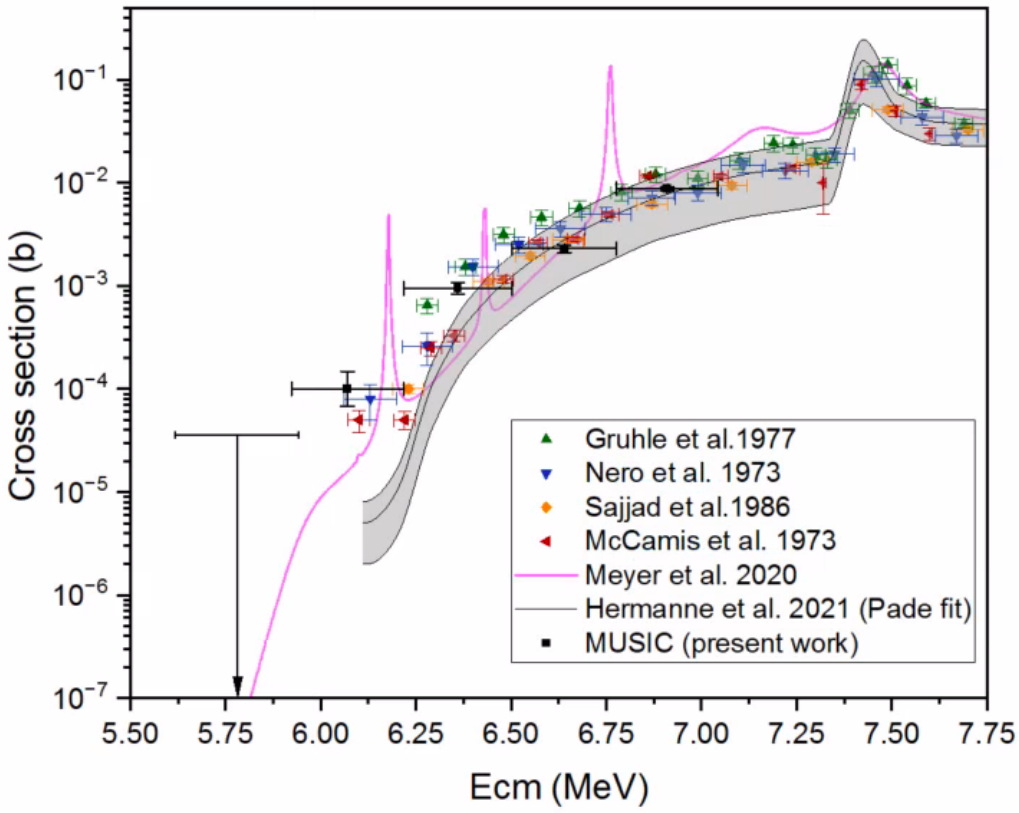

Figure 5.36: Measured cross-sections of the $^{16}\mathrm{O}(\mathrm{p},\alpha)^{13}\mathrm{N}$ reaction obtained with the MUSIC detector (present work), compared with previous experimental data from Gruhle *et al.* (1977), Nero *et al.* (1973), Sajjad *et al.* (1986), and McCamis *et al.* (1973). The data are also compared to the evaluation by Meyer *et al.* (2020) and the statistical Padé fit of Hermanne *et al.* (2021). The downward arrow at $E_{\mathrm{c.m.}} = 5.78$ MeV shows an upper limit for cross-section obtained from strip 6.

5.11 Investigation of Unexpected Event Loss

During the analysis of (p, α) events, an unexpected loss of approximately 35% of the total events was observed after applying the continuity selection criteria (see Section 5.6.2). Preliminary inspection suggested that this loss was associated with strip 3. However, it was not immediately clear whether this behaviour originated from a hardware failure of the response in strip 3 itself, from cumulative effects across multiple strips, or from artefacts introduced during pre-analysis processing.

This section documents a systematic investigation undertaken to identify the origins of this event loss, and to assess their potential impact on the extracted reaction yields and associated uncertainties.

5.11.1 Energy Distribution Across Anode Strips

First, the energy-loss spectra were checked for each anode strip before applying any selection conditions. This step was done to confirm that the detector was working properly and that all anode channels were active and consistent. Figure 5.37 presents the normalised energy-loss distributions across the first six anode strips before any gating was applied. All strips exhibit a dominant peak centred at approximately 6 a.u., corresponding to the expected energy-loss of the normalised beam. In addition, a smaller secondary peak around 12 a.u. is observed. This secondary structure was previously identified as a pileup artefact originating in strip 1 (see Figure 5.20) and was successfully suppressed by applying a beam-selection gate on strip 1, as demonstrated in Figure 5.38. After applying a $6 \pm 2\sigma$ selection condition on strip 1, the secondary peak is fully removed across all strips, confirming that pileup does not contribute to the investigated event loss.

Despite this correction, strip 3 exhibits a distinct anomaly. While the beam peak in all other strips is centred at a normalised energy of 6±0.148 a.u., the corresponding peak in strip 3 is systematically shifted downward to approximately 4 a.u. This deviation is clearly visible in Figs.(5.37 and 5.38) and is not observed in neighbouring strips. Importantly, prior to applying continuity conditions, the total number of recorded events in strip 3 is comparable to those in the other strips, indicating that the anomaly does not originate from a simple loss of detection efficiency.

Next, only the continuity condition (described in Section 5.6.2) was applied across multiple strips (0–12). Upon applying this criterion, a sudden and substantial reduction in the surviving event population is observed, as shown in Figure 5.39. This demonstrates that the 35% event loss is introduced specifically by the continuity requirement, rather than by earlier stages of the analysis.

Therefore, the continuity condition is identified as the direct cause of the observed event loss. However, the underlying origin of this behaviour remains unclear and requires further investigation. In addition, the possibility of recovering these events through a re-examination of the raw detector signals justifies further study.

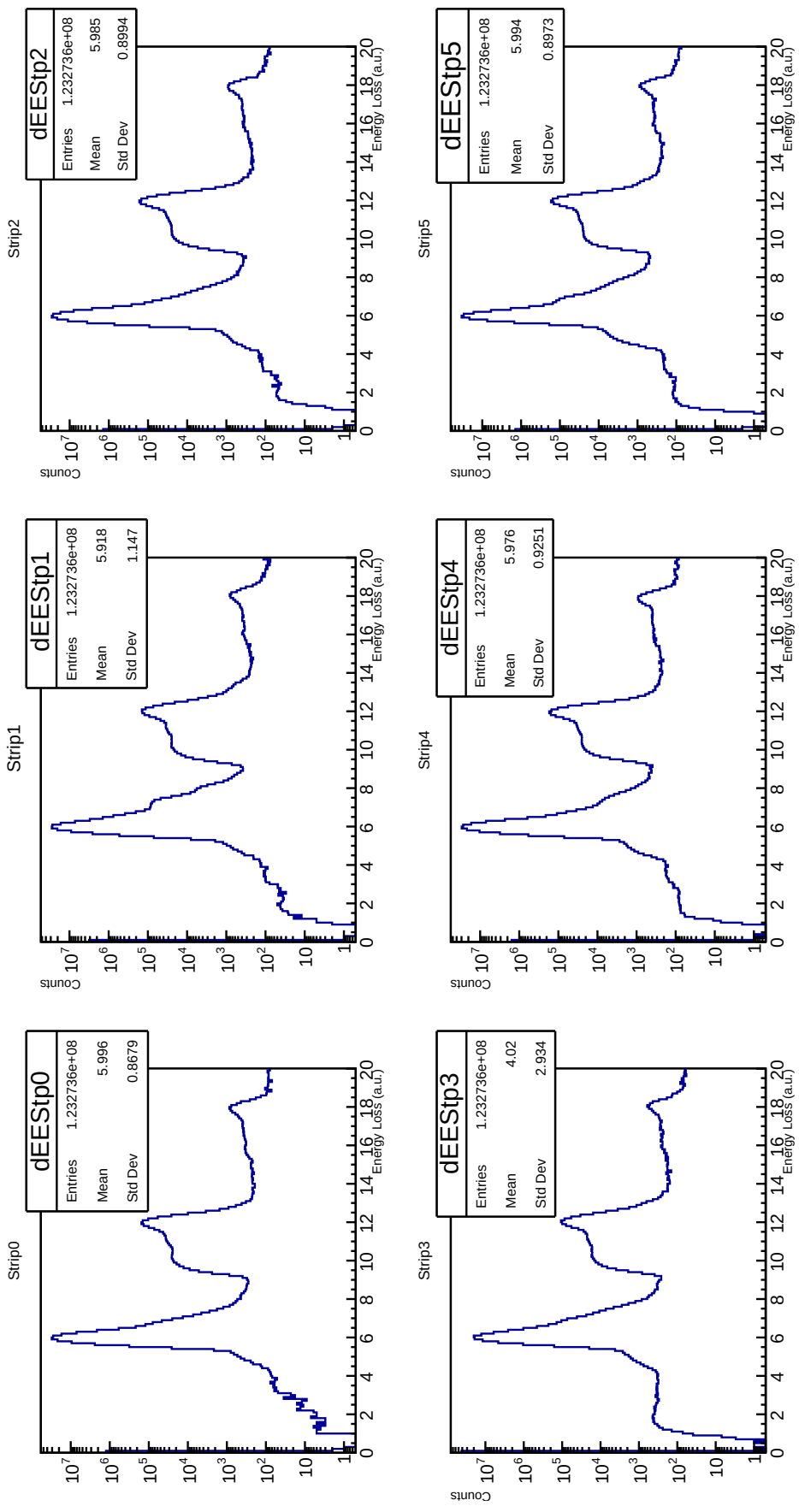

Figure 5.37: Normalised energy-loss spectra recorded in the first six anode strips of the MUSIC detector prior to the application of any selection criteria. All strips exhibit a dominant beam peak centred at approximately 6 a.u., indicating uniform detector response, except for strip 3, where the peak is systematically shifted to lower energy (around 4 a.u.). A secondary structure near 12 a.u. is observed in all strips and is attributed to pileup originating in strip 1. This comparison provides an initial verification of strip functionality and reveals an anomalous energy response specific to strip 3.

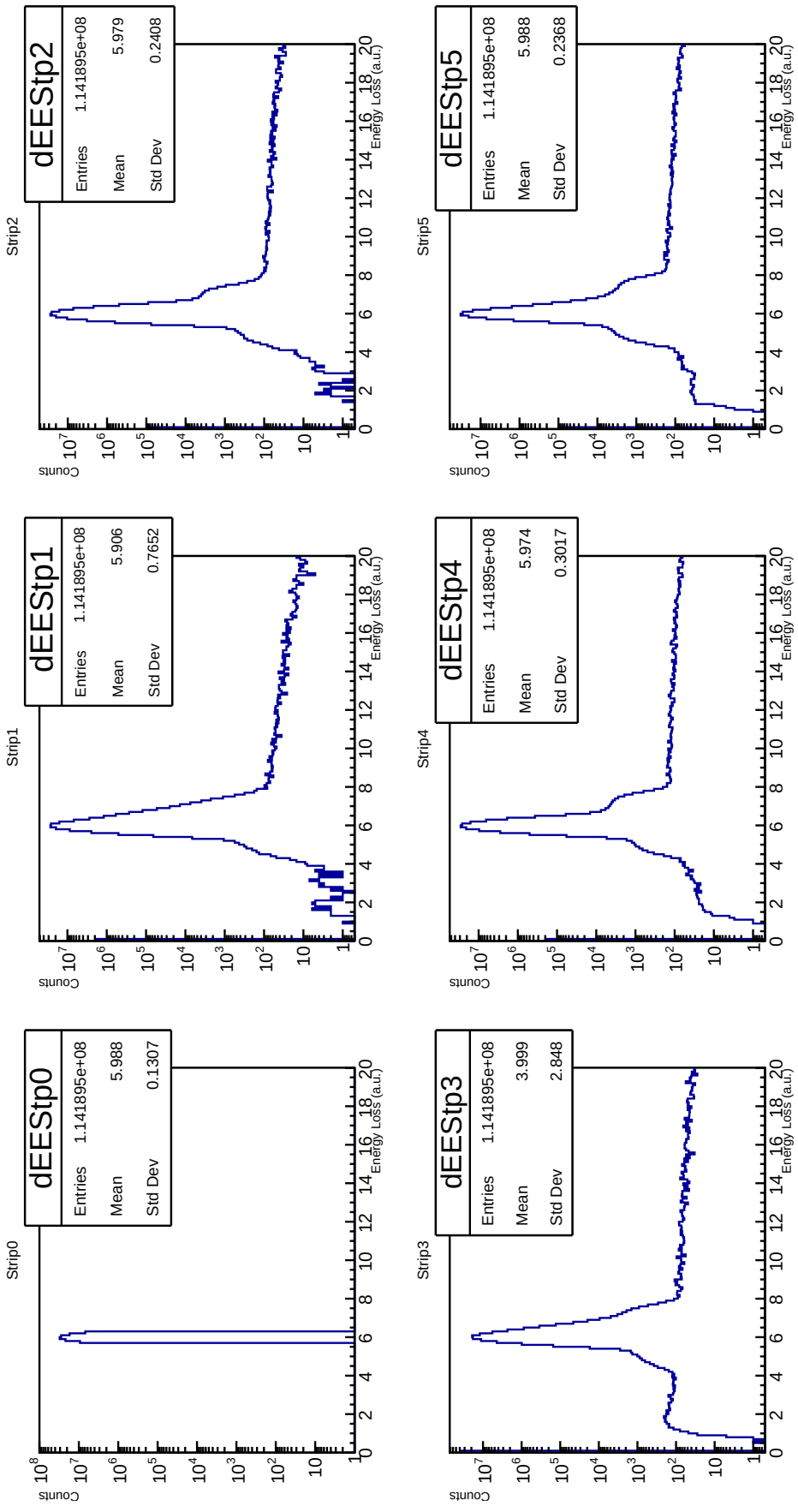

Figure 5.38: Normalised energy-loss spectra across the first six anode strips after applying a $6 \pm 2\sigma$ beam-selection gate on strip 1. The secondary peak at 12 a.u., previously attributed to pileup, is fully suppressed. The anomalously low mean energy observed in strip 3 persists after this correction, demonstrating that the deviation is not caused by pileup or entrance-region effects.

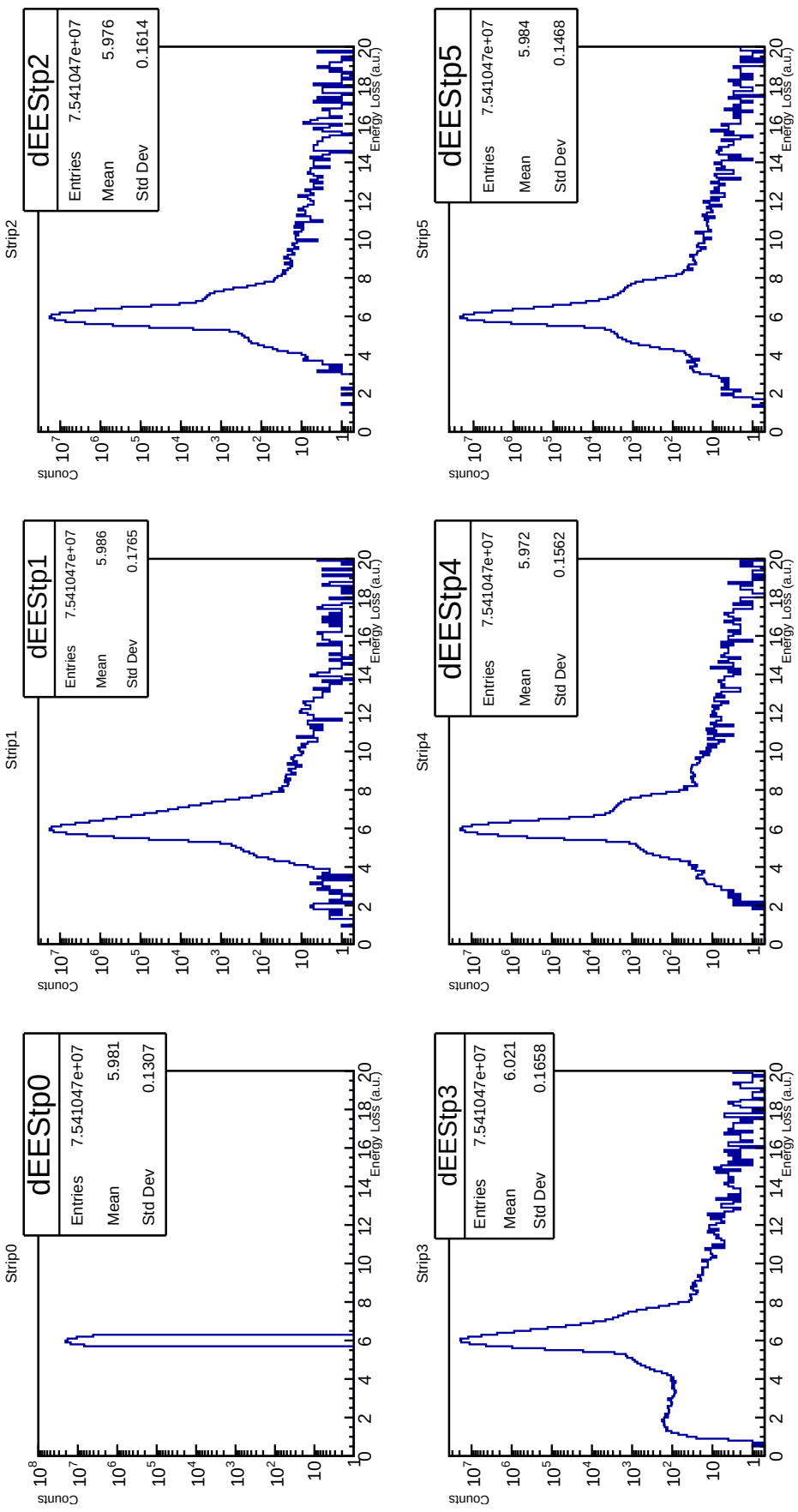

Figure 5.39: Normalised event distributions across the first six anode strips after applying the continuity requirement. A substantial reduction in the surviving event population is observed following the application of the continuity condition, with the total number of entries decreasing from 1.14×10^8 to 7.54×10^7, corresponding to approximately 65% of the entries prior to applying the continuity cut. This behaviour indicates that the anomalous energy response of strip 3 is directly linked to the continuity condition.

5.11.2 Strip-by-Strip Assessment of the Continuity Condition

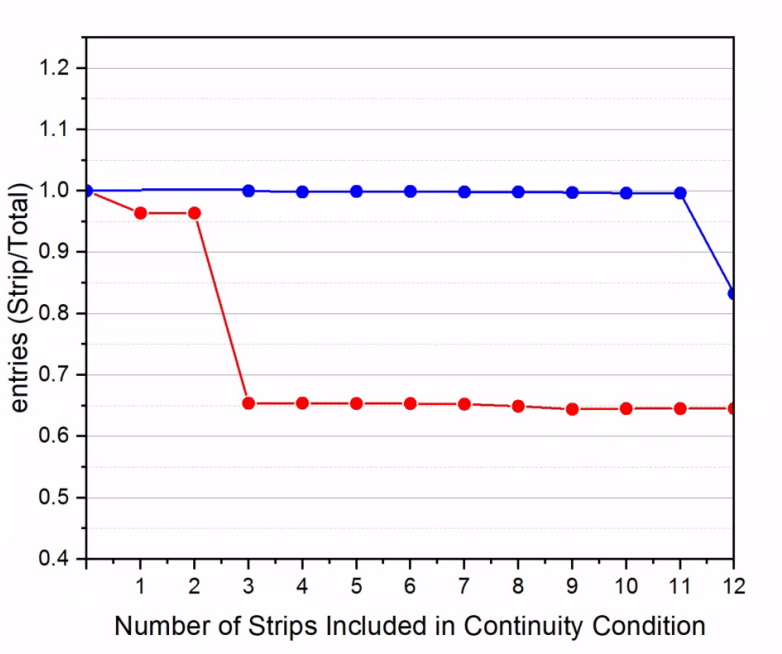

Figure 5.40: Effect of incrementally applying the continuity condition across successive anode strips, shown as the ratio of the surviving event count to the total event count prior to applying the continuity requirement. The red curve shows the normalised surviving population as additional strips are included, revealing a sharp reduction when strip 3 is introduced. The blue curve shows the corresponding ratio when the continuity condition is applied across strips 0–12, except for strips 1 and 3, which are excluded from the continuity requirement, demonstrating that no comparable losses occur in other strips within the active analysis region. This behaviour identifies strip 3 as the dominant source of continuity-induced event loss.

To determine whether the observed 35% event loss originated uniquely from strip 3 or resulted from cumulative effects across multiple strips, the continuity condition was applied incrementally. Starting from strip 0 (no continuity requirement), successive strips were added one at a time while monitoring the surviving event count.

As shown in Figure 5.40, inclusion of strip 1 resulted in only a minor ($\sim$ 3%) reduction in event count, consistent with expected fluctuations. Adding strip 2 produced no further reduction. However, once strip 3 was included, the event count

dropped suddenly by approximately 35%. Adding additional strips beyond strip 3 had no further significant impact.

Conversely, when strip 3 (and strip 1) were excluded from the continuity requirement, no comparable loss was observed until strip 12, which lies well beyond the region relevant to the present analysis. This unambiguously identifies strip 3 as the dominant source of the continuity-related event loss.

5.11.3 Ruling Out Gain-Matching and Pre-Analysis Effects

To verify that the anomalous behaviour observed in strip 3 did not originate from gain-matching corrections or other pre-analysis processing steps (Section 5.5), the investigation was extended to the raw, digitiser-level data, prior to any calibration, normalisation, or event-building procedures.

Figure 5.41 compares the unprocessed energy distributions recorded in strip 2 and strip 3. The total number of recorded entries in both strips is comparable, demonstrating that events are not physically missing at the digitisation stage. However, when Gaussian fits are applied around the respective beam peaks, the number of events contributing to the peak region in strip 3 is approximately 35% lower than in strip 2.

Because this problem is already present in the raw digitiser output, it cannot be attributed to gain-matching, energy normalisation, or any subsequent pre-analysis correction. Instead, it indicates that a significant fraction of events in strip 3 is recorded with systematically reduced pulse amplitudes at the hardware level, shifting them outside the nominal beam peak region. This interpretation is further supported by operational logs indicating that strip 3 was connected to digitiser Board 3, which

experienced multiple communication errors and resets during the experiment.

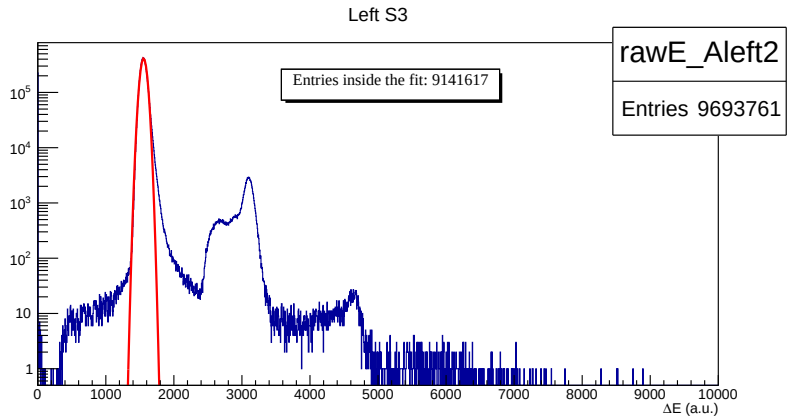

(a) Gaussian distribution and number of entries in the raw data for the left (L) segment of strip 2.

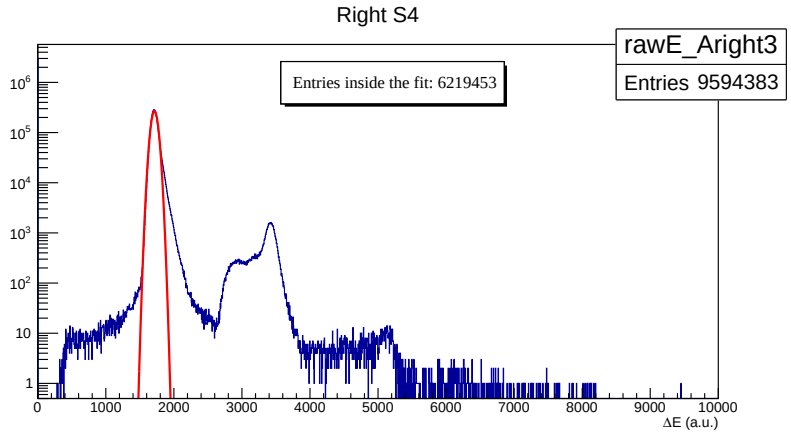

(b) Gaussian distribution and number of entries in the raw data for the right (R) segment of strip 3.

Figure 5.41: Comparison of raw digitiser-level energy spectra for the left (L) segment of strip 2 and the right (R) segment of strip 3. (a) Strip 2 exhibits a well-defined Gaussian beam peak containing the majority of recorded events. (b) Strip 3 shows a markedly reduced population within the corresponding peak region, with only ∼65% of events contributing, despite a similar total number of digitiser entries. This demonstrates that the event deficit in strip 3 is already present at the hardware readout stage and is not introduced by subsequent analysis or calibration procedures.

5.11.4 Origin of the Event Loss Observed in Strip 3

As discussed above, despite the substantial event loss observed after applying the continuity condition, strip 3 records approximately the same total number of raw

events as the other strips when no selection criteria are applied. This demonstrates that events are not physically missing, but are instead misclassified during analysis due to anomalous energy deposition in this strip. Figure 5.42 shows the ΔE distri-

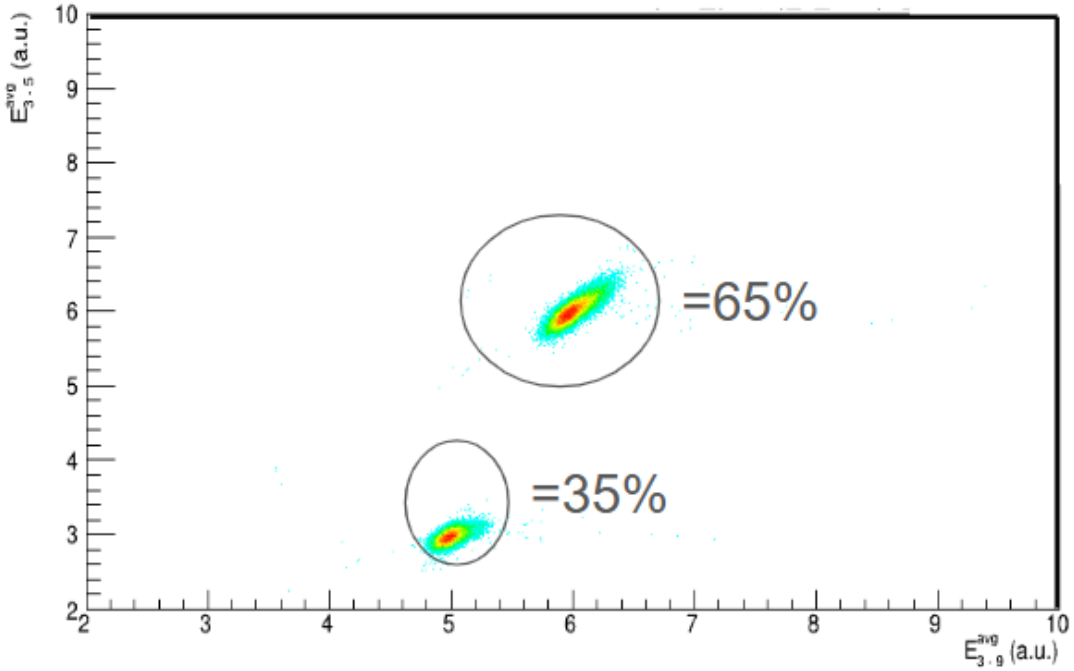

Figure 5.42: ΔE distribution of strip 3, showing two distinct clusters. The primary cluster, centred at approximately 6 a.u., contains ∼65% of the total events and corresponds to the expected beam energy-loss. A secondary cluster at 3–4 a.u., accounting for the remaining ∼35%, exhibits a similar spectral shape, indicating under-collected charge for a subset of otherwise valid beam events.

bution for strip 3, revealing two clearly separated populations. The primary cluster, centred at the expected beam energy-loss value of approximately 6 a.u., contains about 65% of the recorded events. A secondary cluster, located at significantly lower energy-loss (3–4 a.u.), accounts for the remaining ∼35% of the total event population and exhibits a shape closely resembling that of the primary beam peak.

Importantly, events belonging to this low-energy cluster in strip 3 exhibit normal energy-loss values in all subsequent strips. Figures 5.43 and 5.44 illustrate this behaviour by comparing the same set of events when the average energy-loss is calculated starting from strip 4 instead of strip 3. In this case, the beam distribution

returns to its expected centroid at approximately 6 a.u., and the secondary cluster near 4 a.u. disappears, while the total number of entries remains conserved. This confirms that these events correspond to genuine beam particles whose charge collection is underestimated exclusively in strip 3. Because the continuity condition requires consistent and detectable energy deposition in each consecutive strip, events with a reduced signal in strip 3 are rejected, resulting in a loss of approximately 35% of the events.

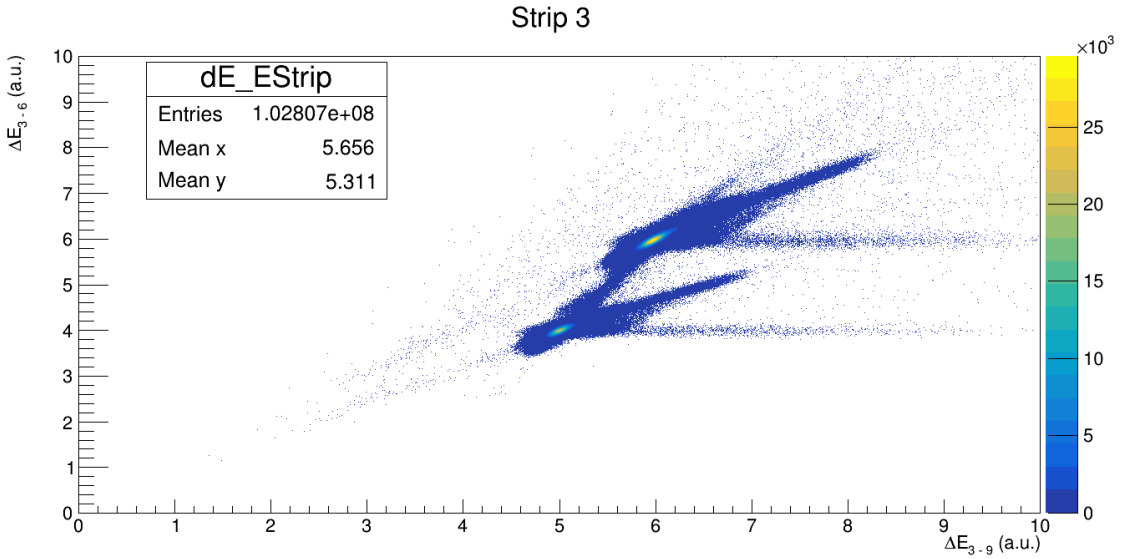

Figure 5.43: ΔE distribution of strip 3 obtained when the energy averaging procedure includes strip 3 itself. The secondary low-energy cluster at 3–4 a.u. is clearly visible, demonstrating the presence of a substantial fraction of under-collected events.

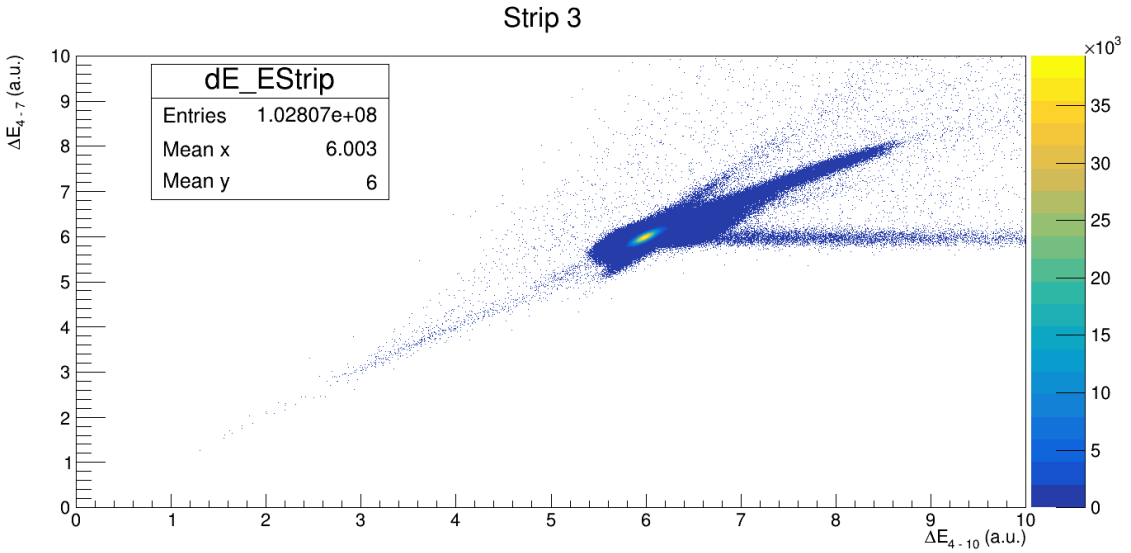

Figure 5.44: Same ΔE distribution as in Figure 5.43, but with the energy averaging starting from strip 4 instead of strip 3. The disappearance of the low-energy cluster confirms that these events deposit normal energy in all subsequent strips, establishing that the anomaly is localised exclusively to strip 3.

5.11.5 Impact of Strip 3 issue on the Calculated cross-section

To quantify the impact of the strip 3 anomaly on the extracted physics results, a controlled comparison was performed in which the cross-section was recalculated under two analysis configurations: (i) with strip 3 included in the continuity condition, and (ii) with strip 3 excluded from the continuity requirement. The resulting cross-sections are summarised in Table 5.7.

The comparison shows that the extracted cross-sections differ by no more than 5% across strips 1–3. This variation is comparable to the combined statistical and systematic uncertainties of the measurement, indicating that the strip 3 anomaly does not introduce a significant bias in the extracted cross-section values.

While excluding strip 3 from the continuity condition increases the total number of events, it significantly degrades the quality of event separation, particularly in the low-statistics strips. This effect is illustrated in Figs. 5.45 and 5.46, where the loss of

Table 5.7: Comparison of extracted cross-section values for strips 1–3 obtained with strip 3 included in, and excluded from, the continuity condition. The quoted variation represents the relative difference between the two analysis strategies.

Analysed Strip	**strip 3 included Cross-section (mb)**	**strip 3 excluded Cross-section (mb)**	**Variation (%)**
Strip 2	8.8	9.2	5%
Strip 3	2.3	2.5	5%
Strip 4	0.95	0.99	5%

continuity leads to increased background contamination and reduced discrimination between beam and reaction products. Under these conditions, event classification becomes ambiguous, and the reliability of the extracted yields is compromised.

For this reason, the analysis adopted the more conservative approach of retaining the continuity condition and excluding the affected events. Although this choice results in a reduced event sample and hence increased statistical uncertainty, it ensures superior background suppression and more robust event identification.

This study demonstrates that the strip 3 anomaly does not systematically bias the extracted cross-sections and that its impact is fully controlled within the adopted uncertainty framework.

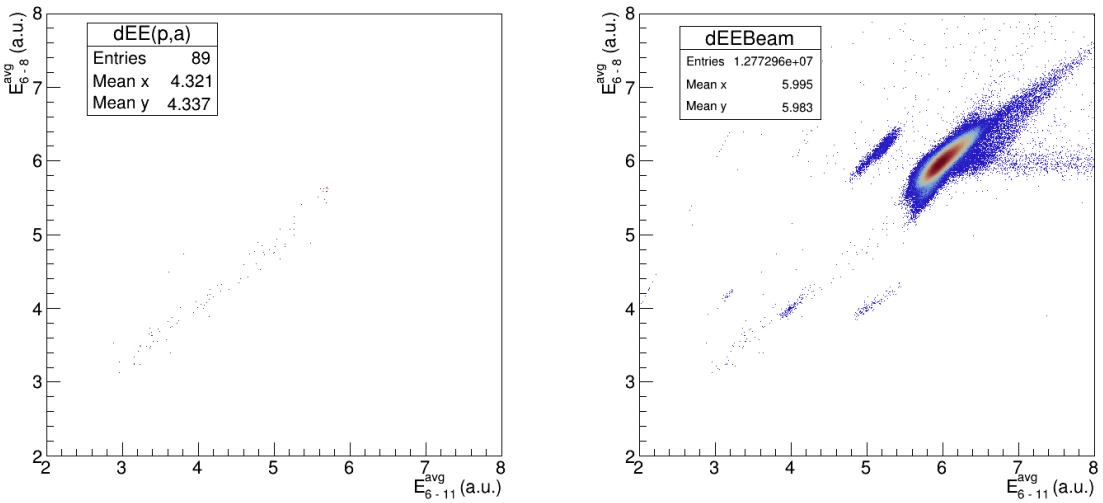

Figure 5.45: Final filtering of strip 5 with strip 3 excluded from the continuity condition. The left panel shows the selected (p, α) events after applying all filtering criteria, while the right panel displays the full filtered dataset. The loss of continuity degrades event separation, increasing background contamination and reducing the clarity of reaction-event identification.

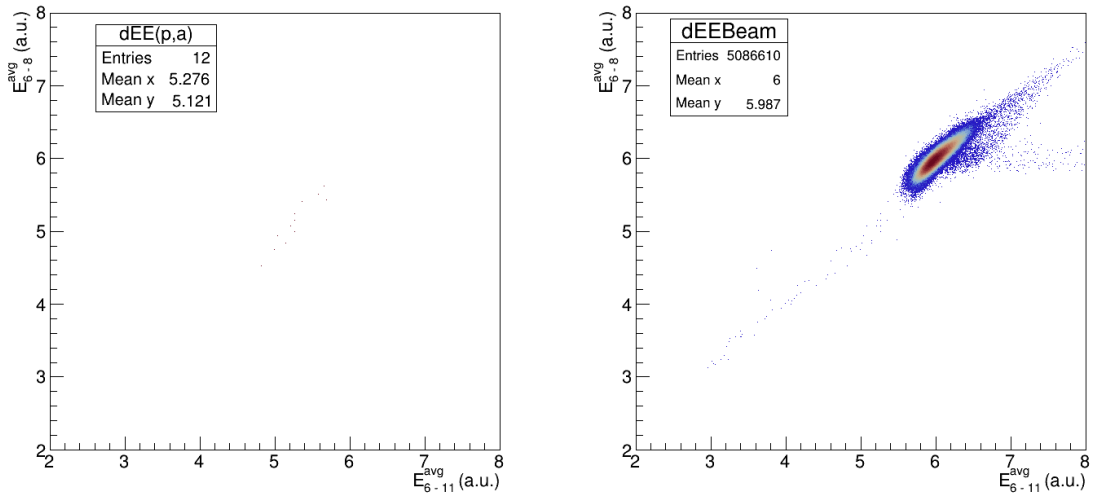

Figure 5.46: Final filtering of strip 6 with strip 3 excluded from the continuity condition. The deterioration in event separation and increased background demonstrate that relaxing the continuity requirement compromises the robustness of reaction-event identification, particularly in low-statistics regions.

Chapter 6

Results and discussion

6.1 New Cross-Section Data for $^{16}\mathrm{O}(\mathrm{p},\alpha)^{13}\mathrm{N}$ Using MUSIC for energies $E_{\mathrm{cm}} = 5.21 - 8.5$ MeV

The new measurement of the $^{16}\mathrm{O}(\mathrm{p},\alpha)^{13}\mathrm{N}$ reaction cross section obtained using the MUSIC detector provides independent experimental constraints on the low-energy behaviour of the reaction in the range $E_{\mathrm{c.m.}} = 5.8$–7.0 MeV. Owing to the relatively large effective energy bins of the MUSIC measurement (0.13 MeV), the present data do not resolve discrepancies between individual narrow-energy datasets. Instead, they constrain the average cross-section behaviour over the low energy range and allow a consistency check against previously published measurements discussed in Section 3.2. The new cross-section of MUSIC measurement was shown in Table 5.6. Although the experiment aimed to measure $E_{\mathrm{cm}} \approx 5.5$ MeV, the very low yield of Strips after strip 4 hindered clear event identification. For (p,α) events of strip 5, some analyses resulted in zero events, so it was not justifiable to average across counts, as the irregular appearance of 1-2 events might be attributed

to beam-related background rather than actual (p, α) reaction events. Additionally, Strip 3 data loss resulted in a 35% reduction in the total detected events, further complicating the statistical analysis of strips with low yields (see Section 5.11). Despite these limitations, an estimated cross-section was initially calculated for Strip 5 , as $0.01^{+0.026}_{-0.005}(mb)$ and represented as an upper limit as seen in Figure 5.36. However, due to the absence of a confirmed (p, α) reaction event and the significant impact of Strip 3 losses, the result of this Strip was ultimately excluded from the final reaction rate calculation.

To ensure a comprehensive calculation of the reaction rate, the cross-section dataset must cover the full astrophysically relevant energy range from the reaction threshold at $E_{\text{cm}} = 5.218$ MeV to $E_{\text{cm}} = 8.5$ MeV. This was achieved by combining multiple complementary data sources:

- MUSIC measurements were used for $E_{\text{cm}} = 5.8 - 7.1$ MeV, providing direct and precise cross-section values.
- At higher energies ($E_{\text{cm}} > 7$ MeV), the previously reported experimental data by McCamis, Nero, Gruhle, and Sajjad after applying appropriate corrections for energy loss in the target and other materials showed considerable agreement (see Figure 3.3). However, the cross-sections from Nero were adopted in this work, as they provide continuous coverage over the full energy range of interest and include details on the energy loss (ΔE) of the proton beam in the target. In contrast, the data from Sajjad and Gruhle consist of discrete points, which may overlook narrow resonances, while the data from McCamis do not extend over the entire energy range.
- For lower energies, where no experimental data were available, an $\mathcal{R}$-matrix calculation was performed (as detailed in Section 4). An uncertainty of 30% was assigned to the extrapolated cross-section values, determined by scaling

the estimated cross-sections to cover the full variations observed in previous McCamis, Nero, Gruhle and Sajjad datasets.

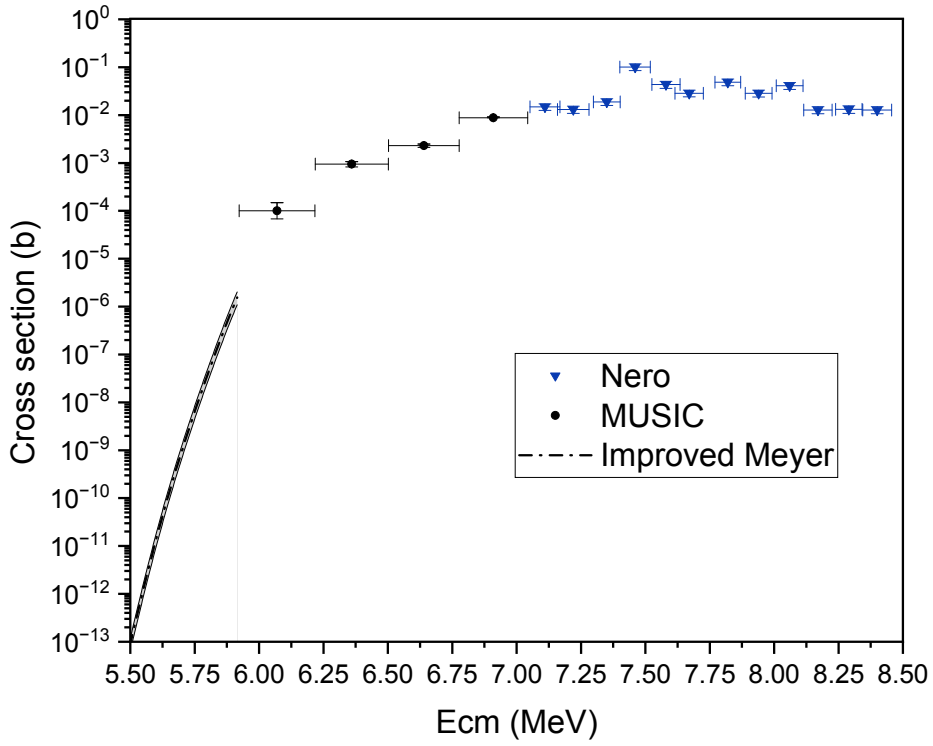

Figure 6.1: Adopted cross-section for the ^{16}O(p, α)^{13}N reaction. The combined dataset covers the full astrophysically relevant energy range ($E_{\mathrm{cm}} = 5.2 - 8.5$ MeV) and incorporates: the low-energy range (5.2–5.8 MeV) as covered by $\mathcal{R}$-matrix extrapolation; the intermediate range (5.8–6.9 MeV) by the MUSIC measurements (present work); and the higher-energy range (6.9–8.5 MeV) by Nero et al. data after correction.

The adopted dataset is shown in Figure 6.1. The new dataset was input to the `EXP2Rate` [84] code to calculate a reaction rate by numerically integrating the cross-section with their associated uncertainties. The $\mathcal{R}$-matrix cross section was computed using the AZURE2 code with an energy step of 0.02 MeV. This energy grid was chosen to ensure that narrow resonances included in the model were properly sampled and not smeared by the grid spacing. The energy spread ΔE of this data was set to 0. The input parameters used in the $\mathcal{R}$-matrix calculations are summarised

in Table 6.1. The experimental data from MUSIC were used as reported in Table 5.6, while the Nero data were adopted from the original publication after applying the necessary corrections, as detailed in Section 3.3.

Table 6.1: Input resonance parameters used in the AZURE2 $\mathcal{R}$-matrix calculation of the $^{16}\mathrm{O}(\mathrm{p},\alpha)^{13}\mathrm{N}$ cross section. The excitation energies (E_x) and spin–parity (J^π) assignments are adopted from the level compilation of Meyer *et al.*. Proton (Γ_p) and alpha (Γ_α) partial widths correspond to the values used as fixed inputs in the calculation. The interference sign was chosen as discussed in Section 4.3.2 .

E_x (MeV)	J^π	Γ_p (keV)	Γ_α (keV)	Interference sign
5.106	$3/2^+$	1.5×10^3	–	(+)
5.820	$3/2^+$	180	6.92×10^{-283}	(+)
6.039	$1/2^-$	28	2.63×10^{-13}	(+)
6.560	$1/2^+$	200	1.88×10^{-3}	(–)
6.701	$5/2^+$	1.6	1.76×10^{-5}	(+)
6.778	$7/2^-$	4.47	3.0×10^{-2}	(–)
7.031	$5/2^-$	3.76	3.59×10^{-2}	(+)
7.361	$3/2^+$	7.20	2.20	(+)
7.483	$1/2^-$	790.36	4.64	(+)
7.551	$1/2^+$	29.98	1.1×10^{-2}	(+)
7.753	$5/2^+$	135	11	(+)
8.073	$3/2^-$	79	14	(+)
8.224	$3/2^-$	636	25	(+)

The reaction rate from current work, including its uncertainty, is presented in Table 6.2, where temperatures related to the oxygen explosive stage of SNIa are around 3-4 GK.

Figure 6.2 illustrates the calculated reaction rate as a ratio to CF88 rate, comparing it to the rate derived from Meyer [7] for the reaction $^{13}\mathrm{N}(\alpha,\mathrm{p})^{16}\mathrm{O}$. Where Meyer rate has been converted to the $^{16}\mathrm{O}(\mathrm{p},\alpha)^{13}\mathrm{N}$ direction using detailed balance formula. Additionally, the rate from the recent IAEA evaluation of the $^{16}\mathrm{O}(\mathrm{p},\alpha)^{13}\mathrm{N}$ cross-section [79] is also included in the comparison.

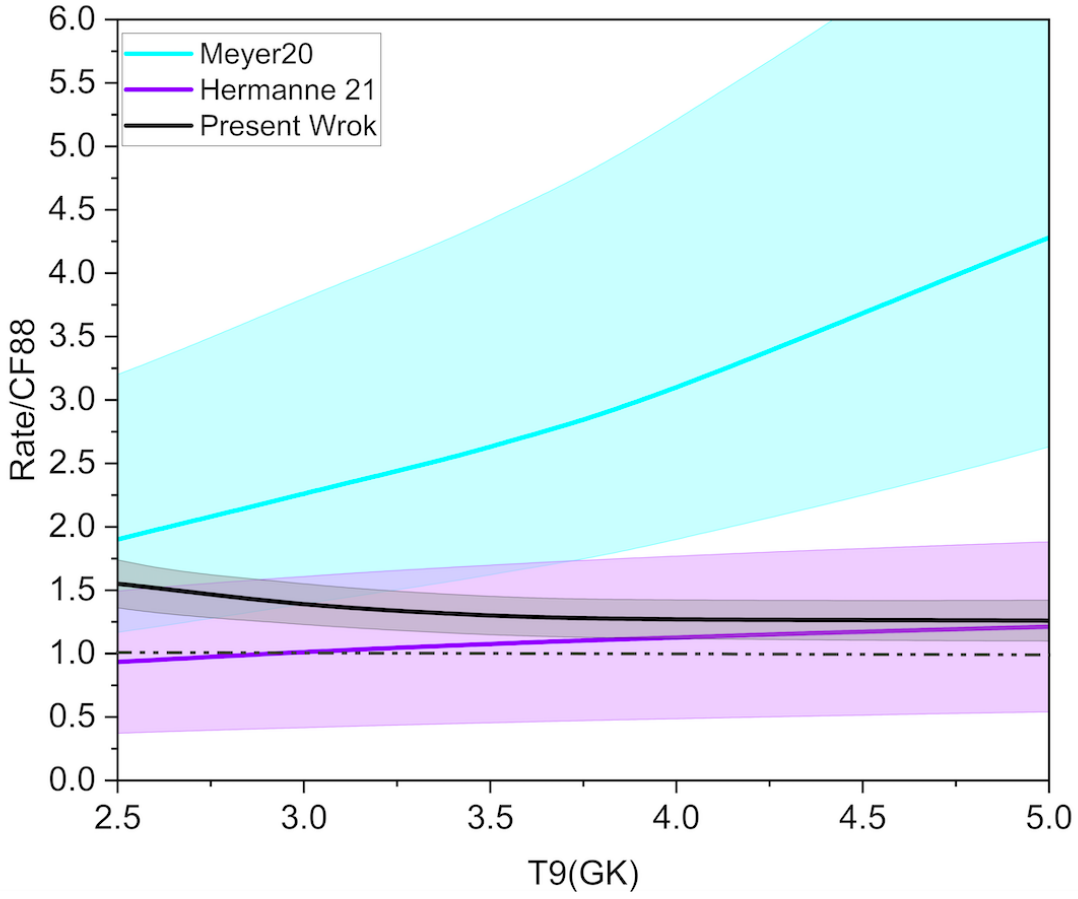

Figure 6.2: The new reaction rate as a ratio to the CF88 rate for temperatures in the range T=2–5 GK, relevant to explosive oxygen burning in Type Ia supernovae. The comparison includes the converted Meyer rate [7] and the IAEA evaluation [79]. The shaded bands represent the uncertainties associated with each dataset.

Table 6.2: Calculated reaction rates of the $^{16}O(p,\alpha)^{13}N$ reaction using the adopted cross-section using the `EXP2Rate` code.

Temperature (GK)	**Low Rate** ($cm^3\,s^{-1}\,mol^{-1}$)	**High Rate** ($cm^3\,s^{-1}\,mol^{-1}$)	**Mean Rate** ($cm^3\,s^{-1}\,mol^{-1}$)
0.3	1.83E-93	3.69E-93	2.60E-93
0.4	8.06E-69	1.72E-68	1.18E-68
0.5	5.44E-54	1.17E-53	7.98E-54
0.6	4.24E-44	9.06E-44	6.20E-44
0.7	5.02E-37	1.05E-36	7.27E-37
0.8	1.04E-31	2.12E-31	1.48E-31
0.9	1.46E-27	2.88E-27	2.05E-27
1.0	3.13E-24	5.94E-24	4.31E-24
1.5	4.24E-14	6.49E-14	5.24E-14
2.0	5.09E-09	1.16E-08	7.68E-09
2.5	1.00E-05	1.28E-05	1.13E-05
3.0	1.43E-03	1.81E-03	1.61E-03
3.5	1.56E-02	2.52E-02	1.96E-02
4.0	7.73E-01	9.84E-01	8.73E-01
4.5	6.39E+00	8.20E+00	7.24E+00
5.0	3.47E+01	4.49E+01	3.95E+01

To calculate the reaction rate of the $^{13}N(\alpha,p)^{16}O$ reaction at temperatures relevant to ^{13}C production in the helium shell of CCSNe, the adopted $^{16}O(p,\alpha)^{13}N$ cross-section was converted into its inverse using the detailed balance formula, as described in Eq. 2.33 (see Section 2.5). Figure 6.3 shows the astrophysical S-factor for the inverse reaction $^{13}N(\alpha,p)^{16}O$, derived from the converted $^{16}O(p,\alpha)^{13}N$ data where the adopted cross-section (S-factor) constructed from Meyer for $E_{cm} = 0 - 0.7$ MeV, MUSIC measurements for $E_{cm} = 0.7 - 1.9$ MeV, and Nero for $E_{cm} = 1.9 - 4.5$ MeV.

Using `EXP2Rate` code the calculated $^{13}N(\alpha,p)^{16}O$ cross-section was input to calculate the reaction rate and its associated uncertainty over the temperature range $T = 0.01$ GK to 2 GK, relevant to CCSNe shock wave condition. The calculated reaction rates are presented in Table 6.3.

The resulting reaction rate is plotted as a ratio to the CF88 rate, as shown in

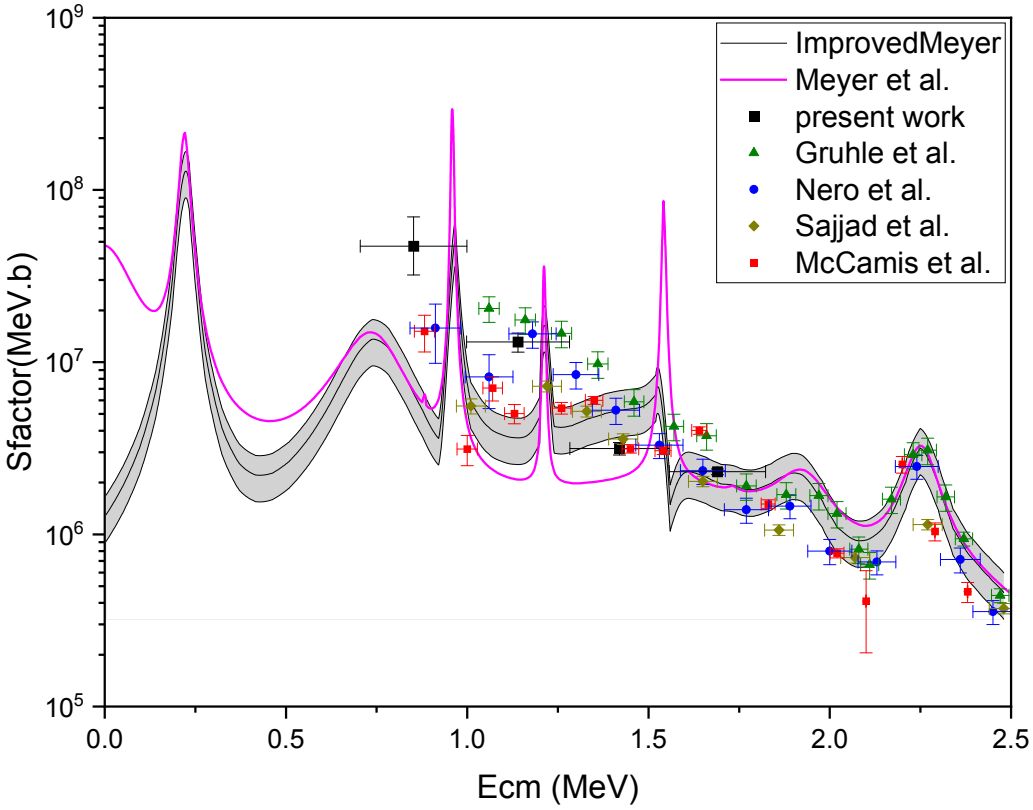

Figure 6.3: Astrophysical S-factor for the inverse reaction $^{13}\mathrm{N}(\alpha,\mathrm{p})^{16}\mathrm{O}$, obtained by converting the adopted $^{16}\mathrm{O}(\mathrm{p},\alpha)^{13}\mathrm{N}$ cross-section using detailed balance. The adopted dataset includes Meyer data for $E_{\mathrm{cm}} = 0 - 0.7$ MeV, MUSIC data for $E_{\mathrm{cm}} = 0.7 - 1.9$ MeV, and Nero data for $E_{\mathrm{cm}} = 1.9 - 4.5$ MeV.

Table 6.3: Calculated reaction rates of the $^{13}\mathrm{N}(\alpha,\mathrm{p})^{16}\mathrm{O}$ reaction using the adopted cross-section using the `EXP2Rate` code.

Temperature (GK)	**Low Rate** ($\mathrm{cm^3\,s^{-1}\,mol^{-1}}$)	**High Rate** ($\mathrm{cm^3\,s^{-1}\,mol^{-1}}$)	**Mean Rate** ($\mathrm{cm^3\,s^{-1}\,mol^{-1}}$)
0.1	9.34E-16	1.80E-15	1.29E-15
0.2	4.32E-10	8.13E-10	5.92E-10
0.3	4.26E-07	8.95E-07	6.18E-07
0.4	1.02E-04	2.89E-04	1.71E-04
0.5	5.37E-03	1.68E-02	9.50E-03
0.6	9.18E-02	3.02E-01	1.66E-01
0.7	7.55E-01	2.60E+00	1.40E+00
0.8	3.83E+00	1.39E+01	7.29E+00
0.9	1.39E+01	5.32E+01	2.72E+01
1.0	4.02E+01	1.60E+02	8.22E+01
1.5	1.22E+03	5.06E+03	2.49E+03
2.0	8.89E+03	3.27E+04	1.70E+04
2.5	3.46E+04	1.11E+05	6.20E+04
3.0	9.37E+04	2.69E+05	1.59E+05

Figure 6.4, compared to the rate from Meyer's work [7].

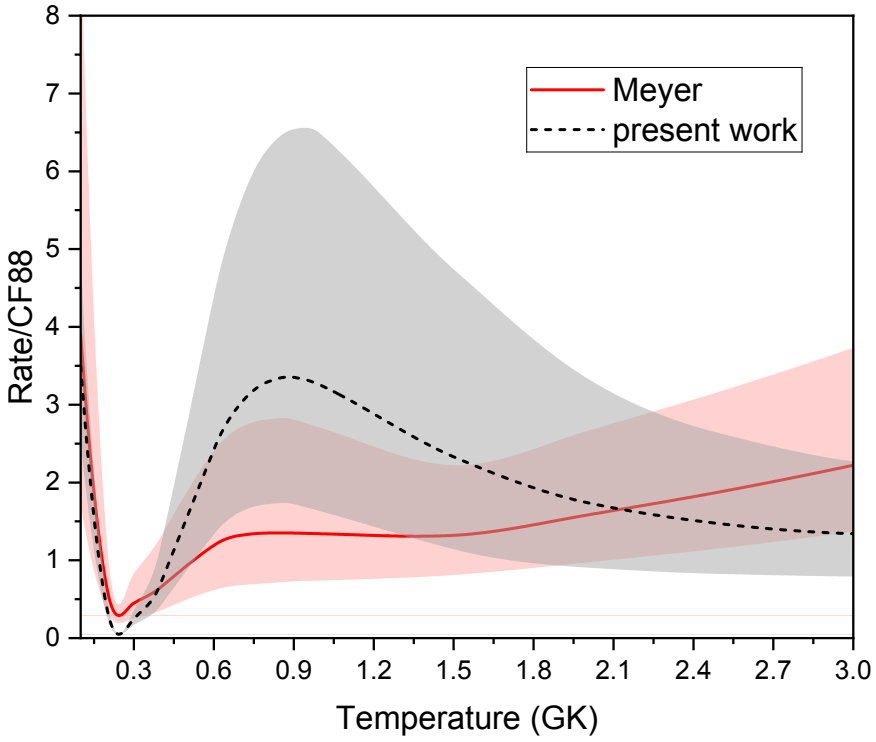

Figure 6.4: Ratio of the newly calculated $^{13}\mathrm{N}(\alpha,\mathrm{p})^{16}\mathrm{O}$ reaction rate at the T=0.1-3GK, compared to the rate derived from Meyer's study [7] as a ratio to CF88. The shaded bands represent the uncertainties associated with each dataset.

6.2 The Impact of the New Rate of $^{16}\mathrm{O}(\mathrm{p},\alpha)^{13}\mathrm{N}$ on Oxygen-Burning Nucleosynthesis in SNe Ia

The adopted $^{16}\mathrm{O}(\mathrm{p},\alpha)^{13}\mathrm{N}$ cross section is constructed from three complementary components: an $\mathcal{R}$-matrix calculation for energies just above the reaction threshold ($E_{\mathrm{c.m.}} = 5.218$–$5.8$ MeV), the present MUSIC experimental data covering $E_{\mathrm{c.m.}} = 5.8$–7.3 MeV, and the corrected Nero dataset for higher energies ($E_{\mathrm{c.m.}} = 7.3$–8.5 MeV). This adopted cross section therefore provides a well-defined input for thermonuclear reaction-rate calculations over the relevant astrophysical energy range. Furthermore, it introduces experimentally based constraints in regions where only phenomenological calculations were previously available. To constrain the role of $^{16}\mathrm{O}(\mathrm{p},\alpha)^{13}\mathrm{N}$ in Type Ia supernovae (SNIa) and its impact on calcium and sulphur (Ca/S) production during oxygen explosive burning in SNIa, the adopted cross-section dataset was used as an input for the `EXP2Rate` code. The resulting reaction rate, with its associated uncertainty for T=2-5 GK, is represented in Table 6.2.

As shown in Figure 6.2, the derived reaction rate at temperatures relevant to SNIa is much lower than the rate represented by Meyer (2020). This discrepancy is expected, as the Meyer rate at temperatures above 1 GK was calculated by normalising the $^{13}\mathrm{N}(\alpha,\mathrm{p})^{16}\mathrm{O}$ rate from the STARLIB database. The STARLIB rate is based on the (H-F) statistical model, which tends to overestimate reaction rates in low-density systems such as the $^{16}\mathrm{O}(\mathrm{p},\alpha)^{13}\mathrm{N}$ and $^{17}\mathrm{F}$ compound nucleus case. Compared with the Padé fit recommended by Hermanne et al. (2021) [79], the present rate shows a noticeably different trend at lower temperatures. This divergence originates from differences in the cross-section datasets as illustrated in Figure 5.36. At $E_{\mathrm{cm}} \approx 6.0 - 6.5$ MeV, the IAEA evaluation showed a lower cross-section, which led to a lower reaction rate at T<3.4 GK. Furthermore, the wide uncertainty band associated with the Padé fit reflects the reported 65% uncertainty in the cross section

within that energy region.

The new rate generally agrees with Hermanne evaluations within uncertainties; however, it offers a significantly tighter constraint. This improvement is primarily due to the incorporation of MUSIC cross-section data, which enhances the reliability of the rate of $^{16}\mathrm{O}(\mathrm{p},\alpha)^{13}\mathrm{N}$ at the temperatures of 3-4GK achieved during the oxygen-burning stage in SNIa.

While earlier measurements had already indicated that an increase by a factor of seven above the CF88 rate as proposed by Bravo [5] is unsupported, discrepancies regarding the suggested upper limit were identified due to the broad variation in earlier reaction rate evaluations, as illustrated in Figure 3.4. The reaction rate derived in the present work has an uncertainty of approximately 40% at low temperatures, decreasing to about 14% at higher temperatures. This represents a tighter constraint than those reported in the evaluations of Meyer [7] and Hermanne [79] (Figure 6.2). Within the current uncertainties, enhancements of the $^{16}\mathrm{O}(\mathrm{p},\alpha)^{13}\mathrm{N}$ rate relative to CF88 larger than a factor of ~ 1.5 are disfavoured.

Thus, the new results demonstrate that the $^{16}\mathrm{O}(\mathrm{p},\alpha)^{13}\mathrm{N}$ reaction rate alone is insufficient to explain the variations in Ca/S abundances observed across different metallicities in SNIa remnants, as suggested by Bravo. Therefore, an alternative mechanism must influence the $^{16}\mathrm{O}$ abundance, subsequently affecting Ca/S production. The previously hypothesised reduction in the $^{16}\mathrm{O} + {}^{12}\mathrm{C}$ fusion rate remains a possible candidate to explain the variation in Ca/S ratios. However, current experimental data for the $^{16}\mathrm{O} + {}^{12}\mathrm{C}$ reaction remains insufficient to conclusively support or refuse this suggestion, emphasising the necessity for more precise experimental constraints on this rate and the need for improved stellar models.

6.3 The Impact of the New Rate of $^{13}\mathrm{N}(\alpha,\mathrm{p})^{16}\mathrm{O}$ on CCSN shock wave Nucleosynthesis

During the CCSN shock wave stage, the nucleosynthesis of ^{13}C depends critically on the $^{13}\mathrm{N}(\alpha,\mathrm{p})^{16}\mathrm{O}$ reaction rate at temperatures of 0.1–2 GK. For this temperature range, the Gamow window is located between $E_{\mathrm{cm}} = 0.3 - 1.4$ MeV.

Due to the short half-life of the ^{13}N nucleus ($T_{1/2} = 9.97$ minutes), direct experimental measurements of the $^{13}\mathrm{N}(\alpha,\mathrm{p})^{16}\mathrm{O}$ cross section were relatively challenging. As a result, current data come from the inverse reaction $^{16}\mathrm{O}(\mathrm{p},\alpha)^{13}\mathrm{N}$. In this context, the new measurements from MUSIC provide the most up to date experimental information for cross sections at energies relevant to the role of $^{13}\mathrm{N}(\alpha,\mathrm{p})^{16}\mathrm{O}$ in CCSN shock wave nucleosynthesis.

The previous measurements by Nero, Gruhle, McCamis, and Sajjad encountered significant challenges particularly at low energies due to the strong Coulomb barrier and background activity of other β-emitters. The current MUSIC experimental data significantly improves the experimental constraints in the critical energy range of $E_{\mathrm{cm}}^{^{13}\mathrm{N}+\alpha}$ =0.6–1.8 MeV. This range covers a substantial portion of the Gamow window (G.W for T=0.4-1GK is within $E_{\mathrm{cm}}^{^{13}\mathrm{N}+\alpha}$ = 0.4-1.4 MeV), offering a robust experimental basis for recalculating the $^{13}\mathrm{N}(\alpha,\mathrm{p})^{16}\mathrm{O}$ rate at low temperatures.

All data have been converted to the $^{13}\mathrm{N}(\alpha,\mathrm{p})^{16}\mathrm{O}$ direction, as shown in Figure 6.1. The adopted cross-section used for calculating the reaction rate with the `EXP2Rate` code consists of the $\mathcal{R}$-matrix cross-section, MUSIC experimental measurements, and corrected Nero data as in $^{16}\mathrm{O}(\mathrm{p},\alpha)^{13}\mathrm{N}$ case.

The reaction rate resulting from the present work is shown in Figure 6.4 as

a ratio to the CF88 rate and compared to the previous rate of Meyer [7]. The updated rate reveals significant deviations from Meyer's estimation, particularly in the temperature range $T = 0.4 - 1.5$ GK, where the new rate is notably higher.

A similar trend was reported by Jayatissa *et al.* [117], who replaced the Meyer cross section above 0.9 MeV with an earlier IAEA evaluation based on the Padé fit of Takács *et al.* [118]. The approach adopted by Jayatissa *et al.* has two principal limitations in this temperature region. First, the Padé fit employed by Jayatissa *et al.* is based on an earlier IAEA evaluation derived from the work of Takács *et al.*, for which no associated uncertainties were reported. As a result, an uncertainty had to be assumed, rather than being constrained by the underlying experimental data. Second, Jayatissa *et al.* assigned an arbitrary uncertainty of 20% to the Meyer cross section. This treatment does not reflect the true uncertainty associated with the Meyer evaluation, which is dominated by uncertainties in the adopted resonance parameters and by the neglect of interference effects on the cross section.

The variation between Meyer (2020) and the present rate mainly stems from differences in methodology. Meyer's rate was derived entirely from the nuclear structure of excited states in ^{17}F; however, these states have since been shown to be highly uncertain and inconsistent with experimental observations (see Section 4). In contrast, the present rate is based on integrated cross-section data with uncertainties derived from experimental measurements.

Moreover, the presence of multiple broad resonances in this energy range makes interference effects significant. Neglecting such interference in earlier calculations in Meyer's resulted in a lower cross-section that is inconsistent with experimental data at $E_{\mathrm{cm}}^{^{13}\mathrm{N}+\alpha} = 0.5$-$1.8$ MeV see Figure 6.3. Moreover, the present measurement shows no indication of strong, narrow resonances at $E_{\mathrm{cm}}^{^{13}\mathrm{N}+\alpha} \approx 1.0 - 1.6$ MeV yet still yields a higher rate. This suggests that the $^{13}\mathrm{N}(\alpha,\mathrm{p})^{16}\mathrm{O}$ rate is dominated by

broad resonances and their interactions.

The higher reaction rate for $^{13}\mathrm{N}(\alpha,\mathrm{p})^{16}\mathrm{O}$, as calculated by the new MUSIC measurements, implies enhanced ^{13}N destruction via alpha capture, which could significantly alter the subsequent ^{13}C production via beta decay. However, due to existing uncertainties in the reaction rate at $T = 0.4$–0.7 GK, it remains difficult to precisely quantify the impact of $^{13}\mathrm{N}(\alpha,\mathrm{p})^{16}\mathrm{O}$ on ^{13}C nucleosynthesis.

While Meyer's estimation with tighter constraints yielded a factor of 50 uncertainty in ^{13}C production, the current rate might imply even greater uncertainty. This is partly due to experimental challenges at lower energies, including the strong Coulomb barrier, low yields, and the loss of strip 3 events in the MUSIC detector (see Section 5.10).

These results underscore the need for further experimental data to reduce the uncertainties in the $^{13}\mathrm{N}(\alpha,\mathrm{p})^{16}\mathrm{O}$ rate. Future efforts should focus on improved low-energy measurements and refined spectroscopy of ^{17}F states to better constrain this critical reaction in CCSN nucleosynthesis modelling.

6.4 Beyond the Ground State: Assessing the Role of Thermally Excited States in $^{16}\mathrm{O}(\mathrm{p},\alpha)^{13}\mathrm{N}$ Reaction Rate Under Oxygen Explosive Conditions

The reaction rate presented in this study was calculated under experimental conditions, where the ^{16}O target nucleus remained in its ground state. However, as

discussed in Section 2.4.5, this assumption may not fully reflect the stellar rate at the relevant temperatures of 3–4 GK. If the temperature of $T = 3.5$ GK is considered, the excited states of the target are expected to have a non-negligible population according to the Maxwell-Boltzmann distribution. However, in the case of the ^{16}O target nucleus, the first excited state lies at an energy of 6.049 MeV, which is sufficiently high for its population to remain strongly suppressed by the Boltzmann factor. Consequently, even at $T = 3.5$ GK, the partition function G remains effectively unity, indicating that the ground state continues to dominate the overall rate contribution.

Table 6.4 illustrates the effect of Maxwell-Boltzmann suppression on the population of excited states in ^{16}O and lists the calculated state populations at a temperature of $T = 3.5$ GK. The population of each excited state was computed assuming thermodynamic equilibrium and a non-degenerate plasma, such that the relative population of state μ follows a Boltzmann distribution. Specifically, the fractional population was calculated according to

$$P_{i\mu} = \frac{g_{i\mu}\, \exp(-E_{i\mu}/kT)}{G_i}, \tag{6.1}$$

where $g_{i\mu} = 2J_\mu + 1$ is the statistical weight of the state, $E_{i\mu}$ is its excitation energy, and G_i is the nuclear partition function including the ground state. This formalism follows the treatment described by Iliadis [29]. At $T = 3.5$ GK, the ground state population is 8.06×10^7, exceeding the population of the most strongly populated excited state ($E_x = 6.049$ MeV) by more than eight orders of magnitude. All excited states above 6 MeV contribute negligibly to the total population, confirming that the thermal population is effectively concentrated in the ground state at this temperature.

Nevertheless, a study by P. Mohr et al. [43] highlighted an important effect that

Table 6.4: Boltzmann suppression factor and thermal population of ^{16}O states up to 9.844 MeV at $T = 3.5$ GK.

State (MeV)	Spin J	Boltzmann Suppression $e^{-E/kT}$	Population
g.s	0	1.00×10^{0}	8.06×10^{7}
6.049	0	1.95×10^{-9}	1.57×10^{-1}
6.129	3	1.49×10^{-9}	8.43×10^{-2}
6.917	2	1.10×10^{-10}	4.41×10^{-2}
7.117	1	5.65×10^{-11}	1.37×10^{-2}
8.065	2	1.68×10^{-13}	6.76×10^{-5}
9.585	1	1.58×10^{-14}	3.81×10^{-6}
9.844	2	6.76×10^{-15}	2.69×10^{-6}

arises from the combination of the high negative Q-value and the position of the Gamow window within the excitation states of the resulting compound nucleus. As discussed in Section 2.4.4, the endothermic nature of the ^{16}O(p, α)^{13}N reaction shifts the Gamow window to higher excitation energies in ^{17}F. As a result, the incident protons must overcome both the Q-value and have high enough energy to populate the excitation state of ^{17}F within the Gamow window.

To illustrate this, consider the ^{17}F state at $E_x^{^{17}\mathrm{F}} = 8.035$ MeV, which lies within the Gamow window. For protons on the ^{16}O ground state , as shown in Figure 6.5, the required proton energy is $E_p(cm) = 7.435$ MeV, where $E_x^{^{17}\mathrm{F}} = E_p(cm) + S_p$, and $S_p = 0.60027$ MeV. So although the ground state of ^{16}O benefits from a dominant thermal population, this advantage is offset by the fact that the required proton energies fall within the exponentially suppressed high-energy tail of the Maxwell-Boltzmann distribution.

In contrast, protons on excited states of ^{16}O requires lower effective projectile energies, given by $\Delta E = E_x^{^{17}\mathrm{F}} - E_x^{^{16}\mathrm{O}}$. For example, the same ^{17}F state at $E_x = 8.035$ MeV can be populated via the second excited state of ^{16}O, at 6.129 MeV, with a proton energy of only $E_p = 1.306$ MeV.This is significantly lower than the

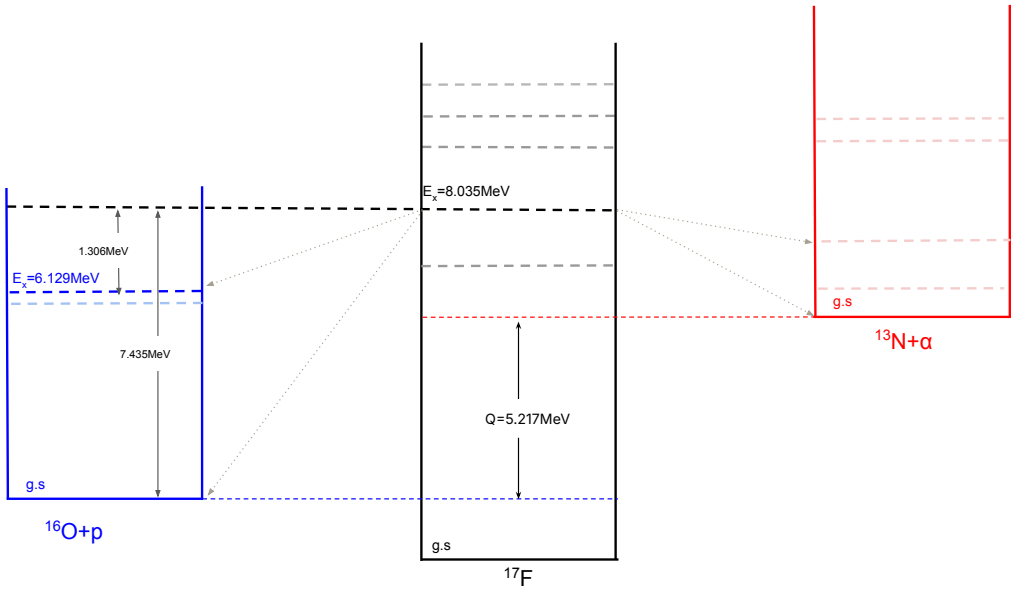

Figure 6.5: Schematic illustration of proton-induced population of states in ^{17}F from various initial states in ^{16}O. The figure highlights how the proton projectile energy required to reach resonances in ^{17}F varies depending on the excitation energy of the target state.

7.435 MeV required when starting from the ground state. Therefore, excited states that lie closer in energy to the levels populated in ^{17}F experience less Maxwell-Boltzmann suppression. This effect can be quantified by the energy difference ΔE, which represents the effective proton energy required to populate a given state in ^{17}F from a specific excited state of ^{16}O, as follows:

$$\text{Suppression} \sim \exp\left[-\frac{\Delta E}{k_{\mathrm{B}}T}\right], \quad \Delta E = E_x^{^{17}\mathrm{F}} - E_x^{^{16}\mathrm{O}}. \tag{6.2}$$

Table 6.5 summarises these suppression factors for different excited states of ^{16}O, using the $E_x = 8.035$ MeV state in ^{17}F as a representative example. The results show that, due to low required energy ΔE, excited states are less suppressed and could play a more substantial role in the reaction rate than previously assumed.

In this case, the potential contribution from thermally excited target states is

Table 6.5: Suppression factors and thermal populations for excited states of ^{16}O at $T = 3.5$ GK considering the effective proton energy ΔE, calculated relative to the $E_x = 8.035$ MeV state in ^{17}F as in Eq. 6.2 .

ΔE (MeV)	Spin J	MB Suppression $e^{-\Delta E/kT}$	Population
7.435	0	1.97×10^{-11}	1.21×10^{-10}
1.386	0	1.01×10^{-2}	4.34×10^{-1}
1.306	3	1.32×10^{-2}	5.66×10^{-1}

expected to be strongly influenced by the branching ratios of the p_1 channel in the compound nucleus of ^{17}F.

Although the p_1 channel opens at approximately E_{cm} =6 MeV, its width was previously considered negligible in the range E_{cm} = 6-7 MeV, as noted by Salisbury *et al.* [89, 88]. However, the partial widths reported by Dangle *et al.* [77] provide values for the p_1 decay channel at higher excitation energies. Using these values, the branching ratios for p_0 and p_1 were calculated for three key states in ^{17}F at $E_x = 7.753$, 8.035, and 8.224 MeV, as shown in Table 6.6.

Table 6.6: Branching ratios of p_0, p_1, and α decay channels relative to the total width Γ_{tot} for selected excited states of ^{17}F.

E_x (MeV)	p_0/Γ_{tot} (%)	p_1/Γ_{tot} (%)	α/Γ_{tot} (%)
7.753	75%	19%	6%
8.035	76%	11%	13%
8.224	90%	6%	4%

Based on these branching ratios, it would be expected to see a noticeable enhancement in the reaction rate upon inclusion of the p_1 channel particularly in the case of the 7.753 MeV resonance, where p_1 constitutes nearly 20% of the total decay width.

6.4.1 Hauser-Feshbach Calculations

To examine the potential impact of thermally excited states on the reaction rate, the rate calculations were performed using the TALYS nuclear reaction code [39]. These simulations allowed for a comparison between rates computed using only the ground state of ^{16}O and the low-lying excited states of 6.049 and 6.129 MeV.

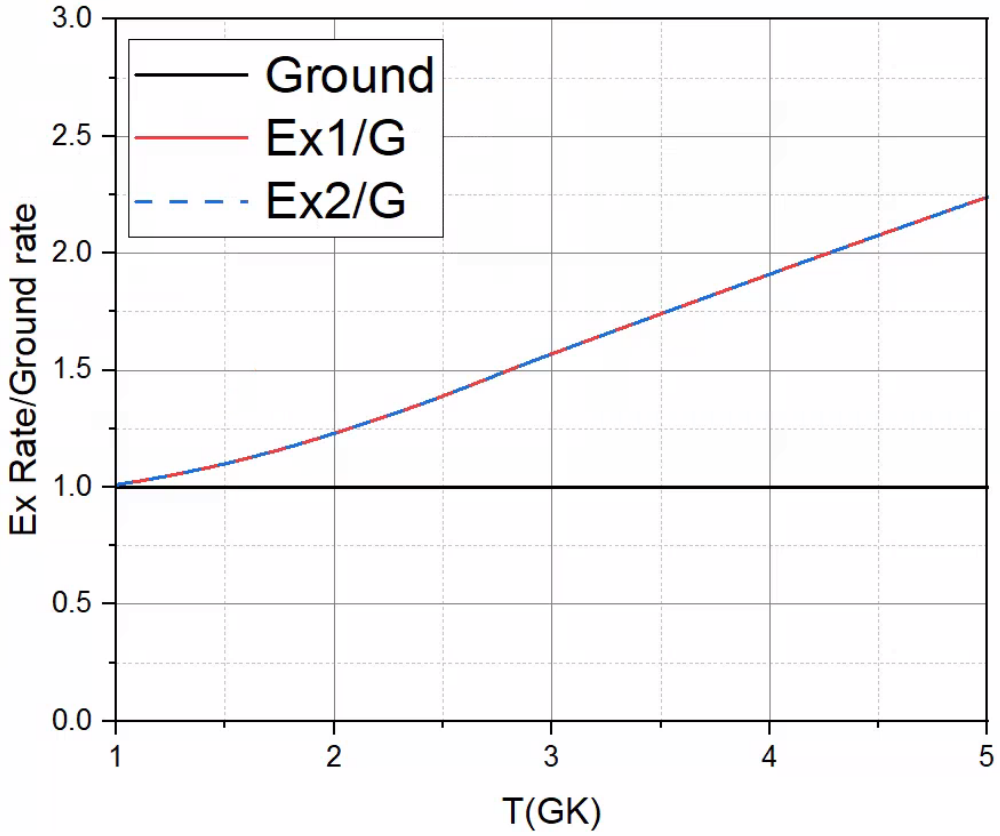

Figure 6.6: Hauser-Feshbach estimation of the ^{16}O(p, α)^{13}N reaction rate using TALYS, illustrating the enhancement due to thermally populated excited states of the ^{16}O target nucleus. The rate is shown as a ratio to the TALYS calculation assuming the ground state only.

The results indicate that excited states can enhance the total reaction rate by up to a factor of two compared to calculations that assume only the ground state.

6.4.2 The Limited Impact of the Proton Channel on the Reaction Rate

While both the branching ratio comparison (see Table 6.6) and TALYS-based Hauser-Feshbach calculations Section 6.4.1 suggest a potentially significant enhancement of the $^{16}\mathrm{O}(\mathrm{p},\alpha)^{13}\mathrm{N}$ reaction rate due to the p_1 channel, it is essential to evaluate this hypothesis quantitatively using the best available spectroscopic information on $^{17}\mathrm{F}$ states.

To achieve this, cross-section calculations (represented as the S-factor for better visualisation of the resonances) for $^{13}\mathrm{N}(\alpha,\mathrm{p})^{16}\mathrm{O}$ were performed with and without the inclusion of the p_1 partial width using AZURE2 code. The comparison focused on key resonances at $E_x = 7.753$, 8.035, and 8.224 MeV. Despite branching ratios for p_1 as high as 20% in some states, the results did not show any significant change in the S-factor upon inclusion of the p_1 channel as seen in Figure 6.7. Consistent with this behaviour, the reaction rate calculations performed within AZURE2 show that inclusion of the p_1 channel leads to only a modest enhancement relative to the p_0-only rate. The maximum increase does not exceed approximately 8% at temperatures above 4.5 GK, as shown in Figure 6.8. This result contrasts with the factor-of-two enhancement predicted by TALYS calculations. The difference arises because TALYS employs a statistical-model treatment that averages over resonance properties, an approach that is not appropriate in the present case where the reaction proceeds through a low density of discrete resonances. Consequently, the statistical-model calculation tends to overestimate the contribution from excited state channels compared to the $\mathcal{R}$-matrix results.

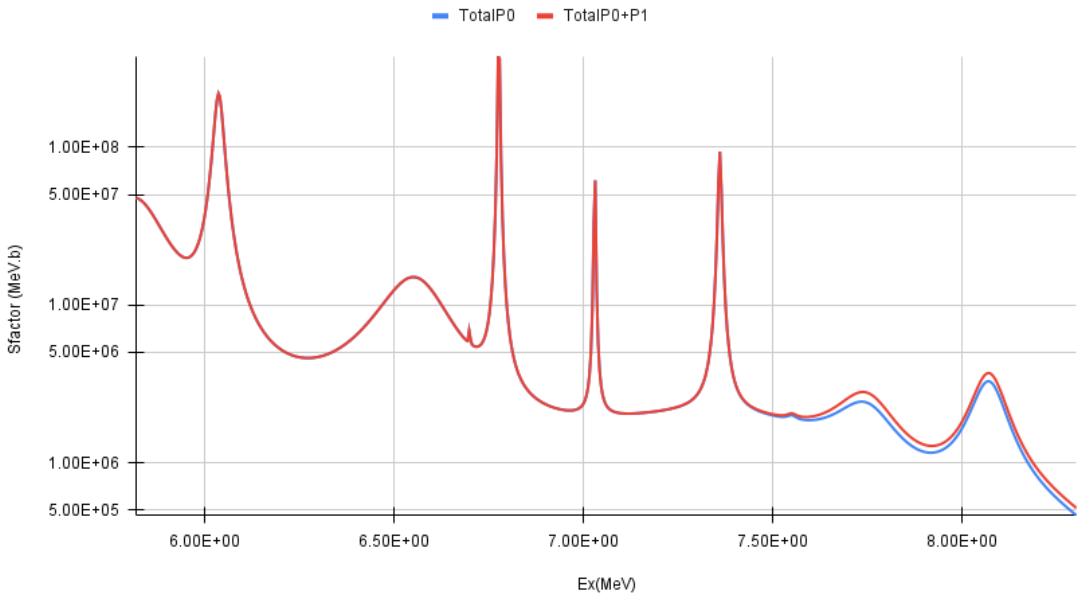

Figure 6.7: Calculated astrophysical S-factor for the $^{13}\mathrm{N}(\alpha,\mathrm{p})^{16}\mathrm{O}$ reaction using AZURE2, comparing fits that include only the p_0 channel (blue) and include both p_0 and p_1 (red). The results show no significant change in the S-factor across the energy range E_x = 6–8 MeV, even for resonances where the p_1 branching ratio reaches 20%.

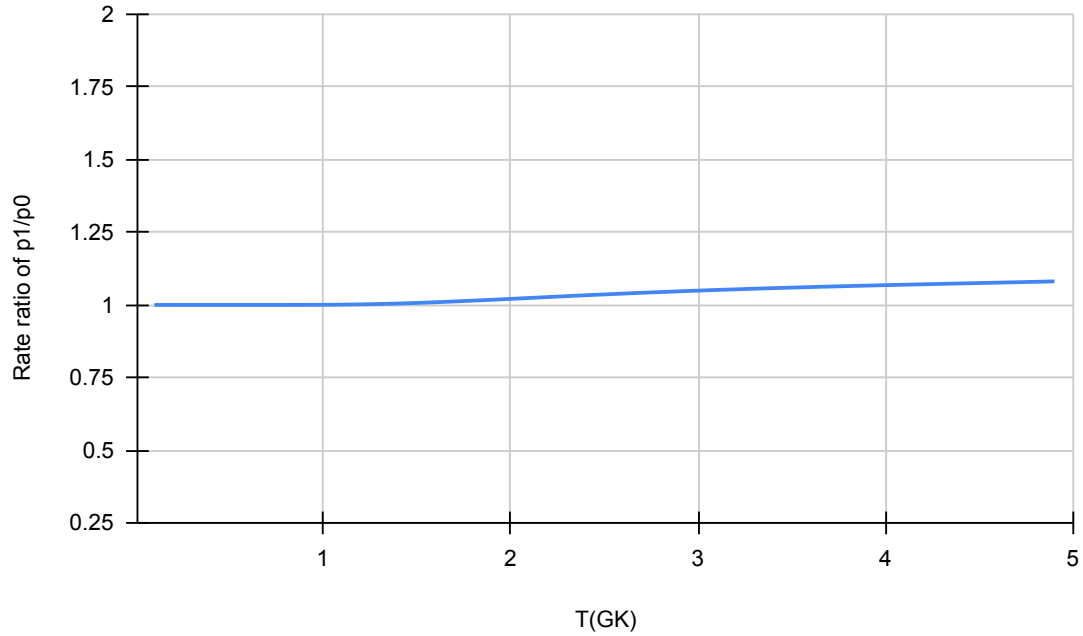

Figure 6.8: Comparison of the $^{13}\mathrm{N}(\alpha,\mathrm{p})^{16}\mathrm{O}$ reaction rate calculated using only the p_0 channel versus both $\mathrm{p}_0 + p_1$ channels. The inclusion of the p_1 channel results in a slight enhancement of the rate, reaching a maximum of approximately 8% at temperatures above 4.5 GK.

To understand this unexpected result, it is important to consider the resonance strength expression. For a resonance of spin J, the strength is given by:

$$\omega\gamma = \frac{2J+1}{(2J_p+1)(2J_t+1)} \cdot \frac{\Gamma_\alpha \Gamma_p}{\Gamma_\alpha + \Gamma_p}. \tag{6.3}$$

As discussed in Section 4, the ^{17}F states above the α-threshold are typically dominated by proton emission, such that $\Gamma_{\text{tot}} \approx \Gamma_p$. In this limit, the proton widths cancel between the numerator and denominator, and the resonance strength becomes approximately:

$$\omega\gamma \propto \Gamma_\alpha. \tag{6.4}$$

To express this more explicitly, for the two channel reaction of (p,α) that each channel is composed of its partial branches, such that: ($\Gamma\alpha = \Gamma\alpha_0 + \Gamma\alpha_1 + ...$) and ($\Gamma p = \Gamma p_0 + \Gamma p_1 + ...$).

Table 6.7 compares the resulting resonance strengths when the total proton width Γp includes only (p_0) decay versus when both proton branches (p_0,p_1) are included, using Eq. (6.3) for resonance strength.

Table 6.7: Effect of Including p_1 on the Resonance Strength $\omega\gamma$, where $\Gamma p = \Gamma p_0 + \Gamma p_1$

$\mathbf{E}_x$ (keV)	$\boldsymbol{\omega\gamma}$ when $p_1 = 0$	$\boldsymbol{\omega\gamma}$ when $p_1 = p_1$	Enhancement (%)
7753	10.2	10.3	1.54%
8035	35.7	36.3	1.87%
8224	48.1	48.2	0.25%

This minimal enhancement in ($\omega\gamma$) is consistent with the behaviour observed in Figure 6.7, and reinforces the conclusion that while p_1 contributes to the total width, it does not influence the resonance strength when summed consistently within Γp.

In other words, although p_1 separately can be seen to have a considerable branch-

ing ratio as shown in Table 6.6, its inclusion does not modify the relative balance between the partial decay width and the total width. When the p_1 contribution is added, it appears consistently in both the numerator and denominator of Eq. (6.3), and therefore cancels in the ratio. Consequently, the resonance strength remains governed by the α-particle width as shown before.

The above analysis confirms that, under the condition of $\Gamma_\alpha \ll \Gamma_p$, the α channel directly determines the resonance strength and, therefore, the reaction rate. In this case, any additional contribution to the α channel could significantly alter the rate. If the α_1 decay occurs, it could influence the reaction rate significantly. However, the α_1 channel opens only at $E_{\mathrm{cm}} = 7.53$ MeV, and to date, no experimental partial widths for this channel are available in the literature.

In the study by Nero *et al.* [72], the contribution of the α_1 channel was theoretically assessed using the evaporation model of Michaud and Fowler [119]. This model estimates the relative importance of the α_0 and α_1 branches, corresponding to the population of the ground and first excited states of ^{13}N, respectively. The results indicate that the α_1 contribution is negligible at energies below $E_{\mathrm{cm}} = 9$ MeV, primarily due to suppression by the Coulomb barrier. Since the relevant energy range for this reaction lies below 9 MeV, the α_1 contribution is concluded to be insignificant. These findings reinforce that cross-section measurement of the ground state for $^{16}\mathrm{O}(\mathrm{p},\alpha)^{13}\mathrm{N}$ reaction adequately represents the full stellar reaction rate in this case.

Overall, these results confirm that contributions through excited states of both the ^{16}O target and the ^{13}N residual nucleus have a minimal impact on the reaction rate of $^{16}\mathrm{O}(\mathrm{p},\alpha)^{13}\mathrm{N}$ Additionally, they highlight that TALYS-based Hauser-Feshbach predictions, which rely on averaging over resonances of compound nuclei, become less valid in nuclei such as ^{17}F. This is particularly evident in cases where

the resonance density above $E_x = 7.7$ MeV is low. Therefore, TALYS predictions in this energy range should be interpreted with caution.

6.5 Detailed Balance and Time Reversibility in $^{16}\mathrm{O}(\mathrm{p},\alpha)^{13}\mathrm{N}$ and $^{13}\mathrm{N}(\alpha,\mathrm{p})^{16}\mathrm{O}$ at Low Temperatures: From Cross Sections to Reaction Rates

The main objective of this study was to determine updated thermonuclear reaction rates for both $^{16}\mathrm{O}(\mathrm{p},\alpha)^{13}\mathrm{N}$ and $^{13}\mathrm{N}(\alpha,\mathrm{p})^{16}\mathrm{O}$, at temperatures relevant to two distinct astrophysical environments: the oxygen-burning phase in Type Ia supernovae (SNIa) and hydrogen ignition in the helium shell of core-collapse supernovae (CCSN), respectively. The relevant temperature range for this work spanned 0.4–5 GK.

The initial approach involved calculating the rate using $^{16}\mathrm{O}(\mathrm{p},\alpha)^{13}\mathrm{N}$ cross-section data from above the reaction threshold up to $E_{\mathrm{cm}} = 9$ MeV, which is appropriately covering the high temperatures encountered in SNIa oxygen explosive scenarios. This rate was then inverted to obtain the $^{13}\mathrm{N}(\alpha,\mathrm{p})^{16}\mathrm{O}$ rate, which is more important at lower temperatures, by applying the formula of detailed balance.

In principle, the reaction rates of $^{16}\mathrm{O}(\mathrm{p},\alpha)^{13}\mathrm{N}$ and $^{13}\mathrm{N}(\alpha,\mathrm{p})^{16}\mathrm{O}$ should satisfy time reversal symmetry. That is, regardless of which direction the rate is initially calculated in, the reversed rate should be obtained by applying a factor that depends only on the Q-value and the properties of the particles involved, as clear from Eq. 2.35. Therefore, both forward and inverse rates are expected to exhibit consistent temperature-dependent behaviour after transformation.

However, when the reaction rate was calculated from the new experimental $^{16}\mathrm{O}(\mathrm{p},\alpha)^{13}\mathrm{N}$ cross-section data using the `Exp2Rate` code, an unexpected result emerged. At low temperatures ($T \approx 0.4$–2 GK), the calculated rate significantly exceeded the corresponding rate from the rate by Meyer*et al.* [7], even though the low-energy part of the cross-section data was adopted directly from the same Meyer dataset. This discrepancy becomes more evident in Figure 6.9, which compares the new calculated rates for both $^{16}\mathrm{O}(\mathrm{p},\alpha)^{13}\mathrm{N}$ and $^{13}\mathrm{N}(\alpha,\mathrm{p})^{16}\mathrm{O}$ as a ratio to their corresponding rates from CF88 [64]. In this figure, the newly obtained cross section of $^{16}\mathrm{O}(\mathrm{p},\alpha)^{13}\mathrm{N}$ was inverted to $^{13}\mathrm{N}(\alpha,\mathrm{p})^{16}\mathrm{O}$ cross section, then both cross sections were fed to `Exp2Rate` to calculate a rate with an uncertainty.

To investigate this unexpected behaviour and verify that it was not due to an error in the conversion from $^{16}\mathrm{O}(\mathrm{p},\alpha)^{13}\mathrm{N}$ to $^{13}\mathrm{N}(\alpha,\mathrm{p})^{16}\mathrm{O}$ cross section, an independent test was performed using the AZURE2 code. In this test, cross sections for both $^{16}\mathrm{O}(\mathrm{p},\alpha)^{13}\mathrm{N}$ and $^{13}\mathrm{N}(\alpha,\mathrm{p})^{16}\mathrm{O}$ were generated using only the level parameters reported by Meyer et al. [7], without using any experimental data as input.

Both theoretical cross sections were then used as input to the `Exp2Rate` code to calculate the corresponding reaction rates. The rate obtained from the $^{16}\mathrm{O}(\mathrm{p},\alpha)^{13}\mathrm{N}$ cross section was converted to the inverse direction using the detailed balance formalism, and compared to the $^{13}\mathrm{N}(\alpha,\mathrm{p})^{16}\mathrm{O}$ rate that was calculated directly from the $^{13}\mathrm{N}(\alpha,\mathrm{p})^{16}\mathrm{O}$ cross section.

As shown in Figure 6.10, the $^{13}\mathrm{N}(\alpha,\mathrm{p})^{16}\mathrm{O}$ rate derived from the $^{16}\mathrm{O}(\mathrm{p},\alpha)^{13}\mathrm{N}$ cross section (referred to here as the reversed-$^{16}\mathrm{O}(\mathrm{p},\alpha)^{13}\mathrm{N}$ rate) remains systematically higher than the directly calculated $^{13}\mathrm{N}(\alpha,\mathrm{p})^{16}\mathrm{O}$ rate at low temperatures ($T \approx 0.4$–2 GK). The discrepancy is particularly significant between $T = 0.6$ and 1 GK, where the reversed-$^{16}\mathrm{O}(\mathrm{p},\alpha)^{13}\mathrm{N}$ rate is up to a factor of three larger.

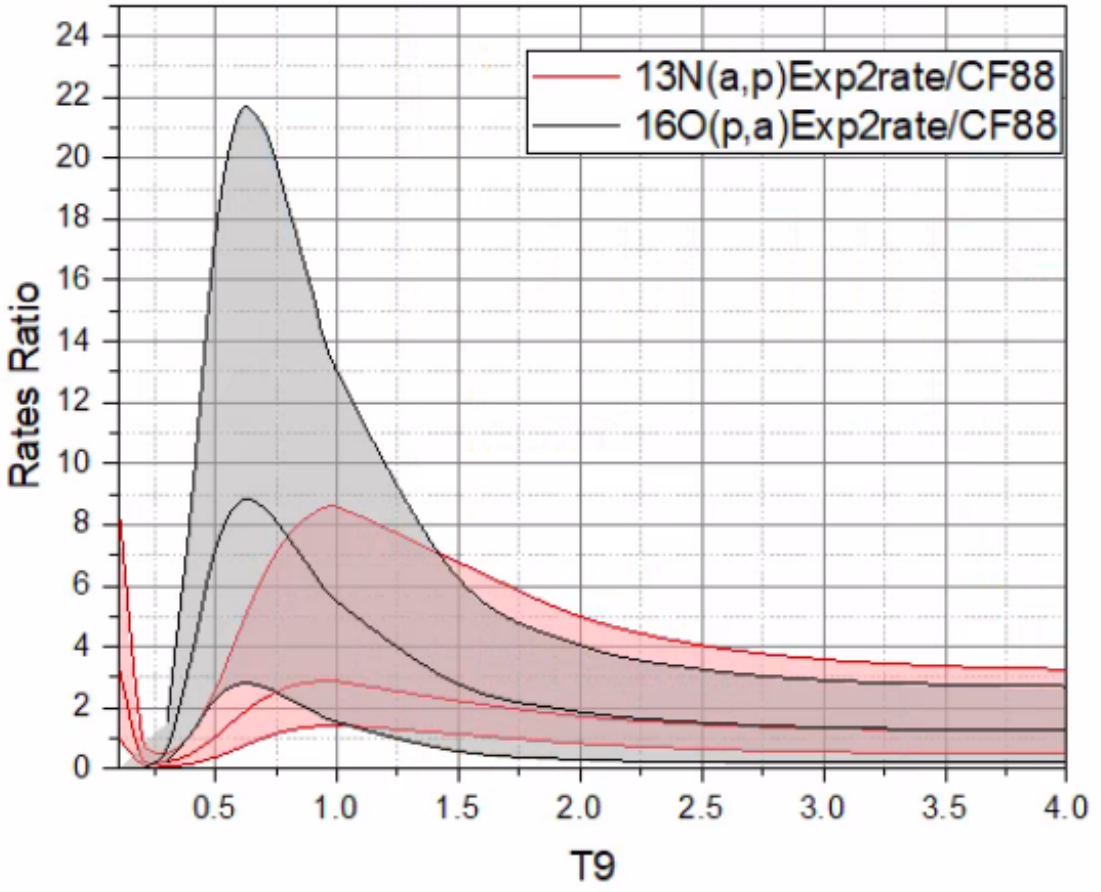

Figure 6.9: Reaction rates of the $^{16}\mathrm{O}(\mathrm{p},\alpha)^{13}\mathrm{N}$ and $^{13}\mathrm{N}(\alpha,\mathrm{p})^{16}\mathrm{O}$ reactions, shown as ratios relative to the corresponding CF88 rates [64]. The rates were calculated using the adopted $^{16}\mathrm{O}(\mathrm{p},\alpha)^{13}\mathrm{N}$ and $^{13}\mathrm{N}(\alpha,\mathrm{p})^{16}\mathrm{O}$ cross sections, with detailed balance applied directly at the cross-section level prior to the rate calculation, rather than being imposed on the reaction rates themselves.

This raises important questions: Why does detailed balance appear to hold at the cross-section level, yet the resulting rates differ significantly? How can the $^{16}\mathrm{O}(\mathrm{p},\alpha)^{13}\mathrm{N}$ rate yield such a large overestimate at low T despite satisfying the formal conditions of detailed balance? Most importantly, which rate should be trusted for astrophysical modelling? To address the first question of whether the principle of

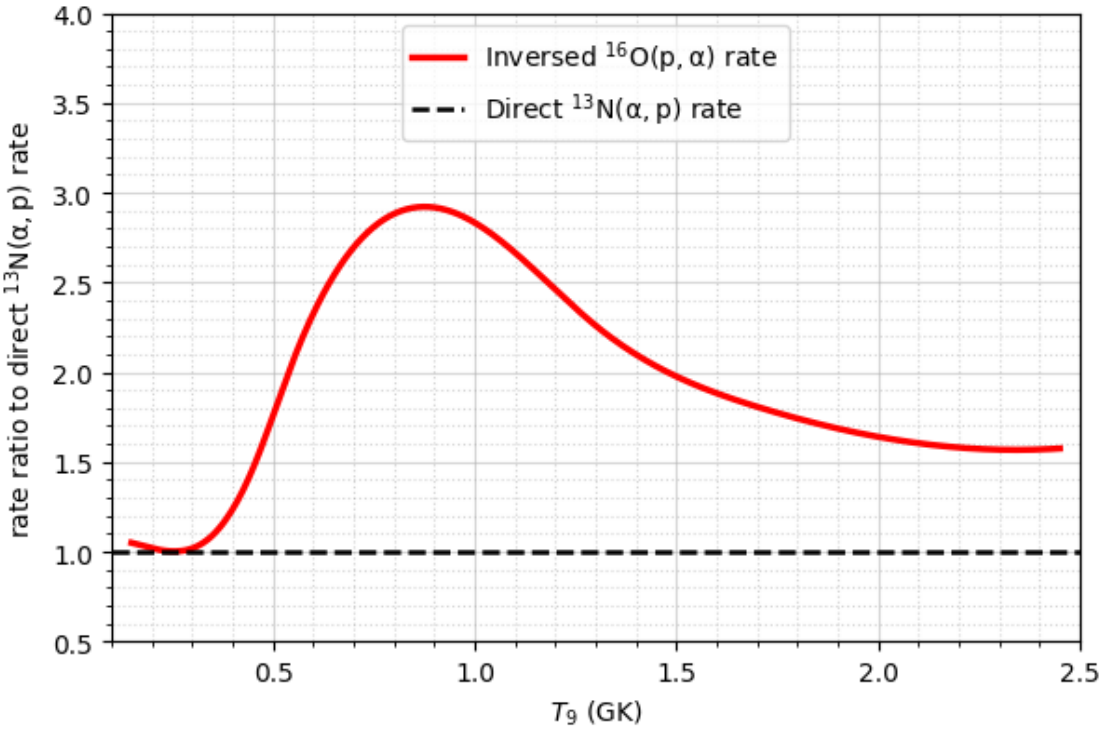

Figure 6.10: Ratio of the $^{13}\mathrm{N}(\alpha,\mathrm{p})^{16}\mathrm{O}$ reaction rates obtained using two independent procedures, with both rates normalised to the directly calculated $^{13}\mathrm{N}(\alpha,\mathrm{p})^{16}\mathrm{O}$ rate. In the first procedure, the $^{13}\mathrm{N}(\alpha,\mathrm{p})^{16}\mathrm{O}$ rate was calculated directly from the $^{13}\mathrm{N}(\alpha,\mathrm{p})^{16}\mathrm{O}$ cross section (black dashed line). In the second procedure, the rate was calculated from the $^{16}\mathrm{O}(\mathrm{p},\alpha)^{13}\mathrm{N}$ cross section and subsequently converted to the inverse $^{13}\mathrm{N}(\alpha,\mathrm{p})^{16}\mathrm{O}$ direction using the detailed-balance formalism (solid red line). Both cross sections were generated using AZURE2 with identical level inputs from Meyer [7]. The deviation from unity peaks at temperatures around $T \approx 0.9$ GK.

detailed balance remains valid at the reaction rate level, it was verified that applying the inversion formula to the $^{16}\mathrm{O}(\mathrm{p},\alpha)^{13}\mathrm{N}$ reaction rate provided in the REACLIB astrophysical library. Specifically, the $^{16}\mathrm{O}(\mathrm{p},\alpha)^{13}\mathrm{N}$ rate was inverted using the detailed balance expression, and the result was compared to the $^{13}\mathrm{N}(\alpha,\mathrm{p})^{16}\mathrm{O}$ rate from REACLIB database. After conversion, it was found that the two $^{13}\mathrm{N}(\alpha,\mathrm{p})^{16}\mathrm{O}$ rates

were identical.

While this agreement is expected given that the CF88 provided by REACLIB rate may have originally been derived by inversion of one rate to the other, it nonetheless confirms that detailed balance is correctly applied and preserved at the rate level. Therefore, the observed discrepancy between the rates derived from $^{16}\mathrm{O}(\mathrm{p},\alpha)^{13}\mathrm{N}$ and $^{13}\mathrm{N}(\alpha,\mathrm{p})^{16}\mathrm{O}$ must originate not from a breakdown in time-reversal symmetry, but from the difference in rate calculation of $^{16}\mathrm{O}(\mathrm{p},\alpha)^{13}\mathrm{N}$ and $^{13}\mathrm{N}(\alpha,\mathrm{p})^{16}\mathrm{O}$ reactions.

The `Exp2Rate` code calculates thermonuclear reaction rates by appling the standard reaction rate integral, which is defined as:

$$\langle \sigma v \rangle = \left(\frac{8}{\pi \mu}\right)^{1/2} \frac{1}{(kT)^{3/2}} \int_0^\infty \sigma(E)\, E\, e^{-E/kT}\, dE, \tag{6.5}$$

where $\sigma(E)$ is the energy-dependent cross section, μ is the reduced mass, and T is the temperature in Kelvin. For charged-particle reactions, the cross section is often expressed in terms of the astrophysical S-factor:

$$\sigma(E) = \frac{S(E)}{E}\, e^{-2\pi\eta}, \tag{6.6}$$

where $2\pi\eta = 31.29\, Z_1 Z_2 \sqrt{\mu/E}$ is the Sommerfeld parameter, and the exponential term accounts for Coulomb barrier penetration. Substituting this expression into the rate integral yields:

$$\langle \sigma v \rangle \propto \int_0^\infty S(E)\, e^{-E/kT - 2\pi\eta}\, dE. \tag{6.7}$$

In this formulation, $S(E)$ is expected to vary slowly with energy, as the dominant energy dependence has been factored out. This assumption is generally valid for most reactions, where the S-factor removes the rapid threshold rise and Coulomb suppression in $\sigma(E)$.

However, in the case of the $^{16}\mathrm{O}(\mathrm{p},\alpha)^{13}\mathrm{N}$ reaction, as shown in Figure 6.11, this assumption breaks down. The steep rise in $\sigma(E)$ near threshold is not fully cancelled by the exponential Coulomb term, and the resulting $S(E)$ still exhibits a strong energy dependence at low energy.

This behaviour of $^{16}\mathrm{O}(\mathrm{p},\alpha)^{13}\mathrm{N}$ may be attributed to the structure of the $^{16}\mathrm{O}$ nucleus. As an even-even nucleus with a relatively high atomic mass number ($A = 16$), the entrance channel in the $^{16}\mathrm{O}(\mathrm{p},\alpha)^{13}\mathrm{N}$ reaction exhibits strong Coulomb suppression. Combined with the small α-penetrability factor, this leads to a cross section that rises steeply just above the threshold and remains strongly suppressed at low energies.

This steepness of the cross section has significant impact for the rate calculation. At $T = 1$ GK, the Gamow window lies approximately between $E_x = 6.1$ and 6.6 MeV. For the $^{13}\mathrm{N}(\alpha,\mathrm{p})^{16}\mathrm{O}$ reaction, the corresponding S-factor is relatively flat within this window, revealing two well defined resonances that dominate the rate. When this S-factor is used as input to `EXP2RATE`, the code integrates over a clearly smoothed data and resonances.

By contrast, the reaction $^{16}\mathrm{O}(\mathrm{p},\alpha)^{13}\mathrm{N}$ does not exhibit isolated resonance peaks within the Gamow window but instead shows a continuously rising cross section and S-factor. As a result, when `Exp2Rate` attempts to integrate over this region, it likely interprets the steep rise as a very broad resonance or a strong low-energy contribution, leading to an overestimation of the reaction rate. This numerical

artefact explains why the $^{16}\mathrm{O}(\mathrm{p},\alpha)^{13}\mathrm{N}$-derived rate after applying detailed balance appears raised relative to the direct $^{13}\mathrm{N}(\alpha,\mathrm{p})^{16}\mathrm{O}$ calculation, even though both are based on identical nuclear input.

Consequently, this study highlights an important methodological insight: when applying the general formula of the reaction rate, it is preferable to use the cross section of the reaction that exhibits the smoother energy dependence within the Gamow window. Although both cross sections are physically equivalent under detailed balance, the numerical integration of steeply rising cross sections especially near threshold, can introduce significant errors if not properly resolved.

In the present case, the $^{16}\mathrm{O}(\mathrm{p},\alpha)^{13}\mathrm{N}$ cross section retains strong energy dependence even after transformation into the S-factor, leading to a numerical overestimation of the rate when used as input to `EXP2RATE`. In contrast, the $^{13}\mathrm{N}(\alpha,\mathrm{p})^{16}\mathrm{O}$ S-factor is much smoother in the relevant energy range, and yields a more stable and reliable rate. These findings demonstrate that, for near threshold reactions with suppressed decay channels, care must be taken in selecting which direction of the reaction to use for rate calculation. When steep energy dependence persists near threshold, the forward reaction with less energy dependency should be preferred for calculating rate.

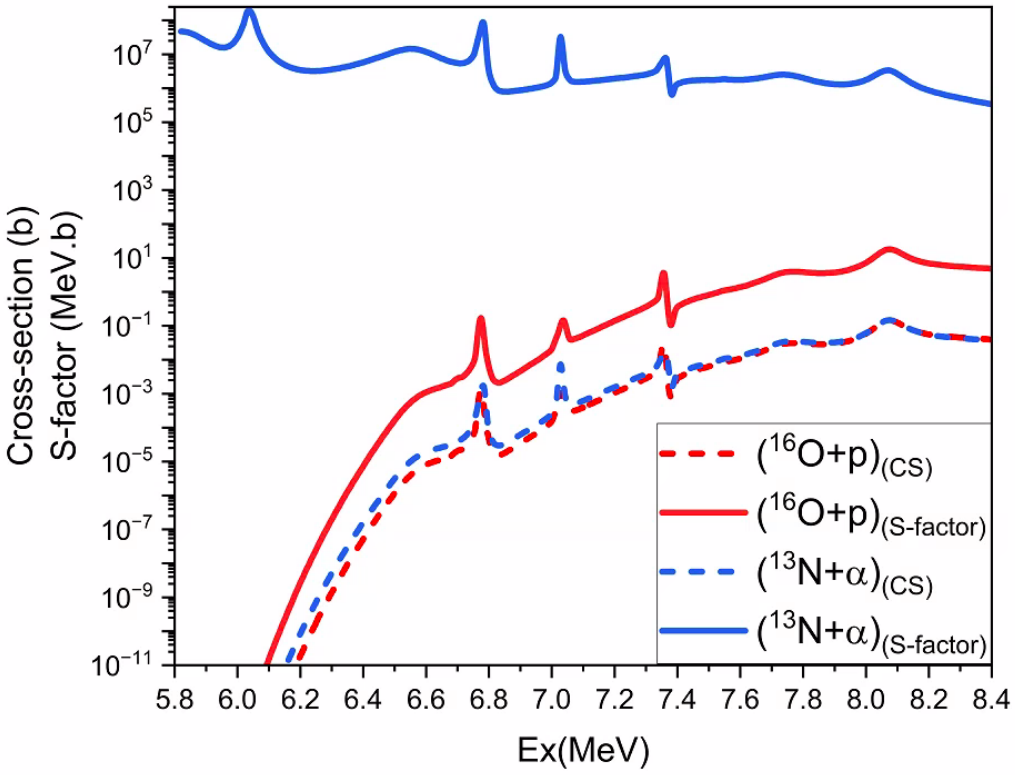

Figure 6.11: Comparison of the cross section and astrophysical S-factor for the $^{16}\mathrm{O}(\mathrm{p},\alpha)^{13}\mathrm{N}$ and $^{13}\mathrm{N}(\alpha,\mathrm{p})^{16}\mathrm{O}$ reactions, shown as a function of the excitation energy E_x of the compound nucleus $^{17}\mathrm{F}$. While the S-factor of $^{13}\mathrm{N}(\alpha,\mathrm{p})^{16}\mathrm{O}$ successfully removes the steep energy dependence of its cross section, the S-factor of $^{16}\mathrm{O}(\mathrm{p},\alpha)^{13}\mathrm{N}$ retains a steep threshold rise.

Chapter 7

Conclusion

7.1 Conclusion

The $^{16}\mathrm{O}(\mathrm{p},\alpha)^{13}\mathrm{N}$ and $^{13}\mathrm{N}(\alpha,\mathrm{p})^{16}\mathrm{O}$ reactions play critical roles in explosive nucleosynthesis processes occurring in both Type Ia supernovae (SNIa) and core-collapse supernovae (CCSN).

In core-collapse supernovae, where temperatures reach $(0.1-1)$ GK, the shock wave mixes hydrogen into the helium shell, initiating proton-capture reactions and increasing $^{13}\mathrm{N}$ production. The fate of the $^{13}\mathrm{N}$, whether it is converted to $^{16}\mathrm{O}$ via the $^{13}\mathrm{N}(\alpha,\mathrm{p})^{16}\mathrm{O}$ reaction or decays into $^{13}\mathrm{C}$, is crucial for interpreting the observed levels of $^{13}\mathrm{C}$ in supernova ejecta. Despite its astrophysical importance, direct experimental cross-section data for the reaction involving $^{13}\mathrm{N}$ remain unavailable due to the short half-life of $^{13}\mathrm{N}$ ($T_{1/2} = 9.97$ minutes). Existing cross-section data for $^{13}\mathrm{N}(\alpha,\mathrm{p})^{16}\mathrm{O}$ are based on measurements from the inverse $^{16}\mathrm{O}(\mathrm{p},\alpha)^{13}\mathrm{N}$ reaction or spectroscopic data of the $^{17}\mathrm{F}$ compound nucleus. However, the crucial energy range for CCSN shock-wave scenarios had not previously been experimentally investigated, resulting

in significant uncertainties.

Recently, a new rate for $^{13}\mathrm{N}(\alpha,\mathrm{p})^{16}\mathrm{O}$ was proposed based on spectroscopic data for $^{17}\mathrm{F}$ states above the α-threshold. However, the current study revealed significant discrepancies between experimental cross-section data and the available nuclear structure data for $^{17}\mathrm{F}$. Additionally, it highlights uncertainties in the spectroscopy of $^{17}\mathrm{F}$, suggesting caution in relying exclusively on such data for reaction rate calculations.

During the explosive oxygen-burning stage of SNIa, at temperatures of approximately $(3{-}4)\,\mathrm{GK}$, the $^{16}\mathrm{O}(\mathrm{p},\alpha)^{13}\mathrm{N}$ reaction contributes significantly to the production of alpha particles [17] [5]. Within the alpha-rich branch, increased alpha abundance enhances calcium production relative to sulphur, a ratio (Ca/S), which is sensitive to the progenitor's metallicity. Therefore, constraining the rate of $^{16}\mathrm{O}(\mathrm{p},\alpha)^{13}\mathrm{N}$ is essential for clarifying its role and improving our understanding of observed variations in the Ca/S ratio across SNIa remnants with differing metallicities.

Previous measurements of the $^{16}\mathrm{O}(\mathrm{p},\alpha)^{13}\mathrm{N}$ cross-section relied on indirect activation methods, in which the cross-section was inferred from the delayed beta decay of the $^{13}\mathrm{N}$ reaction product. However, these techniques introduced significant uncertainties, including the potential loss of $^{13}\mathrm{N}$ activity during transport and difficulties distinguishing true reaction events from the background caused by competing reactions. As a result, discrepancies were found among experimental datasets, particularly in the critical energy range $E_{\mathrm{cm}}^{^{16}\mathrm{O}+p} = 5.7{-}7.1\,\mathrm{MeV}$.

In this study, the $^{16}\mathrm{O}(\mathrm{p},\alpha)^{13}\mathrm{N}$ cross-section was measured using the MUSIC detector that continuously detects reaction products through their energy losses in the detector gas. Unlike previous approaches, MUSIC enables real-time, di-

rect detection of events, eliminating uncertainties associated with delayed detection. Additionally, the setup limited available reaction channels, reducing contributions from competing processes. This was especially valuable in the low-energy region $E_{\mathrm{cm}}^{^{16}\mathrm{O}+p} = 5.7{-}7.1\,\mathrm{MeV}$, where previous studies showed substantial disagreement. A hardware issue during the experiment limited measurement below $E_{\mathrm{cm}}^{^{16}\mathrm{O}+p} < 5.8\,\mathrm{MeV}$, so complementary data from $\mathcal{R}$-matrix analysis of ^{17}F states were incorporated.

Under SNIa conditions, the newly calculated reaction rate closely aligns with the established CF88 rate. Specifically, this work finds a maximum enhancement of only 1.5 times the CF88 value during explosive oxygen burning, substantially lower than previous assumptions of up to a factor of seven. Thus, while the $^{16}\mathrm{O}(\mathrm{p},\alpha)^{13}\mathrm{N}$ reaction affects Ca/S abundance ratios, it cannot solely account for the observed Ca/S variations in SNIa remnants across different metallicities. Furthermore, the new results suggest a need to re-evaluate the assumed suppression of the $^{16}\mathrm{O} + {}^{12}\mathrm{C}$ fusion rate in stellar nucleosynthesis models in light of recent observational evidence.

Although it has been proposed that excited states of ^{16}O may contribute to the $^{16}\mathrm{O}(\mathrm{p},\alpha)^{13}\mathrm{N}$ rate, the present analysis demonstrates that their contribution is negligible. These findings confirm that the rate derived from ground state cross-section measurements of $^{16}\mathrm{O}(\mathrm{p},\alpha)^{13}\mathrm{N}$ reaction effectively represents the full stellar contribution for this reaction.

Finally, the newly measured cross-section for $^{16}\mathrm{O}(\mathrm{p},\alpha)^{13}\mathrm{N}$ was used to calculate an improved rate for the reverse $^{13}\mathrm{N}(\alpha,\mathrm{p})^{16}\mathrm{O}$ reaction, applicable to CCSN conditions. The resulting rate indicates an upper limit approximately three times higher than previous estimates derived from ^{17}F spectroscopy, particularly in the temperature range $T = 0.4{-}0.7\,\mathrm{GK}$. However, current limitations in measuring experimental cross-sections at lower energies restrict our ability to precisely quantify

the role of the $^{13}\mathrm{N}(\alpha,\mathrm{p})^{16}\mathrm{O}$ reaction in $^{13}\mathrm{C}$ nucleosynthesis.

7.2 Summary and future Work

In summary, this research offers a new evaluation for the reaction rates of $^{16}\mathrm{O}(\mathrm{p},\alpha)^{13}\mathrm{N}$ and $^{13}\mathrm{N}(\alpha,\mathrm{p})^{16}\mathrm{O}$ contributing to our understanding of calcium and sulphur nucleosynthesis in Type Ia supernovae, as well as the production of $^{13}\mathrm{C}$ in core-collapse supernova scenarios.

Future investigations should focus on experimentally verifying the proposed reduction in the $^{16}\mathrm{O}+^{12}\mathrm{C}$ reaction rate and on further constraining uncertainties associated with the $^{13}\mathrm{N}(\alpha,\mathrm{p})^{16}\mathrm{O}$ reaction at temperatures $T = 0.4{-}1.0$ GK. Additionally, improved spectroscopic information on the structure of $^{17}\mathrm{F}$ is required to better quantify the contribution of excited states to the $^{16}\mathrm{O}(\mathrm{p},\alpha)^{13}\mathrm{N}$ and $^{13}\mathrm{N}(\alpha,\mathrm{p})^{16}\mathrm{O}$ reaction rates.

References

[1] J. D. Barrow. Cosmology and Elementary Particles. *Fundamentals of Cosmic Physics*, 8:83–200, January 1983.

[2] C.A. Bertulani and T. Kajino. Frontiers in nuclear astrophysics. *Progress in Particle and Nuclear Physics*, 89:56–100, 2016. ISSN 0146-6410. doi: https://doi.org/10.1016/j.ppnp.2016.04.001. URL https://www.sciencedirect.com/science/article/pii/S0146641016300011.

[3] Argonne National Laboratory. Nuclear Astrophysics, 2025. URL https://www.anl.gov/phy/nuclear-astrophysics. Accessed: February 13, 2025.

[4] S. W. Woosley, W. D. Arnett, and D. D. Clayton. Astrophysical importance of the reaction ^{16}O(p, α)^{13}N. *Physics Letters B*, 38(4):196–198, 1972. ISSN 0370-2693. doi: 10.1016/0370-2693(72)90377-2. URL https://www.sciencedirect.com/science/article/pii/0370269372903772.

[5] E. Bravo. ^{16}O(p,α)^{13}N makes explosive oxygen burning sensitive to the metallicity of the progenitors of type ia supernovae. *Astronomy & Astrophysics*, 627:A146, 2019. doi: 10.1051/0004-6361/201936024. URL https://ui.adsabs.harvard.edu/abs/2019A&A...627A.146B.

[6] R. H. Cyburt, A. M. Amthor, R. Ferguson, Z. Meisel, K. Smith, S. Warren, A. Heger, R. D. Hoffman, T. Rauscher, T. Sakharuk, et al. The jina reaclib

database: Its recent updates and impact on type-i x-ray bursts. *The Astrophysical Journal Supplement Series*, 189(1):240, Aug 2010. doi: 10.1088/0067-0049/189/1/240. URL https://www.osti.gov/biblio/1119927.

[7] A. Meyer, N. de Séréville, A. M. Laird, F. Hammache, R. Longland, T. Lawson, M. Pignatari, L. Audouin, D. Beaumel, S. Fortier, J. Kiener, A. Lefebvre-Schuhl, M. G. Pellegriti, M. Stanoiu, and V. Tatischeff. Evaluation of the $^{13}\mathrm{N}(\alpha, p)^{16}\mathrm{O}$ thermonuclear reaction rate and its impact on the isotopic composition of supernova grains. *Phys. Rev. C*, 102:035803, Sep 2020. doi: 10.1103/PhysRevC.102.035803. URL https://link.aps.org/doi/10.1103/PhysRevC.102.035803.

[8] R. E. Azuma, E. Uberseder, E. C. Simpson, C. R. Brune, H. Costantini, R. J. de Boer, J. Görres, M. Heil, P. J. LeBlanc, C. Ugalde, and M. Wiescher. Azure: An r-matrix code for nuclear astrophysics. *Phys. Rev. C*, 81:045805, Apr 2010. doi: 10.1103/PhysRevC.81.045805. URL https://link.aps.org/doi/10.1103/PhysRevC.81.045805.

[9] Y. Cendes. Type ia supernovae: Inside the universe's biggest blasts, Oct 2023. URL https://www.astronomy.com/science/type-ia-supernovae-inside-the-universes-biggest-blasts/. Astronomy Magazine, accessed 28 March 2025.

[10] Paolo A. Mazzali, Friedrich K. Röpke, Stefano Benetti, and Wolfgang Hillebrandt. A common explosion mechanism for type ia supernovae. *Science*, 315(5813):825–828, 2007. doi: 10.1126/science.1136259. URL https://www.science.org/doi/abs/10.1126/science.1136259.

[11] S. Leung and K. Nomoto. Explosive nucleosynthesis in sub-chandrasekhar-mass white dwarf models for type ia supernovae: Dependence on model pa-

rameters. *The Astrophysical Journal*, 888(2):80, Jan 2020. doi: 10.3847/1538-4357/ab5c1f. URL https://dx.doi.org/10.3847/1538-4357/ab5c1f.

[12] F. Thielemann, J. Isern, A. Perego, and P. von Ballmoos. Nucleosynthesis in supernovae. *Space Science Reviews*, 214(3):62, Apr 2018. doi: 10.1007/s11214-018-0494-5. URL https://ui.adsabs.harvard.edu/abs/2018SSRv..214...62T.

[13] J. Jose. *Stellar Explosions: Hydrodynamics and Nucleosynthesis*. CRC Press, 1 edition, 2016. doi: 10.1201/b19165. URL https://doi.org/10.1201/b19165.

[14] Bernard E. J. Pagel. *Nucleosynthesis and Chemical Evolution of Galaxies*. Cambridge University Press, 2 edition, 2009.

[15] Soma De, F. X. Timmes, Edward F. Brown, Alan C. Calder, Dean M. Townsley, Themis Athanassiadou, David A. Chamulak, Wendy Hawley, and Dennis Jack. On Silicon Group Elements Ejected by Supernovae Type Ia. *Astrophys. J.*, 787(2):149, June 2014. doi: 10.1088/0004-637X/787/2/149.

[16] X. Zhao, K. Maeda, X. Wang, L. Wang, H. Sai, J. Zhang, T. Zhang, F. Huang, and L. Rui. The oxygen features in type ia supernovae and implications for the nature of thermonuclear explosions. *The Astrophysical Journal*, 826(2):211, Aug 2016. doi: 10.3847/0004-637X/826/2/211. URL https://dx.doi.org/10.3847/0004-637X/826/2/211.

[17] S. E. Woosley, W. D. Arnett, and D. D. Clayton. The explosive burning of oxygen and silicon. *The Astrophysical Journal Supplement Series*, 26:231, Nov 1973. doi: 10.1086/190282. URL https://ui.adsabs.harvard.edu/abs/1973ApJS...26..231W.

[18] S. W. Woosley, W. D. Arnett, and D. D. Clayton. Astrophysical importance of the reaction ^{16}O(p, α)^{13}N. *Physics Letters B*, 38(4):196–198, Feb 1972.

doi: 10.1016/0370-2693(72)90377-2. URL https://ui.adsabs.harvard.edu/abs/1972PhLB...38..196W.

[19] E. Bravo and G. Martínez-Pinedo. Sensitivity study of explosive nucleosynthesis in type ia supernovae: Modification of individual thermonuclear reaction rates. *Physical Review C*, 85(5):055805, May 2012. doi: 10.1103/PhysRevC.85.055805. URL https://link.aps.org/doi/10.1103/PhysRevC.85.055805.

[20] S. M. Couch. The mechanism(s) of core-collapse supernovae. *Philosophical Transactions of the Royal Society A: Mathematical, Physical and Engineering Sciences*, 375(2105), Sep 2017. doi: 10.1098/rsta.2016.0271. URL https://www.osti.gov/biblio/1540655.

[21] H.-Th. Janka, K. Langanke, A. Marek, G. Martínez-Pinedo, and B. Müller. Theory of core-collapse supernovae. *Physics Reports*, 442(1):38–74, 2007. doi: 10.1016/j.physrep.2007.02.002. URL https://www.sciencedirect.com/science/article/pii/S0370157307000439. The Hans Bethe Centennial Volume 1906–2006.

[22] T. Foglizzo. Explosion physics of core-collapse supernovae. In *Handbook of Supernovae*, pages 1053–1073. Springer International Publishing, Cham, 2017. ISBN 978-3-319-21846-5. doi: 10.1007/978-3-319-21846-5_52. URL https://doi.org/10.1007/978-3-319-21846-5_52.

[23] S. Yamada, H. Nagakura, R. Akaho, A. Harada, S. Furusawa, W. Iwakami, H. Okawa, H. Matsufuru, and K. Sumiyoshi. Physical mechanism of core-collapse supernovae that neutrinos drive. *Proceedings of the Japan Academy, Series B*, 100(3):190–233, Mar 2024. doi: 10.2183/pjab.100.015. URL https://ui.adsabs.harvard.edu/abs/2024PJAB..100..190Y.

[24] M. Pignatari, E. Zinner, P. Hoppe, C. J. Jordan, B. K. Gibson, R. Trappitsch, F. Herwig, C. Fryer, R. Hirschi, and F. X. Timmes. Carbon-rich

presolar grains from massive stars: Subsolar ^{12}c/^{13}c and ^{14}n/^{15}n ratios and the mystery of ^{15}n. *The Astrophysical Journal Letters*, 808(2):L43, Jul 2015. doi: 10.1088/2041-8205/808/2/L43. URL https://dx.doi.org/10.1088/2041-8205/808/2/L43.

[25] P. A. Denissenkov, J. W. Truran, M. Pignatari, R. Trappitsch, C. Ritter, F. Herwig, U. Battino, K. Setoodehnia, and B. Paxton. Mesa and nugrid simulations of classical novae: Co and one nova nucleosynthesis. *Monthly Notices of the Royal Astronomical Society*, 442(3):2058–2074, Jun 2014. doi: 10.1093/mnras/stu1000. URL https://doi.org/10.1093/mnras/stu1000.

[26] Ian J. Thompson and Filomena M. Nunes. *Nuclear Reactions for Astrophysics*. Cambridge University Press, 2009.

[27] Alastair Graham Walter Cameron. *Stellar evolution, nuclear astrophysics, and nucleogenesis*. Courier Corporation, 2013.

[28] L. Trache. Indirect methods for nuclear astrophysics with radioactive nuclear beams. In *AIP Conference Proceedings*, volume 1213(1), pages 125–136. American Institute of Physics, 2010.

[29] C. Iliadis. Thermonuclear reactions. In *Nuclear Physics of Stars*, chapter 3, pages 139–206. John Wiley & Sons, Ltd, 2015. ISBN 9783527692668. doi: 10.1002/9783527692668.ch3. URL https://onlinelibrary.wiley.com/doi/abs/10.1002/9783527692668.ch3.

[30] W. A. Fowler, G. R. Caughlan, and B. A. Zimmerman. Thermonuclear reaction rates. *Annual Review of Astronomy and Astrophysics*, 5:525–570, 1967. doi: 10.1146/annurev.aa.05.090167.002521. URL https://www.osti.gov/biblio/4666476.

[31] C E Rolfs and W S Rodney. *Cauldrons in the cosmos: Nuclear astrophysics*.

University of Chicago Press,Chicago, IL, 01 1988. URL https://www.osti.gov/biblio/5842032.

[32] H. A. Bethe and G. Placzek. Resonance effects in nuclear processes. *Phys. Rev.*, 51:450–484, Mar 1937. doi: 10.1103/PhysRev.51.450. URL https://link.aps.org/doi/10.1103/PhysRev.51.450.

[33] Christian Iliadis, John M. D'Auria, Sumner Starrfield, William J. Thompson, and Michael Wiescher. Proton-induced thermonuclear reaction rates for a = 20–40 nuclei. *The Astrophysical Journal Supplement Series*, 134(1):151, may 2001. doi: 10.1086/320364. URL https://doi.org/10.1086/320364.

[34] W. A. Fowler, G. R. Caughlan, and B. A. Zimmerman. Thermonuclear reaction rates, II. *Annual Review of Astronomy and Astrophysics*, 13:69–112, Jan 1975. doi: 10.1146/annurev.aa.13.090175.000441. URL https://ui.adsabs.harvard.edu/abs/1975ARA&A..13...69F.

[35] C. Angulo, M. Arnould, M. Rayet, P. Descouvemont, D. Baye, C. Willain, A. Coc, S. Barhoumi, P. Aguer, C. Rolfs, R. Kunz, J. W. Hammer, A. Mayer, T. Paradellis, S. Kossionides, C. Chronidou, K. Spyrou, S. Degl'Innocenti, G. Fiorentini, B. Ricci, S. Zavatarelli, C. Providência, H. J. Wolters, J. C. Soares, C. Grama, J. Rahighi, A. C. Shotter, and M. Laméhi-Rachti. A compilation of charged-particle induced thermonuclear reaction rates. *Nuclear Physics A*, 656(1):3–183, 1999. doi: 10.1016/S0375-9474(99)00030-5. URL https://doi.org/10.1016/S0375-9474(99)00030-5.

[36] Walter Hauser and Herman Feshbach. The inelastic scattering of neutrons. *Phys. Rev.*, 87:366–373, Jul 1952. doi: 10.1103/PhysRev.87.366. URL https://link.aps.org/doi/10.1103/PhysRev.87.366.

[37] T. Rauscher and F. K. Thielemann. Astrophysical reaction rates from statistical model calculations. *Atomic Data and Nuclear Data Tables*, 75(1–2):

1–351, May 2000. doi: 10.1006/adnd.2000.0834. URL http://edoc.unibas.ch/dok/A5839325.

[38] A. J. Koning, S. Hilaire, and S. Goriely. Global and local level density models. *Nuclear Physics A*, 810(1):13–76, 2008. doi: 10.1016/j.nuclphysa.2008.06.005. URL https://www.sciencedirect.com/science/article/pii/S0375947408005903.

[39] A. Koning, S. Hilaire, and S. Goriely. TALYS: Modeling of nuclear reactions. *European Physical Journal A*, 59(6):131, Jun 2023. doi: 10.1140/epja/s10050-023-01034-3. URL https://ui.adsabs.harvard.edu/abs/2023EPJA...59..131K.

[40] T. Rauscher. Suppression of excited-state contributions to stellar reaction rates. *Phys. Rev. C*, 88:035803, Sep 2013. doi: 10.1103/PhysRevC.88.035803. URL https://link.aps.org/doi/10.1103/PhysRevC.88.035803.

[41] G. G. Kiss, T. Rauscher, Gy. Gyürky, A. Simon, Zs. Fülöp, and E. Somorjai. Coulomb suppression of the stellar enhancement factor. *Phys. Rev. Lett.*, 101:191101, Nov 2008. doi: 10.1103/PhysRevLett.101.191101. URL https://link.aps.org/doi/10.1103/PhysRevLett.101.191101.

[42] T. Rauscher, G. G. Kiss, Gy. Gyürky, A. Simon, Zs. Fülöp, and E. Somorjai. Suppression of the stellar enhancement factor and the reaction ^{85}Rb$(p,n)^{85}$Sr. *Phys. Rev. C*, 80:035801, Sep 2009. doi: 10.1103/PhysRevC.80.035801. URL https://link.aps.org/doi/10.1103/PhysRevC.80.035801.

[43] P. Mohr, C. Angulo, P. Descouvemont, and H. Utsunomiya. Relation between the ^{16}O$(\alpha,\gamma)^{20}$Ne reaction and its reverse ^{20}Ne$(\gamma,\alpha)^{16}$O reaction in stars and in the laboratory. *The European Physical Journal A: Hadrons and Nuclei*, 27(1):75–78, Mar 2006. doi: 10.1140/epja/i2006-08-010-1. URL https://doi.org/10.1140/epja/i2006-08-010-1.

[44] J M Blatt and V F Weisskopf. *Theoretical nuclear physics*. Springer-Verlag New York Inc.,New York, NY, 01 1979. URL https://www.osti.gov/biblio/5992854.

[45] H Frauenfelder and E M Henley. *Subatomic physics*. Prentice-Hall, Inc., Englewood Cliffs, NJ, 01 1974. URL https://www.osti.gov/biblio/4308008.

[46] Eugene P. Wigner. Resonance reactions. *Phys. Rev.*, 70:606–618, Nov 1946. doi: 10.1103/PhysRev.70.606. URL https://link.aps.org/doi/10.1103/PhysRev.70.606.

[47] E. P. Wigner and L. Eisenbud. Higher angular momenta and long range interaction in resonance reactions. *Phys. Rev.*, 72:29–41, Jul 1947. doi: 10.1103/PhysRev.72.29. URL https://link.aps.org/doi/10.1103/PhysRev.72.29.

[48] A. M. Lane and R. G. Thomas. R-matrix theory of nuclear reactions. *Rev. Mod. Phys.*, 30:257–353, Apr 1958. doi: 10.1103/RevModPhys.30.257. URL https://link.aps.org/doi/10.1103/RevModPhys.30.257.

[49] P. Descouvemont and D. Baye. The r-matrix theory. *Reports on Progress in Physics*, 73:036301, 2010. doi: 10.1088/0034-4885/73/3/036301.

[50] R. E. Azuma, E. Uberseder, E. C. Simpson, C. R. Brune, H. Costantini, R. J. de Boer, J. Görres, M. Heil, P. J. LeBlanc, C. Ugalde, and M. Wiescher. *AZURE2: R-Matrix Code for Nuclear Astrophysics*, 2010. URL https://azure.nd.edu/download.php?s=1&d=3&f=azure2_manual.pdf. User manual, accessed 4 March 2025.

[51] R. J. deBoer, J. Görres, M. Wiescher, R. E. Azuma, A. Best, C. R. Brune, C. E. Fields, S. Jones, M. Pignatari, D. Sayre, K. Smith, F. X. Timmes, and E. Uberseder. The $^{12}\mathbf{C}(\alpha,\gamma)^{16}\mathbf{O}$ reaction and its implications for stellar helium burning. *Rev. Mod. Phys.*, 89:035007, Sep 2017.

doi: 10.1103/RevModPhys.89.035007. URL https://link.aps.org/doi/10.1103/RevModPhys.89.035007.

[52] R. J. deBoer, J. Görres, G. Imbriani, P. J. LeBlanc, E. Uberseder, and M. Wiescher. R-Matrix analysis of ^{16}O compound nucleus reactions. *Physical Review C*, 87(1):015802, Jan 2013. doi: 10.1103/PhysRevC.87.015802. URL https://link.aps.org/doi/10.1103/PhysRevC.87.015802.

[53] R. J. deBoer, J. Görres, K. Smith, E. Uberseder, M. Wiescher, A. Kontos, G. Imbriani, A. Di Leva, and F. Strieder. Monte carlo uncertainty of the ^{3}He$(\alpha,\gamma)^7$Be reaction rate. *Phys. Rev. C*, 90:035804, Sep 2014. doi: 10.1103/PhysRevC.90.035804. URL https://link.aps.org/doi/10.1103/PhysRevC.90.035804.

[54] W. D. Mackintosh. *Rutherford Scattering*, pages 403–418. Springer US, Boston, MA, 1974. ISBN 978-1-4613-4490-2. doi: 10.1007/978-1-4613-4490-2_17. URL https://doi.org/10.1007/978-1-4613-4490-2_17.

[55] G. F. Knoll. *Radiation Detection and Measurement*. Wiley, New York, NY, 4 edition, 2010. URL https://cds.cern.ch/record/1300754.

[56] J. F. Ziegler, M. D. Ziegler, and J. P. Biersack. Srim – the stopping and range of ions in matter (2010). *Nuclear Instruments and Methods in Physics Research Section B: Beam Interactions with Materials and Atoms*, 268(11):1818–1823, 2010. doi: 10.1016/j.nimb.2010.02.091. URL https://www.sciencedirect.com/science/article/pii/S0168583X10001862. 19th International Conference on Ion Beam Analysis.

[57] H. W. Fulbright. *Ionization Chambers in Nuclear Physics*, pages 1–51. Springer Berlin Heidelberg, Berlin, Heidelberg, 1958. ISBN 978-3-642-45903-

0. doi: 10.1007/978-3-642-45903-0_1. URL https://doi.org/10.1007/978-3-642-45903-0_1.

[58] J. E. Johnstone, R. Kumar, S. Hudan, V. Singh, R. T. deSouza, J. Allen, D. W. Bardayan, D. Blankstein, C. Boomershine, S. Carmichael, A. Clark, S. Coil, S. L. Henderson, and P. D. O'Malley. Music@indiana: An effective tool for accurate measurement of fusion with low-intensity radioactive beams. *Nuclear Instruments and Methods in Physics Research Section A: Accelerators, Spectrometers, Detectors and Associated Equipment*, 1014:165697, Oct 2021. doi: 10.1016/j.nima.2021.165697. URL https://ui.adsabs.harvard.edu/abs/2021NIMPA101465697J.

[59] A. M. Laird, P. Amaudruz, L. Buchmann, S. P. Fox, B. R. Fulton, D. Gigliotti, T. Kirchner, P. D. Mumby-Croft, R. Openshaw, M. M. Pavan, J. Pearson, G. Ruprecht, G. Sheffer, and P. Walden. Status of tactic: A detector for nuclear astrophysics. *Nuclear Instruments and Methods in Physics Research Section A: Accelerators, Spectrometers, Detectors and Associated Equipment*, 573(1–2):306–309, Apr 2007. doi: 10.1016/j.nima.2006.10.384. URL https://ui.adsabs.harvard.edu/abs/2007NIMPA.573..306L.

[60] E. Koshchiy, J. C. Blackmon, G. V. Rogachev, I. Wiedenhöver, L. Baby, P. Barber, D. W. Bardayan, J. Belarge, D. Caussyn, and E. D. Johnson. Anasen: The array for nuclear astrophysics and structure with exotic nuclei. *Nuclear Instruments and Methods in Physics Research Section A: Accelerators, Spectrometers, Detectors and Associated Equipment*, 870(C):1–9, Oct 2017. doi: 10.1016/j.nima.2017.07.030. URL https://www.osti.gov/biblio/1693723.

[61] Y. Ayyad, N. Abgrall, T. Ahn, H. Álvarez-Pol, D. Bazin, S. Beceiro-Novo, L. Carpenter, R. J. Cooper, M. Cortesi, A. O. Macchiavelli, W. Mittig, B. Olaizola, J. S. Randhawa, C. Santamaria, N. Watwood, J. C. Zamora,

and R. G. T. Zegers. Next-generation experiments with the active target time projection chamber (at-tpc). *Nuclear Instruments and Methods in Physics Research Section A: Accelerators, Spectrometers, Detectors and Associated Equipment*, 954:161341, Feb 2020. doi: 10.1016/j.nima.2018.10.019. URL https://ui.adsabs.harvard.edu/abs/2020NIMPA.95461341A.

[62] The Free Dictionary by Farlex. Ionization chamber, 2025. URL https://encyclopedia2.thefreedictionary.com/Ionization+Chamber. Accessed: 4 March 2025.

[63] R. V. Wagoner. Synthesis of the elements within objects exploding from very high temperatures. *The Astrophysical Journal Supplement Series*, 18:247–295, Jun 1969. doi: 10.1086/190191. URL https://www.osti.gov/biblio/4772978.

[64] G. R. Caughlan and W. A. Fowler. Thermonuclear reaction rates v. *Atomic Data and Nuclear Data Tables*, 40(2):283–334, Nov 1988. doi: 10.1016/0092-640X(88)90009-5. URL https://linkinghub.elsevier.com/retrieve/pii/0092640X88900095.

[65] A. L. Sallaska, C. Iliadis, A. E. Champagne, S. Goriely, S. Starrfield, and F. X. Timmes. Starlib: A next-generation reaction-rate library for nuclear astrophysics. *The Astrophysical Journal Supplement Series*, 207(1):18, Jul 2013. doi: 10.1088/0067-0049/207/1/18. URL https://dx.doi.org/10.1088/0067-0049/207/1/18.

[66] L. Piersanti, E. Bravo, S. Cristallo, I. Domínguez, O. Straniero, A. Tornambé, and G. Martínez-Pinedo. Sne ia keep memory of their progenitor metallicity. *The Astrophysical Journal Letters*, 836(1):L9, Feb 2017. doi: 10.3847/2041-8213/aa5c7e. URL https://dx.doi.org/10.3847/2041-8213/aa5c7e.

[67] H. Martínez-Rodríguez, A. L. Piro, J. Schwab, and C. Badenes. Neutronization

during carbon simmering in type ia supernova progenitors. *The Astrophysical Journal*, 825(1):57, Jun 2016. doi: 10.3847/0004-637X/825/1/57. URL https://dx.doi.org/10.3847/0004-637X/825/1/57.

[68] H. Martínez-Rodríguez, C. Badenes, H. Yamaguchi, E. Bravo, F. X. Timmes, B. J. Miles, D. M. Townsley, A. L. Piro, H. Mori, B. Andrews, and S. Park. Observational evidence for high neutronization in supernova remnants: Implications for type ia supernova progenitors. *The Astrophysical Journal*, 843(1): 35, Jun 2017. doi: 10.3847/1538-4357/aa72f8. URL https://dx.doi.org/10.3847/1538-4357/aa72f8.

[69] V. V. Zerkin and B. Pritychenko. The experimental nuclear reaction data (exfor): Extended computer database and web retrieval system. *Nuclear Instruments and Methods in Physics Research Section A: Accelerators, Spectrometers, Detectors and Associated Equipment*, 888:31–43, Apr 2018. doi: 10.1016/j.nima.2018.01.045. URL https://ui.adsabs.harvard.edu/abs/2018NIMPA.888...31Z.

[70] A. B. Whitehead and J. S. Foster. Activation cross sections for ^{12}C(p,pn)^{11}C, ^{16}O(p,α)^{13}N, and ^{19}F(p,pn)^{18}F. *Canadian Journal of Physics*, 36(10):1276–1285, Oct 1958. doi: 10.1139/p58-132. URL https://ui.adsabs.harvard.edu/abs/1958CaJPh..36.1276W.

[71] R. H. McCamis, G. A. Moss, and J. M. Cameron. Total cross section of ^{16}O(p,α)^{13}N from threshold to 7.7 mev. *Canadian Journal of Physics*, 51 (16):1689–1692, Aug 1973. doi: 10.1139/p73-223. URL https://ui.adsabs.harvard.edu/abs/1973CaJPh..51.1689M.

[72] A. V. Nero and A. J. Howard. ^{16}O(p,α_0)^{13}N cross-section measurements. *Nuclear Physics A*, 210(1):60–66, Aug 1973. doi: 10.1016/0375-9474(73)90503-4. URL https://ui.adsabs.harvard.edu/abs/1973NuPhA.210...60N.

[73] W. Gruhle and B. Kober. The reactions ^{16}O(p,α), ^{20}Ne(p,α), and ^{24}Mg(p,α). *Nuclear Physics A*, 286(3):523–530, Aug 1977. doi: 10.1016/0375-9474(77)90601-7. URL https://ui.adsabs.harvard.edu/abs/1977NuPhA.286..523G.

[74] M. Sajjad, R. M. Lambrecht, and A. P. Wolf. Cyclotron isotopes and radiopharmaceuticals. *Radiochimica Acta*, 39(3):165–168, Jul 1986. doi: 10.1524/ract.1986.39.3.165. URL https://www.degruyter.com/document/doi/10.1524/ract.1986.39.3.165/html.

[75] J. B. Cumming, A. M. Poskanzer, and J. Hudis. Loss of ^{11}c from plastic foils and its effect on cross-section measurements. *Physical Review Letters*, 6(9):484–485, May 1961. doi: 10.1103/PhysRevLett.6.484. URL https://link.aps.org/doi/10.1103/PhysRevLett.6.484.

[76] H. Fuchs and K. H. Lindenberger. Loss of activity from betatron irradiated samples by diffusion. *Nuclear Instruments and Methods*, 7:106–111, May 1960. doi: 10.1016/0029-554X(60)90136-1. URL https://www.osti.gov/biblio/4163248.

[77] R. L. Dangle, L. D. Oppliger, and G. Hardie. ^{16}O(p,α)^{13}N and ^{16}O(p,p$'$)^{16}O* differential cross sections. *Physical Review*, 133(3B):B647–B659, Feb 1964. doi: 10.1103/PhysRev.133.B647. URL https://link.aps.org/doi/10.1103/PhysRev.133.B647.

[78] C. F. Williamson, J. Boujot, and J. Picard. Tables of range and stopping power of chemical elements for charged particles of energy 0.5 to 500 mev. Technical report, Commissariat à l'Énergie Atomique, Centre d'Études Nucléaires, Saclay, Jan 1966. URL https://www.osti.gov/biblio/4529550.

[79] A. Hermanne, F. T. Tárkányi, A. V. Ignatyuk, S. Takács, and R. Capote. Upgrade of iaea recommended data of selected nuclear reactions for produc-

tion of pet and spect isotopes. *Nuclear Data Sheets*, 173:285–308, 2021. doi: 10.1016/j.nds.2021.04.008. URL https://www.sciencedirect.com/science/article/pii/S0090375221000247. Special Issue on Nuclear Reaction Data.

[80] H. Padé. Sur la représentation approchée d'une fonction par des fractions rationnelles. In *Annales scientifiques de l'Ecole normale supérieure*, volume 9, pages 3–93, 1892.

[81] G. A. Baker and J. L. Gammel. The padé approximant. *Journal of Mathematical Analysis and Applications*, 2(1):21–30, 1961. doi: 10.1016/0022-247X(61)90042-7. URL https://www.sciencedirect.com/science/article/pii/0022247X61900427.

[82] S. M. Qaim, F. T. Tárkányi, P. Obložinský, K. Gul, A. Hermanne, M. G. Mustafa, F. M. Nortier, B. Scholten, Y. N. Shubin, S. Takács, and Y. Zhuang. Charged-particle cross section database for medical radioisotope production. *Journal of Nuclear Science and Technology*, 39:1282–1285, Aug 2002. doi: 10.1080/00223131.2002.10875338. URL https://ui.adsabs.harvard.edu/abs/2002JNST...39S1282Q.

[83] Michiaki Furukawa, Yoshihide Ishizaki, Yoshihiro Nakano, Tadashi Nozaki, Yoshio Saji, and Shigeo Tanaka. Excitation Function for the Reaction B^{11}(p, n)C^{11} up to E_p{=}15 MeV and Energy Levels of C^{12}. *Journal of the Physical Society of Japan*, 15(12):2167–2170, December 1960. doi: 10.1143/JPSJ.15.2167.

[84] T. Rauscher. EXP2RATE code (2003), 2003. URL https://nucastro.org/codes.html. A computational tool for calculating thermonuclear reaction rates in nuclear astrophysics.

[85] Longland, Richard. Correlated uncertainties in monte carlo reaction rate cal-

culations. *A&A*, 604:A34, 2017. doi: 10.1051/0004-6361/201730911. URL https://doi.org/10.1051/0004-6361/201730911.

[86] Longland, Richard and de Séréville, Nicolas. Correlated energy uncertainties in reaction rate calculations. *A&A*, 642:A41, 2020. doi: 10.1051/0004-6361/202038151. URL https://doi.org/10.1051/0004-6361/202038151.

[87] A. Sonzogni. NNDC chart of nuclides. In *International Conference on Nuclear Data for Science and Technology*, pages 105–106, 2007. doi: 10.1051/ndata:07530. URL https://doi.org/10.1051/ndata:07530.

[88] S. R. Salisbury and H. T. Richards. ^{17}F level parameters. *Physical Review*, 126(6):2147–2158, Jun 1962. doi: 10.1103/PhysRev.126.2147. URL https://link.aps.org/doi/10.1103/PhysRev.126.2147.

[89] S. R. Salisbury, G. Hardie, L. Oppliger, and R. Dangle. Proton-oxygen differential scattering cross sections. ii. *Phys. Rev.*, 126:2143–2147, Jun 1962. doi: 10.1103/PhysRev.126.2143. URL https://link.aps.org/doi/10.1103/PhysRev.126.2143.

[90] W. J. Huang, M. Wang, F. G. Kondev, G. Audi, and S. Naimi. The ame2016 atomic mass evaluation (i): Evaluation of input data and adjustment procedures. *Chinese Physics C*, 41(3):030002, Mar 2017. doi: 10.1088/1674-1137/41/3/030002. URL https://dx.doi.org/10.1088/1674-1137/41/3/030002.

[91] J. Legg, unknown. Private communication.

[92] S. E. Darden and H. R. Hiddleston. Spins of the 3.854-MeV and 7.026-MeV levels in ^{17}F from ^{16}O$(\vec{p},p)^{16}$O. *Phys. Rev. C*, 9:800–801, Feb 1974. doi: 10.1103/PhysRevC.9.800. URL https://link.aps.org/doi/10.1103/PhysRevC.9.800.

[93] H. T. Richards, unknown. Private communication.

[94] G. P. Bauer. Senior honors thesis, 1978. Unpublished.

[95] S. Sen. Spin and parity of the 6.699 MeV level in ^{17}F. *Physical Review C*, 25(2):1054–1057, Feb 1982. doi: 10.1103/PhysRevC.25.1054. URL `https://link.aps.org/doi/10.1103/PhysRevC.25.1054`.

[96] M. G. Pellegriti, F. Hammache, P. Roussel, L. Audouin, D. Beaumel, P. Descouvemont, S. Fortier, L. Gaudefroy, J. Kiener, A. Lefebvre-Schuhl, M. Stanoiu, V. Tatischeff, and M. Vilmay. Indirect study of the ^{13}C$(\alpha, n)^{16}$O reaction via the ^{13}C(^{7}Li,t)^{17}O transfer reaction. *Phys. Rev. C*, 77:042801, Apr 2008. doi: 10.1103/PhysRevC.77.042801. URL `https://link.aps.org/doi/10.1103/PhysRevC.77.042801`.

[97] I. Pogrebnyak, C. Howard, C. Iliadis, R. Longland, and G. E. Mitchell. Mean proton and α-particle reduced widths of the Porter–Thomas distribution and astrophysical applications. *Physical Review C*, 88(1):015808, Jul 2013. doi: 10.1103/PhysRevC.88.015808. URL `https://link.aps.org/doi/10.1103/PhysRevC.88.015808`.

[98] R. Longland, C. Iliadis, A. E. Champagne, J. R. Newton, C. Ugalde, A. Coc, and R. Fitzgerald. Charged-particle thermonuclear reaction rates: I. monte carlo method and statistical distributions. *Nuclear Physics A*, 841 (1):1–30, 2010. doi: 10.1016/j.nuclphysa.2010.04.008. URL `https://www.sciencedirect.com/science/article/pii/S0375947410004185`. The 2010 Evaluation of Monte Carlo Based Thermonuclear Reaction Rates.

[99] P. F. F. Carnelli, S. Almaraz-Calderon, K. E. Rehm, M. Albers, M. Alcorta, P. F. Bertone, B. Digiovine, H. Esbensen, J. Fernández Niello, D. Henderson, C. L. Jiang, J. Lai, S. T. Marley, O. Nusair, T. Palchan-Hazan,

R. C. Pardo, M. Paul, and C. Ugalde. Multi-sampling ionization chamber (music) for measurements of fusion reactions with radioactive beams. *Nuclear Instruments and Methods in Physics Research Section A: Accelerators, Spectrometers, Detectors and Associated Equipment*, 799:197–202, 2015. doi: 10.1016/j.nima.2015.07.030. URL `https://www.sciencedirect.com/science/article/pii/S0168900215008591`.

[100] W. B. Christie, J. L. Romero, F. P. Brady, C. E. Tull, C. M. Castaneda, E. F. Barasch, M. L. Webb, J. R. Drummond, H. J. Crawford, I. Flores, D. E. Greiner, P. J. Lindstrom, H. Sann, and J. C. Young. A multiple sampling ionization chamber (music) for measuring the charge of relativistic heavy ions. *Nuclear Instruments and Methods in Physics Research Section A: Accelerators, Spectrometers, Detectors and Associated Equipment*, 255(3):466–476, 1987. doi: 10.1016/0168-9002(87)91213-7. URL `https://www.sciencedirect.com/science/article/pii/0168900287912137`.

[101] P. F. F. Carnelli, S. Almaraz-Calderon, K. E. Rehm, M. Albers, M. Alcorta, P. F. Bertone, B. Digiovine, H. Esbensen, J. O. Fernández Niello, D. Henderson, C. L. Jiang, J. Lai, S. T. Marley, O. Nusair, T. Palchan-Hazan, R. C. Pardo, M. Paul, and C. Ugalde. Measurements of fusion reactions of low-intensity radioactive carbon beams on ^{12}C and their implications for the understanding of x-ray bursts. *Phys. Rev. Lett.*, 112:192701, May 2014. doi: 10.1103/PhysRevLett.112.192701. URL `https://link.aps.org/doi/10.1103/PhysRevLett.112.192701`.

[102] M. L. Avila, K. E. Rehm, S. Almaraz-Calderon, A. D. Ayangeakaa, C. Dickerson, C. R. Hoffman, C. L. Jiang, B. P. Kay, J. Lai, O. Nusair, R. C. Pardo, D. Santiago-Gonzalez, R. Talwar, and C. Ugalde. Study of (α,p) and (α,n) reactions with a multi-sampling ionization chamber. *Nuclear Instruments and Methods in Physics Research Section A: Accelerators, Spec-*

trometers, Detectors and Associated Equipment, 859:63–68, 2017. doi: 10.1016/j.nima.2017.03.060. URL https://www.sciencedirect.com/science/article/pii/S0168900217304187.

[103] R. Talwar, M. J. Bojazi, P. Mohr, K. Auranen, M. L. Avila, A. D. Ayangeakaa, J. Harker, C. R. Hoffman, C. L. Jiang, S. A. Kuvin, B. S. Meyer, K. E. Rehm, D. Santiago-Gonzalez, J. Sethi, C. Ugalde, and J. R. Winkelbauer. Experimental study of ^{38}Ar + α reaction cross sections relevant to the ^{41}Ca abundance in the solar system. *Phys. Rev. C*, 97:055801, May 2018. doi: 10.1103/PhysRevC.97.055801. URL https://link.aps.org/doi/10.1103/PhysRevC.97.055801.

[104] Argonne National Laboratory. About ATLAS Facility. https://www.anl.gov/atlas/about-atlas, n.d. Accessed: 2024-12-12.

[105] C. Fougeres. Advances in the detection of low-energy nuclear reactions using a tpc. *Texas A&M Cyclotron Institute TPC Workshop 2023, College Station, TX*, October 2023. URL https://cyclotron.tamu.edu/tpc2023/slides/5_Thu_AM/CFougeres_TPC2023.pdf.

[106] W. Ong. Active target tpc detector developments. *ANL Active Target Workshop 2019, Argonne National Laboratory, Argonne, IL*, September 2019. URL https://aaw2019.phy.anl.gov/Talks/WOng.pdf.

[107] Ashley Ann Hood. *Measurements of the ^{16}C + ^{12}C and ^{16}C + ^{13}C Fusion Cross Sections with Implications for Astrophysics*. Phd dissertation, Louisiana State University, 2019. URL https://repository.lsu.edu/gradschool_dissertations/5109. LSU Doctoral Dissertations, Paper 5109.

[108] M. L. Avila, K. E. Rehm, S. Almaraz-Calderon, A. D. Ayangeakaa, C. Dickerson, C. R. Hoffman, C. L. Jiang, B. P. Kay, J. Lai, O. Nusair, R. C. Pardo, D. Santiago-Gonzalez, R. Talwar, and C. Ugalde. Experimental study of

the astrophysically important ^{23}Na$(\alpha, p)^{26}$Mg and ^{23}Na$(\alpha, n)^{26}$Al reactions. *Phys. Rev. C*, 94:065804, Dec 2016. doi: 10.1103/PhysRevC.94.065804. URL https://link.aps.org/doi/10.1103/PhysRevC.94.065804.

[109] H. Geissel and C. Scheidenberger. Slowing down of relativistic heavy ions and new applications. *Nuclear Instruments and Methods in Physics Research Section B: Beam Interactions with Materials and Atoms*, 136–138:114–124, 1998. doi: 10.1016/S0168-583X(97)00660-5. URL https://www.sciencedirect.com/science/article/pii/S0168583X97006605. Ion Beam Analysis.

[110] CAEN. V1725 - 16 channel 14-bit 250 ms/s digitizer. https://www.caen.it/products/v1725/, n.d. Accessed: 27 March 2025.

[111] CAEN S.p.A. CoMPASS: Digital Pulse Processing Software for Physics Applications, 2025. URL https://www.caen.it/products/compass/. Accessed: March 6, 2025.

[112] CAEN. CoMPASS software, 2023. URL https://www.caen.it/products/compass/. Accessed: September 2023.

[113] Chloé Fougères. Private communication, 2024.

[114] Wilton N. Catford. Two-body relativistic kinematics calculator. https://personalpages.surrey.ac.uk/w.catford/kinematics/, n.d. Accessed: 18 July 2025.

[115] W. J. Thompson. Poisson distributions. *Computing in Science and Engineering*, 3(3):78–82, May 2001. doi: 10.1109/5992.919271. URL https://ui.adsabs.harvard.edu/abs/2001CSE.....3c..78T.

[116] G. J. Feldman and R. D. Cousins. Unified approach to the classical statistical analysis of small signals. *Physical Review D*, 57(7):3873–3889, Apr

1998. doi: 10.1103/PhysRevD.57.3873. URL https://link.aps.org/doi/10.1103/PhysRevD.57.3873.

[117] H. Jayatissa, M. L. Avila, K. E. Rehm, R. Talwar, P. Mohr, K. Auranen, J. Chen, D. A. Gorelov, C. R. Hoffman, C. L. Jiang, B. P. Kay, S. A. Kuvin, and D. Santiago-Gonzalez. First direct measurement of the $^{13}\mathrm{N}(\alpha, p)^{16}\mathrm{O}$ reaction relevant for core-collapse supernovae nucleosynthesis. *Phys. Rev. C*, 105:L042802, Apr 2022. doi: 10.1103/PhysRevC.105.L042802. URL https://link.aps.org/doi/10.1103/PhysRevC.105.L042802.

[118] S. Takács, F. Tárkányi, A. Hermanne, and R. Paviotti de Corcuera. Validation and upgrading of the recommended cross section data of charged particle reactions used for production of PET radioisotopes. *Nuclear Instruments and Methods in Physics Research Section B: Beam Interactions with Materials and Atoms*, 211(2):169–189, 2003. doi: 10.1016/S0168-583X(03)01264-3. URL https://www.sciencedirect.com/science/article/pii/S0168583X03012643.

[119] Georges Michaud and William A. Fowler. Thermonuclear-reaction rates at high temperature. *Phys. Rev. C*, 2:2041–2049, Dec 1970. doi: 10.1103/PhysRevC.2.2041. URL https://link.aps.org/doi/10.1103/PhysRevC.2.2041.